

**High resolution X-ray diffraction study of
microstructure in compressive and tensile strained
III-V semiconductor epitaxial layers**

By
RAVI KUMAR
PHYS03201104005

Raja Ramanna Centre for Advanced Technology, Indore

A thesis submitted to the
Board of Studies in Physical Sciences
In partial fulfillment of requirements
for the Degree of
DOCTOR OF PHILOSOPHY
of
HOMI BHABHA NATIONAL INSTITUTE








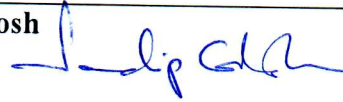


June, 2018

Homi Bhabha National Institute¹

Recommendations of the Viva Voce Committee

As members of the Viva Voce Committee, we certify that we have read the dissertation prepared by Ravi Kumar entitled "High resolution X-ray diffraction study of microstructure in compressive and tensile strained III-V semiconductor epitaxial layers" and recommend that it may be accepted as fulfilling the thesis requirement for the award of Degree of Doctor of Philosophy.

Chairperson – Prof. Rama Chari		Date: 15.3.19.
Guide / Convener – Prof. T. K. Sharma		Date: 15.3.19
Examiner- Prof. D. S. Rana		Date: 15/3/19
Member 1- Prof. S. M. Gupta		Date: 15.3.19
Member 2- Prof. Tapas Ganguli		Date: 15-03-2019
Member 3- Prof. M. H. Modi		Date: 15.3.19
Member 4- Prof. M. K. Chattopadhyay		Date: 15/03/2019
External Member - Prof. Sandip Ghosh		Date: 15/3/19

Final approval and acceptance of this thesis is contingent upon the candidate's submission of the final copies of the thesis to HBNI.

I hereby certify that I have read this thesis prepared under my direction and recommend that it may be accepted as fulfilling the thesis requirement.

Date: Indore

Place: 15/03/2019



T. K. Sharma

¹ This page is to be included only for final submission after successful completion of viva voce.

STATEMENT BY AUTHOR

This dissertation has been submitted in partial fulfillment of requirements for an advanced degree at Homi Bhabha National Institute (HBNI) and is deposited in the Library to be made available to borrowers under rules of the HBNI.

Brief quotations from this dissertation are allowable without special permission, provided that accurate acknowledgement of source is made. Requests for permission for extended quotation from or reproduction of this manuscript in whole or in part may be granted by the Competent Authority of HBNI when in his or her judgment the proposed use of the material is in the interests of scholarship. In all other instances, however, permission must be obtained from the author.


Ravi Kumar

DECLARATION

I, hereby declare that the investigation presented in the thesis has been carried out by me. The work is original and has not been submitted earlier as a whole or in part for a degree / diploma at this or any other Institution / University.



Ravi Kumar

List of Publications arising from the thesis

Published in International Journals

1. Anisotropic distribution of microstructure in compressively strained InP/GaAs epitaxial layers

Ravi Kumar, V K Dixit, C Mukherjee, and T K Sharma

Superlattices and Microstructures, **(2018) 122**, 636.

2. Anisotropic distribution of dislocations density in tensile strained GaP/GaAs epilayers

R. Kumar, V K Dixit, and T K Sharma

Vacuum, **(2018) 154**, 214.

3. Observation of anisotropic distribution of microstructure in GaP/GaAs epitaxial layers

R. Kumar, V K Dixit, T Ganguli, C Mukherjee, A K Srivastava, and T K Sharma

J. Appl. Phys., **(2016) 120**, 135307.

4. Study of the microstructure information of GaAs epilayers grown on silicon substrate using synchrotron radiation

R. Kumar, V K Dixit, A K Sinha, T Ganguli, C Mukherjee, S M Oak, and T K Sharma

J. synchrotron Radiat., **(2016) 23(1)**, 238.

5. Evaluation of Vertical Coherence Length, Twist and Microstrain of GaAs / Si Epilayers Using Modified Williamson-Hall Analysis

Ravi Kumar, Tapas Ganguli, Vijay Chouhan, V K Dixit, Puspen Mondal, A K Srivastava, C Mukherjee, and T K Sharma

J Nano- Electron Phys, **(2014) 6**, 02010.

6. The study of microstructure of III-V polar on non-polar heterostructures by HRXRD

Ravi Kumar, Tapas Ganguli, Vijay Chouhan, and V K Dixit

J Nano- Electron Phys, **(2011) 3**, 17.

Presented in Conferences/ Symposia

1. Anisotropic Distribution of Dislocations Density in Tensile Strained GaP/GaAs Epilayers

Ravi Kumar, V. K. Dixit, Tapas Ganguli, C. Mukherjee, A. K. Srivastava, and T. K. Sharma

International Conference on Thin Films (ICTF-2017), 13-17 November 2017, NPL, New Delhi, India.

2. Asymmetric Dislocation Distribution and Microstructure Analysis for GaP/GaAs

Ravi Kumar, V. K. Dixit, Tapas Ganguli, C. Mukherjee, A. K. Srivastava, and T. K. Sharma

International Conference on New Scintillations on Materials Horizon (ICNSMH-2016), 21-23 October 2016, M.J.P. Rohilkhand University, Bareilly (U.P.), India.

3. The study of microstructure of III-V polar on non-polar heterostructures by HRXRD

Ravi Kumar, Tapas Ganguli, Vijay Chouhan, and V K Dixit

International Symposium on Semiconductor Materials and Devices (ISSMD-
2011), 28-30 January 2011, Vadodara, Gujarat, India.



Ravi Kumar

Acknowledgement

I owe special debt of gratitude to the persons who contributed to the completion of this work.

First and foremost I offer my sincere gratitude to my guide Prof. T. K. Sharma who accepted me as his Ph.D. student and offered me his mentorship, and encouraged me throughout the tenure of my thesis. This Ph.D. work would not have been possible without his constant support, constructive criticism, valuable suggestions/ discussions, unhindered motivation and luminous guidance.

I am also thankful to Prof. Tapas Ganguli for his support and motivation. He introduced me very patiently to amazing world of X-ray diffraction and discussed in detail the research problems that can be understood by X-ray diffraction. I am also thankful to Prof. V. K. Dixit, for patiently listening to my questions and answering them in a lucid way. He gave me the opportunity to openly express my views. I also owe my sincere thanks to Dr. A. K. Sinha for his support in carrying out high resolution X-ray diffraction (HRXRD) experiments on angle dispersive X-ray diffraction beamline at Indus-2 synchrotron radiation facility. It is my great pleasure to thank Dr. Arvind Kumar Srivastava for his support in acquiring transmission electron microscopy (TEM) images of the samples. My thanks are also attributable to Dr. C. Mukherjee for their support in capturing atomic force microscopy (AFM) images of the samples.

I also extend my thanks to Dr. M. P. Joshi, Dr. Rajmohan, Dr. A. Sagdeo, Dr. S. K. Khamari, Dr. Suparna Pal, Dr. Dipankar Jana, Shri U.K. Ghosh, Shri G. Jayaprakash, Shri A. K. Jaiswal, Shri V. K. Agnihotri, Shri Sanjay Porwal, Shri Alexander Khakha, Shri Abhishek Chatterjee, Kum. Geetanjali, Kum. Payal Taya, Shri Mahendra Babu,


Shri Puspen Mondal, Shri Anuj Upadhyay, Shri M. N. Singh, Shri Rijul Roychowdhury, Shri Subhomoy Haldar and Shri Priyabrata Mudi for helping me in my research work.

As the head of divisions Dr. S.M. Oak, Dr. K. S. Bindra and Dr. Rama Chari have made available their support in a number of ways throughout my thesis work.

I am grateful to the members of my Ph.D. advisory committee, for their critical comments and valuable suggestions which were very helpful in summarizing and advancing my research work.

Finally, I would like to express my love and gratitude to my parents, all the family members and my wife for being supportive in my endeavor and extending encouragement throughout the work. I would also like to express my thanks to my beloved daughter Manu for always cheering me up. Abhiman, Lay, Supriya; thanks for inspiring me and always cheering me up.

It was one of the dreams of my parents Shri Virendra Kumar and Smt. Kasturi Devi to see me completing my Ph.D.; it is to them, this work is dedicated.


Ravi Kumar

CONTENTS

SYNOPSIS	i
LIST OF FIGURES	xi
LIST OF TABLES	xvi
Chapter 1 Introduction	1
1.1 Motivation	1
1.2 Introduction of compressive and tensile strained III-V semiconductor epitaxial layers	3
1.3 Literature survey related to the development of novel semiconductor devices based on lattice-mismatched epitaxial layers	5
1.4 Classification of lattice mismatched layers according to choice of substrate	6
1.5 Various issues related to the structural characterization of chosen material combinations	7
1.5.1 High values of dislocation density	7
1.5.2 Type of dislocations governed by the choice of strain	8
1.5.3 Anti-phase domains	8
1.5.4 Anisotropic relaxation of epitaxial layers	9
1.6 Historical perspective: A Need for high crystalline quality of epitaxial layer and their association with HRXRD	10
1.7 Thesis overview	11

Chapter 2	Experimental Methods	13
2.1	Introduction	13
2.2	History of X-ray diffraction	13
2.2.1	Reciprocal space.....	14
2.2.2	Diffraction condition	15
2.2.3	Ewald sphere construction	16
2.2.4	Factors governing the intensity of diffracted beams	17
2.2.5	Intensities of reflections in zinc-blende structure.....	18
2.3	Details of Lab source based HRXRD system	19
2.3.1	X-ray Tube	19
2.3.2	Incident beam optics.....	20
2.3.3	Diffracted beam optics	21
2.3.4	Sample stage.....	22
2.3.5	Detector	22
2.4	Details of synchrotron radiation based HRXRD system.....	23
2.4.1	Incident and diffracted beam optics	24
2.4.2	Detector	25
2.5	Commonly used X-ray geometries and scans	26
2.5.1	Symmetric, asymmetric and skew-symmetric geometries	26
2.5.2	Different types of scans	28
2.6	Atomic force microscopy	28

2.7 High resolution transmission electron microscopy	30
2.8 Photoluminescence spectroscopy	31
2.9 Surface Profilometer	32
2.10 Epitaxial growth by metal organic vapour phase epitaxy	33
2.11 Williamson-Hall analysis method	34
Chapter 3 Study of the Anisotropic Distribution of Microstructure in GaP/GaAs Epitaxial Layers.....	37
3.1 Introduction	37
3.2 Experimental details	41
3.3 Results and discussion.....	43
3.3.1 Observation of anisotropic distribution of microstructure in GaP/GaAs epitaxial layers.....	43
3.3.2 Anisotropic distribution of dislocations density in tensile strained GaP/GaAs epilayers	58
3.4 Conclusion.....	63
Chapter 4 Study of the Anisotropic Distribution of Microstructure in Compressively Strained InP/GaAs Epitaxial Layers	66
4.1 Introduction	66
4.2 Experimental details	67
4.3 Results and discussion.....	69
4.4 Conclusion.....	76

Chapter 5	Study of the Anisotropic Distribution of Microstructure in Compressively Strained GaAs/Si Epitaxial Layers: A Case of Polar on Nonpolar Material Combination	77
5.1	Introduction	77
5.2	Experimental details	80
5.3	Results and discussion	82
5.3.1	HRXRD results based on the synchrotron radiation source	82
5.3.2	Modified Williamson-Hall analysis for studying the microstructure in compressively strained GaAs/Si epitaxial layers	88
5.3.3	Anisotropic distribution of microstructure in compressively strained GaAs/Si epitaxial layers	93
5.4	Conclusion	96
Chapter 6	Summary, Conclusion, and the Future Scope	98
6.1	Summary	98
6.2	Conclusion	101
6.3	Suggestions for future work	101
References		103

SYNOPSIS

Nowadays mismatched epitaxy is routinely utilized to develop numerous semiconductor devices. It is now possible to integrate a multilayer device structure on a foreign substrate irrespective of a large lattice mismatch between them. For such applications, a robust understanding of the epitaxial growth process is essential. Here, various in-situ/ex-situ characterization techniques play a pivotal role where accurate information regarding the structural, optical and electronic properties of epitaxial layers is unambiguously obtained. Out of these, high resolution x-ray diffraction (HRXRD) technique is of paramount importance since it provides a quick and accurate estimate of the crystalline quality of epitaxial layers. However, with the invention of newer combination of layer/substrate materials, it often becomes challenging to acquire and analyze the HRXRD data.¹⁻⁵ In case of mismatch epitaxy, it is indeed a herculean task where the presence of a larger number of defects and dislocations often limits the usefulness of HRXRD technique. A precise knowledge of the nature and density of defects/dislocations is thus essential. This can significantly help in the optimization of crystalline quality of epitaxial layers with a minimal density of defects/dislocations, which leads to an improved performance of the devices based on mismatched epitaxial layers.^{6,7} During the course of this thesis, compressive and tensile strained III-V semiconductor epitaxial layers grown under different conditions are studied. Although such epitaxial layers are promising for several optoelectronic device applications but are prone to possess a high density of defects/dislocations.^{2,5,8}

HRXRD and high resolution transmission electron microscopy (HRTEM) are the two main characterization techniques which have been used to understand the nature

and density of dislocations in lattice-mismatched epitaxial layers. In general, HRTEM provides the most unambiguous evidences about the presence of dislocations in epitaxial layers. However, HRTEM is destructive and in particular the enormous efforts that one needs to put in sample preparation makes the technique largely unattractive for the cases where numerous samples are to be studied over a short period. In all such cases HRXRD is preferred due to its non-destructive nature where the crystalline quality of lattice-mismatched epitaxial layers is accessed by measuring the full width at half maximum (FWHM) of Bragg diffraction peaks. HRXRD is routinely used by epitaxial growers for accessing the crystalline quality of layers, which helps them in preparing the next growth recipe rather quickly. However, no attention is generally paid to the identification of the types of dislocations that might be present in epitaxial layer. All types of dislocations are understood to broaden the diffraction peaks and a low value of FWHM is considered to be a prime indicator of the crystalline quality. However, this might lead to an ambiguity in some cases since the dislocations distribution in lattice-mismatched III–V epitaxial layers is expected to be asymmetrical. New methodologies for the HRXRD characterization of lattice-mismatched III-V semiconductor epitaxial layers are thus desired.

This thesis deals with the development of novel HRXRD characterization methodologies with an overall aim of understanding the anisotropic distribution of microstructure in compressive and tensile strained III-V semiconductor epitaxial layers. In particular, GaAs/Si, GaP/GaAs and InP/GaAs epitaxial layers are investigated in depth. Here, a choice of the material combinations is rather interesting since 1) all the three combinations are nearly 4% lattice-mismatched systems, and 2) issues related to the growth of III-V semiconductors on polar/nonpolar substrates along with the type of

strain i.e. compressive/tensile can be looked into. An anisotropic distribution of microstructure is observed where the origin of anisotropy is found to depend on the nature of strain and the choice of polar/nonpolar substrate. The results obtained from HRXRD measurements are also supported by other complementary techniques i.e. atomic force microscopy (AFM), surface profilometry, HRTEM, and polarization dependent photo-luminescence (PL) measurements. The thesis is organized as follows:

In **Chapter 1**, a brief introduction of compressive and tensile strained III-V semiconductor epitaxial layers is given. Literature survey related to the development of novel semiconductor devices based on the lattice-mismatched epitaxial layers is also given. Lattice-mismatched zinc-blende epitaxial layers can be grown on either polar or non-polar substrates. Those grown on non-polar substrates e.g. GaAs/Si are prone to the formation of anti-phase domains which complicates the analysis of HRXRD data. The lattice-mismatched layers are further classified into two main categories depending on the type of residual strain. For example, GaAs/Si and InP/GaAs epitaxial layers possess compressively strain while GaP/GaAs falls under the tensile category. Various issues related to the structural characterization of chosen material combinations are also described in this chapter. HRXRD, being a fast and non-destructive technique, is given special attention where key issues related to data acquisition and analysis are briefly discussed. Historical perspectives related to the need of high crystalline quality of the epilayers and their association with HRXRD characterization are also discussed. Further, issues related to lattice mismatch and residual strain in epitaxial layers along with various crystalline defects i.e. point defects, line defects, planar defects and volume defects are discussed. At the end of chapter, an outline of thesis is also presented.

Chapter 2 is devoted to various experimental techniques and apparatuses which are used during the course of thesis. To begin with, various concepts involved in HRXRD characterization i.e. reciprocal space, diffraction condition, Ewald sphere construction, factors affecting the intensity of diffracted beams in zinc-blende materials are described in this chapter. Next, the key components of HRXRD system i.e. X-ray sources, incident beam optics, diffracted beam optics, sample stage and detector arm are presented. Subsequently, the components of synchrotron radiation based HRXRD system are also briefly described. Afterwards, conventional HRXRD data acquisition geometries covering symmetric, asymmetric and skew-symmetric configurations along with different types of scans e.g. ω , $\omega/2\theta$, ϕ , and reciprocal space maps are explained in brief. Experimental details of a few other characterization techniques e.g. AFM, surface profilometry, HRTEM, and PL are also discussed. These are used to complement the information obtained from HRXRD characterization of lattice-mismatched epitaxial layers. The chapter ends by a brief description of metal organic vapour phase epitaxy (MOVPE) technique which is used to grow the lattice-mismatched epitaxial samples investigated during the course of thesis.

In **chapter 3**, HRXRD studies related to GaP epitaxial layers grown on GaAs substrate are presented. HRXRD measurements reveals that the GaP layers are tensile strained. Information related to the microstructure of such lattice-mismatched layers is usually obtained by performing a standard procedure known as Williamson-Hall analysis. Here, one uses a set of symmetric reflections i.e. (200), (400) and (600) where HRXRD measurements are generally performed using Cu $K\alpha_1$ x-ray beam.² A sinusoidal variation of FWHMs of symmetric (400) omega scan with sample rotation is observed which indicates about an anisotropic distribution of dislocations in layer.² The

observed anisotropy leads to the different values of lattice relaxation along [011] and [01 $\bar{1}$] directions as revealed by the reciprocal space maps recorded at 0° and 90° azimuths for (42 2) and (422) reflections. The anisotropic relaxation process causes large differences in the values of FWHM of (400) diffraction peaks of omega scans along the [011] and [01 $\bar{1}$] directions. It therefore provides large differences in the values of microstructural parameters of GaP epitaxial layer along the two in-plane orthogonal directions. A systematic Williamson-Hall analysis of HRXRD data confirms the presence of large anisotropy of lattice relaxation process along the two directions. Owing to the lattice mismatch, GaP/GaAs epilayers presented here possess grain boundaries where the broadening of HRXRD pattern is strongly affected by the anisotropy of microstructure and dislocations. The kinetics of dislocations is also discussed in this chapter where it is found that the misfit strain is primarily relieved by 90° partial dislocations up to a certain thickness of epilayer and thereafter the nucleation of 60° perfect dislocations dominates the strain relaxation process. The effect of anisotropic distribution of relaxation process is also seen in the surface topography of GaP epilayer as revealed by AFM images. A large value of lateral coherence lengths (LCL) along [01 $\bar{1}$] direction in HRXRD measurements indicates that the grains are elongated in that direction in comparison to [011] which is confirmed by the AFM images.² The reason of such an asymmetric behaviour is found to be related to the formation of 90° partial and 60° perfect dislocations at different stages of epilayer growth. Such dislocations are commonly observed in zinc-blende tensile strained layers and are classified as α (β) dislocations e.g. dislocations having line of dislocation along [01 $\bar{1}$] ([011]) in tensile system are responsible for poor (good) structural quality along [011] ([01 $\bar{1}$]) direction.² The tilt and twist ratio for α dislocations is found to be very

high (≈ 2.9) in comparison to the ratio for β dislocations (≈ 1.3). It is found that β dislocations are 60° perfect dislocations which is generally observed in zinc blende systems. Furthermore, α dislocations which are responsible for leading to a high value of tilt are identified as 90° partial dislocations. Note that the Burgers vectors of two 90° partial dislocations combine to give a Burgers vector of an edge dislocation pointing toward $[100]$ direction. After a careful literature survey, it is found that there is no standard formula available for estimating the anisotropic dislocation densities for the cases when different type of dislocations are acting along the two orthogonal in-plane directions. The particular issue is addressed in this chapter and a formula based on random distribution of dislocations is proposed to find the dislocation densities of 90° partial and 60° perfect dislocations. The density of 90° partial dislocations is found to be nearly an order of magnitude larger in comparison to 60° perfect dislocations. This is in agreement with the reports available in literature where 90° partial dislocations are found to be responsible for the initial relaxation of layer and are expected to be large in number.² Further, the origin of the anisotropic distribution of dislocations is successfully explained by considering the Burgers vector network, and its consequences are also observed in the cross sectional transmission electron microscopy images.

In **chapter 4**, HRXRD studies on InP/GaAs epitaxial layers are presented. However, contrary to GaP/GaAs epitaxial layers, this is a compressively strained system.⁸ In this case also, a sinusoidal variation of FWHM of omega scan for (400) reflection with sample rotation reveals about the presence of an in-plane anisotropy. Standard Williamson-Hall analysis is used to find the microstructure along the two in-plane orthogonal directions. The tilt and twist ratio for both α and β dislocations is found to be nearly 1.4 indicating that the dislocations are predominantly 60° perfect ones. The

estimated density of 60° perfect dislocations of α type is found to be slightly large in comparison to 60° perfect dislocations of β type. This is in agreement with the reports available in literature where α type 60° perfect dislocations are known to initiate the relaxation process in epilayer. Further, the information obtained from HRXRD measurements about an anisotropic distribution of microstructure in InP/GaAs epitaxial layers is confirmed by performing polarization dependent PL measurements where intensity of PL signal is found to be different along the two in-plane orthogonal directions.

In **chapter 5**, attention is paid to another lattice-mismatched layer substrate combination based on the MOVPE growth of GaAs epitaxial layers on Si substrates. A major difference here is that the layer is expected to be compressive strained. Further, the layer is grown on a nonpolar substrate leading to the formation of anti-phase domains. Here too, a sinusoidal variation of FWHMs of symmetric (400) omega scan with sample rotation is observed which indicates about an anisotropic distribution of dislocations in layer.² Information related to the microstructure is obtained by a systematic Williamson-Hall analysis where a set of symmetric reflections i.e. (200), (400) and (600) is considered.² Out of these, (200) and (600) diffraction patterns, which are expected to be weaker, are further broadened by the anti-phase domains. Moreover, it is found that an unambiguous measurement of (600) diffraction pattern is nearly impossible due to a low value of form factor for (600) reflection when compared with (200) reflection.^{1,4,5} Therefore, a standard Williamson-Hall analysis cannot be performed using Cu $K\alpha_1$ x-ray beam of a laboratory based x-ray source. Under such circumstances, angle dispersive x-ray diffraction beamline (BL-12) of Indus-2⁹ synchrotron radiation source is found to be extremely useful. Here, one can choose a high energy of incident x-ray beam which helps in accessing even further higher order

reflections. Standard Williamson-Hall analysis therefore can be made more accurate and meaningful for GaAs/Si epitaxial layers.³ High intensity of Indus-2 synchrotron radiation source is another advantage since it helps in overcoming the limitation posed by the weak scattering efficiency of epilayer in case of (200) and (600) reflections as mentioned earlier. With the availability of synchrotron radiation source, diffraction patterns corresponding to a set of four symmetric reflections i.e. (200), (400), (600), and (800) are successfully recorded. It enables us in performing standard Williamson-Hall analysis on GaAs/Si epitaxial layers which facilitates the evaluation of microstructure information.³

Although the application of synchrotron radiation source in performing Williamson-Hall analysis on GaAs/Si epitaxial layers is successfully proven but it is not recommended for the routine characterization purpose. Hence, alternate methodologies are required with an aim of accessing a similar information by recording a set of diffraction patterns with a laboratory based x-ray source alone. Under such circumstances, the scheme of modified Williamson-Hall analysis can be implemented by choosing a set of parallel planes which are tilted at a fixed angle with respect to the sample surface.¹⁰ Here, (111), (333) and (444) skew-symmetric reflections are chosen to record the HRXRD data which is then used to measure the information related to the microstructure in GaAs/Si epitaxial layers without any ambiguity. Modified Williamson-Hall analysis is found to provide an accurate measurement of the values of lateral coherence length (LCL), vertical coherence length (VCL), tilt and twist of GaAs/Si epitaxial layers. Furthermore, a simple method based on the orientation of Burgers vector is proposed for estimating the ratio of tilt and twist. In this method, the twist can be found easily once tilt is known. It is rather quick and the measured values

of twist are very similar to those which are otherwise estimated by acquiring numerous HRXRD scans along with tedious fitting procedures. The identification of dislocations along both the in-plane orthogonal directions and the estimation of corresponding dislocation density is addressed by considering the role of Burgers vector and/or their components in tilting and twisting the grains in epilayer.^{2,4} It is found that the dislocations along both the in-plane directions are 60° perfect ones which is found to be in good agreement with the reports available in literature. Density of dislocations along the two in-plane orthogonal directions is found to be different confirming an asymmetrical distribution. Presence of 60° mixed dislocations is confirmed from the cross sectional HRTEM images of GaAs/Si samples. Furthermore, the estimated value of VCL is found to be equivalent to the layer thickness measured by the surface profiler.

Finally in **chapter 6**, main results of the thesis are summarized along with a brief discussions on the scope of future work. In this thesis, HRXRD characterization of compressive and tensile strained III-V semiconductor epitaxial layers is carried out with an aim of understanding the anisotropic distribution of microstructure. It is found that standard Williamson-Hall analysis can be used to understand the asymmetric distribution of microstructure in zinc blende epitaxial layers grown on polar substrate irrespective of the type of residual strain. However, the method fails in case of epitaxial layers grown on nonpolar substrates. In that case, either the HRXRD measurements should be performed on a synchrotron radiation source or modified Williamson-Hall analysis, based on a set of skew-symmetric reflections, needs to be carried out in case the measurements are performed with a lab source. HRXRD characterization results from three nearly 4% lattice-mismatched material combinations are presented in this thesis where an anisotropic distribution of microstructure is observed along the two in-

plane orthogonal directions. In case of compressively strained systems, it is found that the same type of dislocations i.e. 60° perfect dislocations are responsible for lattice relaxation, where the anisotropy occurs mainly due to the difference in the density of dislocations. On the other hand, in case of tensile strained epilayers, 90° partial dislocations are primarily responsible for initial relaxation of the layer while 60° perfect dislocations dominate the relaxation process beyond a certain layer thickness. The present work is useful in understanding the relaxation process in compressive and tensile strained III-V semiconductor epitaxial layers which is expected to help in the development of novel semiconductor devices based on such materials. To conclude, HRXRD is proven to be a fast and contactless method to understand the relaxation process in lattice-mismatched III-V semiconductor epitaxial layers which depends on the type of strain in layer and the choice of polar/nonpolar substrate. Further, a quick identification of dislocation type and estimation of the dislocation density is possible by HRXRD technique. As part of future work, it is proposed to study a few other lattice-mismatched system e.g. GaP/Ge, AlAs/Si etc. which shall help in developing a robust understanding about the lattice relaxation process in such material combinations.

LIST OF FIGURES

Figure 1.1 (a) Standalone layer having lattice constant smaller than the substrate, (b) Layer in case of pseudomorphic growth, (c) Relaxed layer, (d) Standalone layer having lattice constant larger than substrate, (e) Layer in case of pseudomorphic growth and (f) Relaxed layer. ¹¹	4
Figure 1.2 Bandgap of III-V and III-N semiconductors versus lattice constants.	5
Figure 1.3 An anti-phase domain boundary. ⁵⁰	9
Figure 2.1 Incident and diffracted X-rays have a path difference (POQ) of $2d \sin \theta$. Both the rays will be in phase if $2d \sin \theta = n\lambda$. ^{73, 79}	15
Figure 2.2 Ewald Sphere construction. ⁷⁹	16
Figure 2.3 (a) Schematic of four circle (ω , 2θ , ϕ and ψ) goniometer, ^{82, 83} (b) Photograph of PANalytical X'pert pro MRD system. ^{82, 83}	19
Figure 2.4 Schematic diagram of U-channel cut Bartels monochromator. ^{82, 83}	21
Figure 2.5 Schematic diagram of a triple bounce analyzer crystal. ^{82, 83}	21
Figure 2.6 Schematic diagram of Xenon filled proportional counter. ^{82, 83}	23
Figure 2.7 Schematic layout of BL-12 beamline at Indus-2. ⁹	24
Figure 2.8 Schematic diagram of HRXRD setup at BL-12 beamline. ⁹⁰	25
Figure 2.9 Schematic diagram of a NaI (Tl) scintillator detector. ⁹¹	26
Figure 2.10 HRXRD geometries ((a) symmetric, (b) asymmetric and (c) skew-symmetric) that are used during the course of this thesis.	27
Figure 2.11 Schematic diagram to describe the basic concept behind an atomic force microscope. ¹⁰⁰	29
Figure 2.12 Preparation of TEM sample for cross-sectional view. ¹⁰⁶	31

Figure 2.13 Schematic diagram for polarization dependent PL spectroscopy, ND and F stand for the neutral density filter and long pass filter respectively.....	32
Figure 2.14 Schematic diagram of an MOVPE growth system. ¹¹¹	33
Figure 2.15 A graphical description of various microstructural parameters. ¹²¹	35
Figure 3.1 HRXRD configuration for studying the anisotropy in epilayer where the sample is rotated around the growth direction by an angle ϕ . For skew-symmetric HRXRD scans, the sample is rotated by an angle ψ around the direction of the projection of incident X-ray beam.....	42
Figure 3.2 HRXRD pattern of GaP/GaAs epitaxial layer for (400) reflection recorded at 0°, 90°, 180°, and 270° azimuths.	43
Figure 3.3 Reciprocal space maps of GaP/GaAs epitaxial layer for (a) (42 2) reflection at 0° azimuth, and (b) (422) reflection at 90° azimuth.....	45
Figure 3.4 FWHMs of ω scans for (400) HRXRD pattern plotted as a function of azimuth where the solid line is a guide to eye.....	46
Figure 3.5 (a) Linear fit of $(\Delta q_x)^n$ plot with $(\alpha_{hkl})^n$ at 0° and 90° azimuths for the Williamson-Hall analysis, and (b) variation of α_{hkl} for several skew-symmetric reflections where the inset shows the distribution of tilt and twist along different crystallographic directions.	48
Figure 3.6 AFM image of GaP/GaAs epitaxial layer that shows anisotropic distribution of grains along [01 1] and [011] directions.....	49
Figure 3.7 (a) 90° partial dislocations reacting to give an edge dislocation, line of dislocation is shown along [01 1] direction, and (b) the components of 60° perfect dislocations where the line of dislocation is shown along [011] direction.	52

Figure 3.8 HRTEM image of GaP/GaAs epitaxial layers showing the formation of stacking fault ribbons and a highly defected interface for cross section orientation. ..	53
Figure 4.1 HRXRD pattern of InP epitaxial layer grown on GaAs substrates for (400) reflection recorded at two azimuths.	69
Figure 4.2 FWHM of (400) rocking curve plotted as a function of azimuth where solid line is a guide to the reader's eye.....	70
Figure 4.3 Reciprocal space maps of InP/GaAs layer recorded at 0° and 90° azimuths for {422} reflection.	71
Figure 4.4 Williamson-Hall analysis: a) The width (Δq_x) obtained from pseudo-Voigt fitting of the omega scan diffraction peaks, n is related to Lorentzian fraction in the pseudo-Voigt fitting, is plotted as a function of q^n , b) The value of α_{hkl} are plotted as a function of ψ for 0 and 90° azimuths.	72
Figure 4.5 Atomic force microscopy image of InP epitaxial layer grown on GaAs substrates.	74
Figure 4.6 10 K Polarization dependent PL spectra of InP epitaxial layer grown on GaAs substrates.	75
Figure 5.1 Schematic of the portion of the limiting sphere to illustrate the allowed symmetric reflections for GaAs grown on (100) Si substrates. Here, the [011] direction lies in the growth plane. The limiting sphere governed by the wavelength of the laboratory X-ray source (Cu $K\alpha_1$) is shown by a dashed line (red) whereas the limiting sphere governed by the wavelength of synchrotron radiation is shown by a solid line (black). Note that the (800) reflection (red filled circle) is accessible only when HRXRD measurements are performed at the synchrotron radiation source. At 15.5 keV energy a	

few more reflections are accessible. However, the reflections only up to (800) are shown here for simplicity.	83
Figure 5.2 HRXRD pattern of GaAs epilayer grown on Si substrate (Sample S1): (a) ω scans, (b) $\omega/2\theta$ scans, where the curves labelled as 2A (2B), 4A (4B) and 6A (6B) are the diffraction patterns for the (200), (400), (600) reflections acquired using the laboratory (synchrotron) based X-ray source. Note that the (800) scans are acquired only at the synchrotron radiation source. The overlaying solid lines show the pseudo-Voigt fitting of the experimental data.	84
Figure 5.3 Williamson–Hall plots prepared using ω and $\omega/2\theta$ scans for (200), (400), (600) and (800) symmetric reflections recorded using the Indus-2 synchrotron radiation source. The size of the error bars is smaller than the size of symbols. The value of n is 1 for the Lorentzian component and 2 for the Gaussian component; $1 < n < 2$ whenever the line shape is defined by a pseudo-Voigt profile.	86
Figure 5.4 (a) AFM image ($5\ \mu\text{m} \times 5\ \mu\text{m}$) of the GaAs epilayer grown on Si substrate, and (b) frequency distribution of the grain size obtained from the image analysis of AFM data.....	87
Figure 5.5 (a(b)) WH plots for GaAs/Si samples (S2, S3, and S4) using the ω ($\omega/2\theta$) scans for a set of skew-symmetric reflections. Straight lines show a linear fitting of the experimental data. (c) Variation of α_{hkl} for several skew-symmetric reflections.....	89
Figure 5.6 (a) The components of Burgers vector for 60° mixed dislocation, (b) cross section HRTEM image of sample S4, and (c) magnified HRTEM image around the centre of previous image.	91
Figure 5.7 FWHMs of ω scans for (400) HRXRD pattern plotted as a function of azimuth.	93

Figure 5.8 (a) Intensity versus q_x curves for (111), (333) and (444) reflection of GaAs/Si sample. The fitting of the curve is shown by overlaying line. (b) Modified Williamson–Hall plots prepared using ω scans for (111), (333), and (444) skew-symmetric reflections recorded using Cu $K\alpha_1$. The size of the error bars is smaller than the size of symbols.	95
Figure 5.9 Variation of α_{hkl} for several skew-symmetric reflections.....	96

LIST OF TABLES

Table 1.1 Some examples of III-V layers classified according to type of strain and choice of polar/non-polar substrate.	7
Table 2.1 Intensities of diffracted X-ray beam corresponding to various reflections of zinc-blende system.	18
Table 2.2 Details of cradle translational movements and rotation capabilities.	22
Table 2.3 Type of scans and their descriptions.	28
Table 3.1 Summary of the microstructural parameters of GaP/GaAs epitaxial layer obtained from the Williamson-Hall analysis of HRXRD data.....	57
Table 4.1 The values of microstructure namely lateral coherence length, tilt, twist and their ratio obtained from Williamson-Hall analysis at two orthogonal azimuths along with the values of dislocation density in InP epitaxial layer grown on GaAs substrate.	72
Table 5.1 Summary of various growth parameters of the GaAs / Si samples.	82
Table 5.2 Summary of the microstructure of GaAs epilayers grown on Si substrate. The values of lateral coherence length (LCL), vertical coherence length (VCL), tilt and micro-strain are obtained by performing the Williamson–Hall analysis of HRXRD data acquired at the Indus-2 synchrotron radiation source. The values of grain size and layer thickness measured by atomic force microscopy and surface profiler techniques are also included for comparison purposes.....	88
Table 5.3 Summary of the microstructure obtained from the modified Williamson-Hall analysis for the three GaAs/Si samples S2, S3 and S4.....	92

Table 5.4 Summary of microstructural parameters of GaAs/Si epitaxial layer obtained from the modified Williamson-Hall analysis of HRXRD data.	95
---	----

Chapter 1

Introduction

1.1 Motivation

Most of III-V compound semiconductors find numerous applications in the development of optoelectronic devices. Let it be a light emitting diode, laser diode, high efficiency multi junction solar cell, or high electron mobility transistor, all such devices are made out of III-V compound semiconductors.^{1,6} On the other hand, Silicon is the most sought semiconductor material owing to its enormous applications in the development of electronic devices. In view of this, a monolithic integration of group III-V semiconductors on Silicon substrate is of paramount importance.¹ Availability of a large band offset in multilayer heterostructure is quite attractive for the device designers.^{1,7} With the help of modern epitaxy tools, it is now possible to grow lattice-mismatched systems offering a wider selection of band gaps and band offsets, which plays a key role in improving the performance of existing devices and also in the development of newer devices.^{1,3,6,7} However, epitaxial growth of these semiconductors on foreign substrates is extremely challenging. Due to a large difference in the values of lattice constant and thermal expansion coefficient for a given layer and substrate combination, a poor crystalline quality of the layer is often reported.¹⁻³ The grown layer is usually filled with defects and dislocations, and often their density is enormous which makes them largely unsuitable for any device development. Under such cases, epitaxial growers try to optimize the growth conditions with an overall aim of minimizing the density of defects/dislocations in the layer. A quick feedback on the crystalline quality of layer is thus desirable which must arrive from a reliable characterization technique.

In past, several methods have been used by epitaxial growers for investigating the crystalline quality of epitaxial layers, where high resolution X-ray diffraction (HRXRD) is found to be especially attractive. Unlike high resolution transmission electron microscopy (HRETM), no time consuming sample preparation is needed in case of HRXRD. Although, HRETM provides a direct information about the natures of defects/dislocations in layer but the information obtained is rather of microscopic nature. Moreover, HRTEM cannot be used for the routine characterization purpose. On the other hand, HRXRD being a non-destructive, macroscopic, rapid and accurate technique emerges as an ideal tool for knowing the nature and density of defects/dislocations for routine applications.² In HRXRD, crystalline quality of epitaxial layers is studied by measuring the full width at half maximum (FWHM) of a diffraction peak. Defects/dislocations are assumed to broaden the diffraction peaks and a low value of FWHM is generally targeted by the growers. However, this might be inappropriate if the distribution of defects/dislocations is anisotropic in layer. Depending upon the sample mounting on HRXRD cradle, one can get different values of FWHM of rocking curves for the same sample. This is inappropriate and needs to be suitably corrected. One therefore needs to find new methodologies for the HRXRD characterization of lattice-mismatched III-V semiconductor epitaxial layers where asymmetric distribution of defects/dislocations is anticipated.

During the course of this thesis, novel HRXRD characterization methodologies are developed with an overall aim of understanding the anisotropic distribution of microstructure in compressive and tensile strained III-V semiconductor epitaxial layers. In particular, GaP/GaAs, InP/GaAs, and GaAs/Si epitaxial layers are taken for the case study. One can grow zinc-blende epitaxial layers on either polar or non-polar substrates.

For example, GaAs/Si epitaxial layers, which is a case of polar on non-polar growth, are prone to the formation of anti-phase domains. Further depending upon the layer/substrate combination, the residual strain in layer can be of either compressive or tensile nature. For example, GaAs/Si and InP/GaAs epitaxial layers possess compressively strain while GaP/GaAs falls under the tensile category. In particular, historical perspectives related to the HRXRD characterization technique of lattice-mismatched epitaxial layers and other fundamental aspects related to distribution of defects/dislocations in zinc-blende epitaxial layers are discussed in this chapter.

1.2 Introduction of compressive and tensile strained III-V semiconductor epitaxial layers

As mentioned earlier that an epitaxial layer grown on a substrate of a different lattice constant is expected to be strained only up to a certain thickness.¹¹ Beyond this limit, which is known as the critical layer thickness (h_C), layer relaxes via generation of defects and dislocations. Lattice mismatch and strain are defined in terms of lattice constants of the substrate (a_{0S}) and fully relaxed layer (a_{0L}), which is shown in **Figure 1.1(a and d)**, by the following Equations:¹¹

$$strain(\varepsilon) = \frac{a_{0S} - a_{0L}}{a_{0L}} \quad (1.1)$$

$$mismatch(m) = \frac{a_{0S} - a_{0L}}{a_{0S}} \quad (1.2)$$

The layer remains pseudomorphic (fully strained) until the thickness of layer is smaller than the critical layer thickness. In this case, in-plane lattice constant of the layer

(a_{0L}) matches with that of the substrate (a_{0S}) as shown in **Figure 1.1(b and e)**.¹¹

Whenever the thickness of layer exceeds the critical layer thickness, the layer will reach its fully relaxed lattice constant via formation of misfit dislocations.¹¹ In this case the layer is partially or totally relaxed depending on the thickness of layer, see **Figure 1.1(c and f)**.¹¹

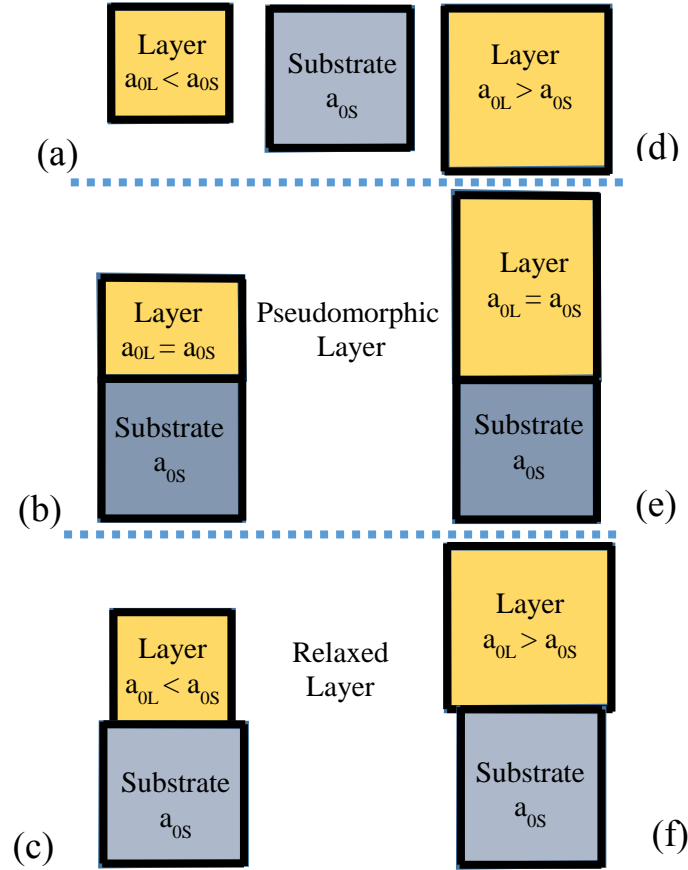


Figure 1.1 (a) Standalone layer having lattice constant smaller than the substrate, (b) Layer in case of pseudomorphic growth, (c) Relaxed layer, (d) Standalone layer having lattice constant larger than substrate, (e) Layer in case of pseudomorphic growth and (f) Relaxed layer.¹¹

The in-plane lattice constant and band gap of commonly used III-V semiconductors including nitrides lie between 3.11–5.87 Å and 6.20–0.65 eV (200–1900 nm).^{12–14} **Figure 1.2** shows the lattice constant and band gaps of commonly used III-V semiconductors. Due to their wide band gap range, III-V semiconductors cover a

broad spectral range starting from ultraviolet to infrared region. Following the successful demonstration of devices using wurtzite GaN/Sapphire and AlN/Sapphire systems,¹⁵ current trend is to harness possible zinc-blende combinations with large lattice mismatch. Novel optoelectronic devices are anticipated from such material combinations. For example, GaP/GaAs, InP/GaAs, and GaAs/Si are some of the promising mismatch systems which have nearly 4% lattice mismatch and can be grown using standard epitaxial systems.

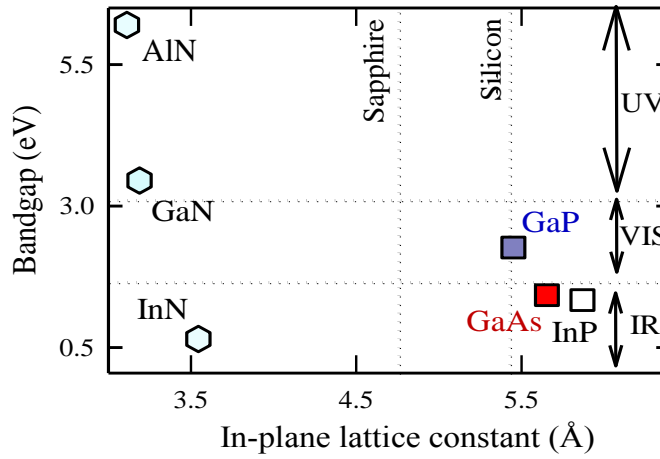


Figure 1.2 Bandgap of III-V and III-N semiconductors versus lattice constants.

1.3 Literature survey related to the development of novel semiconductor devices based on lattice-mismatched epitaxial layers

Harnessing of lattice mismatch zinc-blende layers is an active area of research for more than 40 years.¹⁶ Theoretical work regarding the mismatched systems was started by Frank and van der Merwe way back in 1949.^{16–20} It was later extended by several other researchers where various concepts including the concept of critical layer thickness and concept of reducing the growth area were coined.^{21–30} Esaki and Tsu³¹

proposed the concept of semiconductor superlattice in 1970, which have been extensively utilized by numerous researchers in many applications thereafter.^{31,32} High-frequency field-effect transistor was demonstrated using strained GaAs/In_xGa_{1-x}As/GaAs superlattice by T E Zipperian et al. in 1983.¹⁶ This structure had the advantage over high-frequency field-effect transistor based on nearly lattice matched GaAs/AlGaAs/GaAs system that in this system no DX centres are present which might limit the device performance.^{33,34} The modulation-doped field-effect transistors based on AlGaAs/InGaAs/GaAs utilize larger band offset of AlGaAs in comparison to GaAs.³⁵⁻³⁷ Heterojunction bipolar transistors (HBT) using the GaAs/In_xGa_{1-x}As/GaAs system are demonstrated with high dc gains.³⁸ In order to achieve potential of mature Si technology, edge emitting GaAs/AlGaAs lasers on Si are also reported.³⁹ For the realization of high efficiency solar cells, III-V solar cells on Si substrates have also been fabricated.^{40,41} GaP/GaAs material combinations are recently reported for the fabrication of various devices, for example, in flash memory devices,⁴² and next generation non-linear optical devices.^{43,44}

1.4 Classification of lattice mismatched layers according to choice of substrate

The layers which are compressively or tensile strained can be further classified according to choice of substrate. For example GaAs/Si is a compressively strained system which is grown on a non-polar substrate. Similarly GaP/Ge is a tensile strained system which is grown on non-polar substrate. On the other hand, InP/GaAs and GaP/GaAs layers are compressively and tensile strained layers respectively which are grown on polar substrate. The zinc-blende layers on non-polar substrates allow the

formation of anti-phase domains which are detrimental for the devices made out of them.

Table 1.1 lists some of the nearly 4% lattice mismatched layers

Table 1.1 Some examples of III-V layers classified according to type of strain and choice of polar/non-polar substrate.

Layer	Compressively strained		Tensile strained	
	On polar substrate	On non-polar substrate	On polar substrate	On non-polar substrate
Example	InP/GaAs	GaAs/Si	GaP/GaAs	GaP/Ge

1.5 Various issues related to the structural characterization of chosen material combinations

We have chosen GaP/GaAs, InP/GaAs and GaAs/Si systems to understand the layer relaxation mechanism in compressively and tensile strained layers along with the choice of polar and non-polar substrate. The following issues arise when we plan to perform a structural characterization of these samples:

1.5.1 High values of dislocation density

These layers have nearly 4% lattice mismatch where the critical thickness is typically below 50 Å and therefore a high value of dislocation density is expected.^{2,45} The thermal expansion coefficient difference which is large in GaAs/Si layers in comparison to the other two systems makes the situation worst.^{5,45} It makes HRXRD data acquisition on a lab source quite tough since the intensity of certain reflections is

weaken by a high value of dislocation density and also by the presence of antiphase domains.

1.5.2 Type of dislocations governed by the choice of strain

For the case of compressively (tensile) strained layer the extra half plane of interface dislocations lie in the substrate (layer) which is needed to relieve the strain.⁴⁶ Due to this reason, primarily 60° perfect dislocations (90° partial dislocations) act in compressively (tensile) strained layers contrary to a common belief that it is only the 60° perfect dislocations which dominate the relaxation process in zinc-blende epitaxial layers.⁴⁷ The same is discussed in this thesis by a careful selection of material combinations, and the understanding developed here is based on a careful analysis of HRXRD data.

1.5.3 Anti-phase domains

In epitaxial growth of GaAs layer on Si (100) substrates, a non-centrosymmetric polar material ($\bar{4}3m$) is grown on centrosymmetric non-polar ($m\bar{3}m$) material.⁴⁸ This leads to the presence of two in-plane sub-lattices which are 90° rotated with respect to each other. The difference occurs due to the finite possibility of two separate locations that are available for the incorporations of cation (Ga/In) and anion (As/P) adatoms.⁴⁸ The anti-phase domains weakens the diffraction intensity of selective reflections in the diffraction pattern of such layers.^{1,4,5,49} Due to a high dislocation density, selective broadening of the diffraction peak for some of the reflections occurs, which makes the structural characterization extremely difficult. **Figure 1.3** shows a schematic diagram depicting the formation of anti-phase domains.⁵⁰

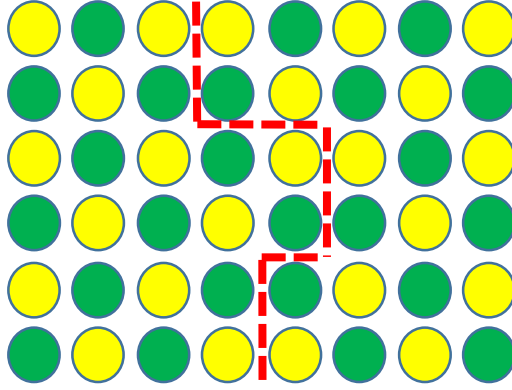


Figure 1.3 An anti-phase domain boundary.⁵⁰

1.5.4 Anisotropic relaxation of epitaxial layers

It is seen that the relaxation of zinc-blende epilayers is not isotropic due to their non-centrosymmetric nature.^{2,48} It is well known that the dislocations glide with different velocities along the two orthogonal $\langle 011 \rangle$ directions in $\{111\}$ glide plane for zinc-blende epilayers grown on (100) oriented substrates. In case of tensile strained III–V epilayers, misfit dislocations with the line of dislocations along $[01\bar{1}]/[011]$ crystallographic directions are known as α/β dislocations, respectively.^{46,51–60} It is also understood that the glide velocity of α dislocations can be even two orders of magnitude larger than that of the β dislocations.^{52–54,56–58} Because of the difference in their core structures and glide velocities, α and β dislocations possess different formation energies, which leads to an asymmetry in the formation of dislocations along the two orthogonal in-plane directions.^{55,61} These are known to be primarily 60° dislocations which glide in the $\{111\}$ crystallographic plane, but 30° and 90° partial dislocations also glide in the same plane as summarized by Goldman et al.⁵⁹ For a particular layer-substrate combination, specific sets of dislocations nucleate which propagate along different crystallographic directions with their respective glide velocities.^{46,52–54,62,63} It is therefore obvious that the strain relaxation is expected to be anisotropic in III–V

epilayers grown on (100) oriented zinc-blende substrates. Moreover, the direction of strain relaxation can be swapped as a function of substrate miscut, dopant, and strain type.^{54,56,64} In general, anisotropic relaxation of epitaxial layer is of considerable interest both from the experimental and theoretical point of view.^{46,54,57,59,65} Therefore, understanding the atomistic mechanism of nucleation of dislocations is very important for the growth of novel heterostructures. Some of the interesting examples where the process of anisotropic strain relaxation is already studied are InGaAs/ GaAs,^{52,55,56,66,67} SiGe/Ge,⁴⁷ GaSb/GaAs,⁶⁸ InSb/GaAs,^{68,69} InAsP/InP,⁷⁰ InGaAs/InP,⁶⁵ etc.

Understanding the mechanism of strain relaxation is very important for the optimization of epilayer quality grown by the mismatch epitaxy. Nucleation, propagation, and reaction of dislocations govern the ultimate dislocation density that can be achieved for an epilayer grown on a foreign substrate.^{62,71} One can target the minimum density of dislocations by implementing such concepts that might otherwise limit the overall performance of a device made out of the mismatched epilayers. Owing to these reasons, the study of dislocation formation and their propagation along different directions is considered to be of great interest.

1.6 Historical perspective: A Need for high crystalline quality of epitaxial layer and their association with HRXRD

Prior to the development of Norelco (Philips) X-ray diffractometer in 1945,⁷² Laue diffraction pattern remained as a standard X-ray characterization tool for the characterization of crystalline materials for several years. Till 1950s X-ray diffractometers were available in many research laboratories across the world.⁷² In 1980s, high resolution X-ray diffraction (HRXRD) characterization of single crystals

became a routine exercise in several semiconductor labs.⁷³ X-ray diffraction analysis was commonly used for finding the structural quality of epilayers. This led to the development of various new devices which are currently in use. Realization of all these devices which are based on III-V layers grown on either III-V semiconductor or Si substrates could not have been possible without the involvement of HRXRD characterization.

1.7 Thesis overview

This thesis deals with the development of novel HRXRD characterization methodologies with an overall aim of understanding the anisotropic distribution of microstructure in compressive and tensile strained III-V semiconductor epitaxial layers. In particular, GaP/GaAs, InP/GaAs, and GaAs/Si epitaxial layers are investigated in depth. The thesis is organized as follows:

In **Chapter 1**, motivation of thesis along with a brief introduction of compressive and tensile strained III-V semiconductor epitaxial layers is given. **Chapter 2** is devoted to various experimental techniques and apparatuses which are used during the course of thesis. Modern HRXRD techniques (both laboratory and synchrotron radiation) and other technique such as atomic force microscopy (AFM), transmission electron microscopy (TEM), surface profilometer and photo-luminescence (PL) technique are described in brief. In **chapter 3**, HRXRD studies related to tensile strained GaP epitaxial layers grown on GaAs substrate are presented. A method for estimating the density of dislocations for HRXRD measurements is also proposed in this chapter. In **chapter 4**, HRXRD studies on compressively strained InP/GaAs epitaxial layers are presented. In **Chapter 5**, HRXRD characterization of compressively strained GaAs/Si

epilayers is addressed. Williamson-Hall analysis is successfully applied using both synchrotron radiation source and Cu $K\alpha_1$ lab source. Modified Williamson-Hall analysis is also proposed which is needed in the HRXRD characterization of GaAs/Si epilayers using a lab source. The procedure for finding the twist value from tilt value is also discussed using Burgers vector consideration. Finally in **chapter 6**, main results of the thesis are summarized along with a brief discussions on the scope of future work.

Chapter 2

Experimental Methods

2.1 Introduction

This chapter describes various experimental techniques and apparatuses that are used to characterize epitaxial layers in this thesis. In the beginning of chapter, basic concepts involved in HRXRD characterization i.e. reciprocal space, diffraction condition, Ewald sphere construction, factors affecting the intensity of diffracted beams etc. are briefly discussed. Thereafter, details of the experimental setups for laboratory and synchrotron radiation based HRXRD systems are described in this chapter. The chapter also covers other characterization techniques like surface profilometry, atomic force microscopy (AFM), transmission electron microscopy (TEM), and photoluminescence (PL) spectroscopy which are used to complement the information received from HRXRD. At the end of chapter, Williamson-Hall analysis is discussed which is extensively used for finding the microstructure of epitaxial layers during the course of this thesis.

2.2 History of X-ray diffraction

Wilhelm Conrad Röntgen, a professor at University of Würzburg in Germany discovered X-rays in 1895. While investigating range of cathode rays in air coming out from evacuated glass tubes, he noticed some glow on a screen coated with fluorescent barium platinocyanide kept far away from the range of cathode rays. He argued that it is happening from some unknown rays coming out from the walls of the tube, and named them as 'X-rays'.⁷⁴ Max Theodor Felix von Laue thought that if X-rays have

wavelength similar to the interatomic distances in crystals, then they will be diffracted by crystals.⁷⁵ In 1912, he along with Walter Friedrich and Paul Knipping did first diffraction experiment on CuSO₄ crystal.⁷⁶ The crystal structure of Diamond determined by W. H. Bragg and W. L. Bragg and those of other crystals viz. sodium chloride, potassium chloride and potassium bromide determined by W. L. Bragg were published during that period.⁷⁶ It led to the opening of a new field in the name of X-ray diffraction (XRD) which was to become a routine method for characterizing single crystals. Basics of XRD are briefly described in this chapter.

2.2.1 Reciprocal space

Diffraction pattern of a crystal is a true representation of the reciprocal space associated with the crystal structure.⁷⁷ The primitive vectors of reciprocal lattice (b_1 , b_2 and b_3) are connected by the primitive vectors of direct lattice⁷⁸ (a_1 , a_2 and a_3) via the following relations:

$$\begin{aligned}
 b_1 &= 2\pi \frac{a_2 \times a_3}{a_1 \cdot (a_2 \times a_3)} \\
 b_2 &= 2\pi \frac{a_3 \times a_1}{a_1 \cdot (a_2 \times a_3)} \\
 b_3 &= 2\pi \frac{a_1 \times a_2}{a_1 \cdot (a_2 \times a_3)} \\
 b_i \cdot a_j &= 2\pi \delta_{ij}
 \end{aligned} \tag{2.1}$$

Further, the real space vector (R) and reciprocal space vectors (G) are defined by the following relations:

$$R = c_1 a_1 + c_2 a_2 + c_3 a_3 \tag{2.2}$$

$$G = hb_1 + kb_2 + lb_3 \quad (2.3)$$

where c_1, c_2, c_3, h, k and l are integers. A set of all R vectors and G vectors defines the direct lattice and reciprocal lattice respectively.⁷⁸ G vector is perpendicular to corresponding plane (hkl) and has a length $|G|=1/d_{hkl}$, where d_{hkl} is the distance between consecutive (hkl) planes.⁷⁸

2.2.2 Diffraction condition

Figure 2.1 shows interaction of in-phase incident X-rays on a crystal at an angle θ having (hkl) planes of spacing d , which are then diffracted at an angle θ . If the path difference POQ (i.e. $2d \sin \theta$) is equal to an integral multiple (n) of wavelength (λ), then the diffracted and incident X-rays are in-phase:^{14,78,79}

$$2d \sin(\theta) = n\lambda \quad (2.4)$$

Equation (2.4) is known as Bragg's Law.

Bragg's condition expressed in **Equation (2.4)** can also be defined in the following manner using incident (k) and diffracted wave vector (k'):^{78,80}

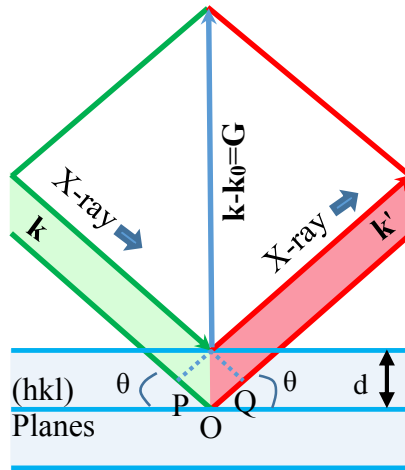


Figure 2.1 Incident and diffracted X-rays have a path difference (POQ) of $2d \sin \theta$. Both the rays will be in phase if $2d \sin \theta = n\lambda$.^{73, 79}

$$k' - k = G \quad (2.5)$$

$$\Delta k = G \quad (2.6)$$

2.2.3 Ewald sphere construction

Bragg's law can also be written as

$$\sin(\theta_{hkl}) = \frac{\frac{1}{d_{hkl}}}{\frac{1}{\lambda}} = \frac{d_{hkl}^*}{1/\lambda} \quad (2.7)$$

P. P. Ewald drew the circle as shown in **Figure 2.2** to demonstrate the diffraction condition in reciprocal space.^{78,80} The circle is named as Ewald circle after him. In this diagram, the incident and diffracted X-rays are at an angle 2θ . The reciprocal lattice vector (d^*) starts from reciprocal lattice point O and ends at B. In order to satisfy diffraction condition, reciprocal lattice vector, Ewald circle and diffracted X-ray should

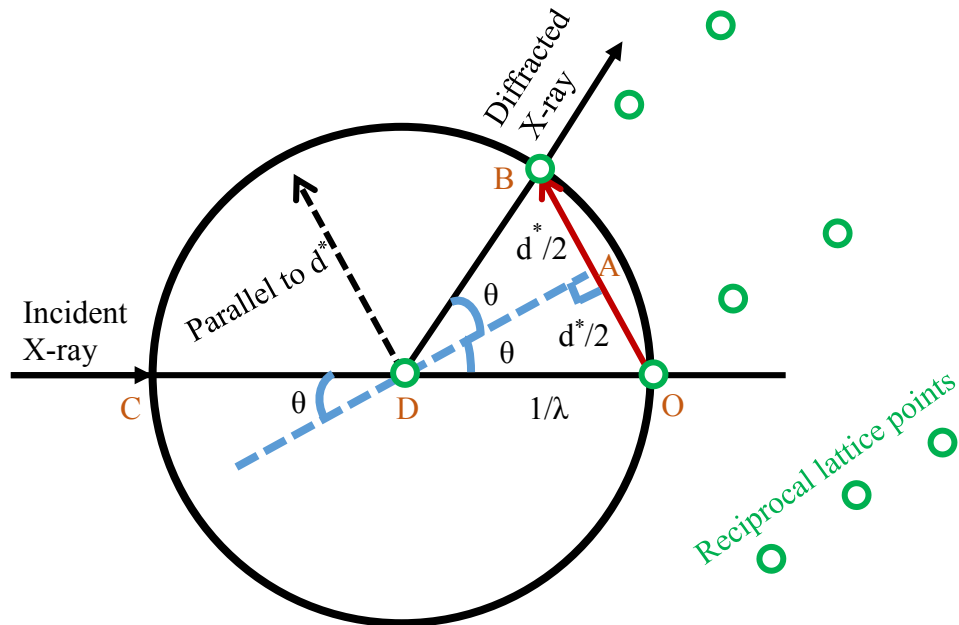


Figure 2.2 Ewald Sphere construction.⁷⁹

meet at reciprocal lattice point (B). The Bragg's law is shown via triangles DOA and DAB.

2.2.4 Factors governing the intensity of diffracted beams

In this section, scattering of X-rays by a single electron, then by an atom (ensembles of scattering electrons), and finally by a unit cell (group of atoms) is described. The scattering intensity for incident un-polarized X-ray light of intensity I_0 is given by the following Equation:^{14,81}

$$I_P = \frac{I_0}{2} \left(\frac{\mu_0}{4\pi} \right)^2 \left(\frac{q^4}{m^2 r^2} \right) [1 + \sin^2 2\theta] \quad (2.8)$$

Where I_P is the scattered intensity to the point of observation P at a distance r, $\mu_0 = 4\pi \times 10^{-7} \text{ Hm}^{-1}$, q is the electronic charge, and m is the rest mass of electrons. 2θ is the angle between the incident and scattered X-ray beams. The quantity named as form factor (f) describes the net scattering power for X-rays by all the electrons of an atom.⁸¹ It is defined as the ratio of the amplitude of the wave scattered by an atom to the amplitude that would be scattered by an electron.⁸¹ It depends on the atomic number, scattering angle, and X-ray wavelength.⁸¹ Structure factor (F_{hkl}) defines the net scattering power of X-rays by a unit cell of a crystal which is governed by the vector sum of X-ray amplitudes of the individual atoms of unit cell.⁸¹ It is the ratio of the amplitude of wave scattered by all atoms in a unit cell to amplitude of wave scattered by an electron.⁸¹

The structure factor for hkl reflection for the unit cell containing N atoms with atomic structure factors f_n , is given by following Equation:^{14,81}

$$F_{hkl} = \sum_{n=1}^N f_n e^{2\pi i(hu_n + kv_n + lw_n)} \quad (2.9)$$

Where (u_n, v_n, w_n) is the positional coordinates of n^{th} atom.

The intensity of diffracted X-ray beam corresponding to a reflection is proportional to $|F_{hkl}|^2$ i.e. multiplication of the structure factor by its complex conjugate.^{14,81}

2.2.5 Intensities of reflections in zinc-blende structure

The unit cell of zinc-blende crystal system is made of atoms A and B (form factors f_A and f_B respectively) and contains 4 atoms of A and B type each. The positions of A atoms are $(0,0,0)$, $(0, \frac{1}{2}, \frac{1}{2})$, $(\frac{1}{2}, 0, \frac{1}{2})$ and $(\frac{1}{2}, \frac{1}{2}, 0)$ and that of the B atoms are $(\frac{1}{4}, \frac{1}{4}, \frac{1}{4})$, $(\frac{1}{4}, \frac{3}{4}, \frac{3}{4})$, $(\frac{3}{4}, \frac{1}{4}, \frac{3}{4})$ and $(\frac{3}{4}, \frac{3}{4}, \frac{1}{4})$. After putting these values in the structure factor Equation (2.9), we find a simplified expression:⁸¹

$$|F_{hkl}|^2 = \left[f_A + f_B e^{\frac{-i\pi}{2}(h+k+l)} \right] \left[1 + e^{-i\pi(k+l)} + e^{-i\pi(h+l)} + e^{-i\pi(h+k)} \right] \quad (2.10)$$

therefore, the intensity of diffracted X-ray beam corresponding to a reflection depends on h, k, l . **Table 2.1** lists the probable conditions of X-ray diffraction for a zinc-blende crystal.^{14,81}

Table 2.1 Intensities of diffracted X-ray beam corresponding to various reflections of zinc-blende system.

S. No.	$ F ^2$	Condition	Reflection	Example
1	0	h, k and l are mixed even and odd	forbidden	(231)
2	$16(f_A - f_B)^2$	$(h+k+l)$ is an odd multiple of two	weak	(006)
3	$16(f_A^2 + f_B^2)$	$(h+k+l)$ is odd	Strong	(111)
4	$16(f_A + f_B)^2$	$(h+k+l)$ is an even multiple of two	Very strong	(004)

2.3 Details of Lab source based HRXRD system

High resolution X-ray diffractometer is typically equipped with three parts: incident beam optics, diffracted beam optics and cradle as schematically described in **Figure 2.3(a)**.^{82–84} Most of the HRXRD measurements reported in this thesis are performed on PANalytical X'Pert Pro Diffractometer shown in **Figure 2.3(b)**. Details of the HRXRD systems used in the thesis are described in this section.

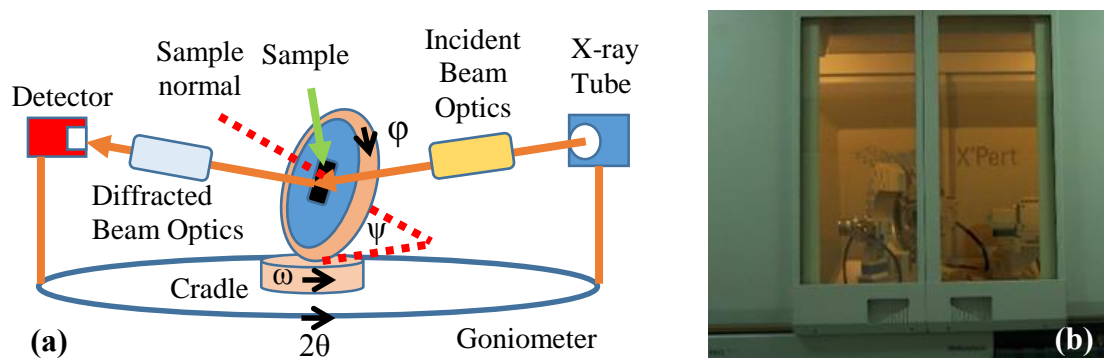


Figure 2.3 (a) Schematic of four circle (ω , 2θ , ϕ and ψ) goniometer,^{82, 83} (b) Photograph of PANalytical X'pert pro MRD system.^{82, 83}

2.3.1 X-ray Tube

In X-ray tube, electron beam from a heated cathode (commonly tungsten filament cathode is heated by passing ≈ 40 mA electric current) is accelerated by high voltage (typically 45kV) towards the anode target e.g. Copper. Electron beam hits the target along a thin line i.e. rectangle about 0.4 by 12 mm in vacuum sealed atmosphere thus causing the emission of X-rays.^{81,82} The emitted X-ray leave the tube through either line or point focus beryllium window. The two windows are located at 90° with respect to each other. Incident electrons give up some of their energy in the interaction with either the orbital electrons or nucleus of the atoms present in target and generate X-rays. The emitted X-rays have a continuous energy distribution known as Bremsstrahlung or

white radiation. Here, the X-rays production process is extremely inefficient and $\approx 99\%$ incident energy is dissipated as heat in the collision process. Therefore, it becomes necessary to water cool the metal target in order to avoid melting. The high energy electrons ejected from the inner shells of target atoms and the vacancies thus generated are filled by the electrons of higher levels, emitting energy difference as characteristic X-rays. These characteristic X-ray lines are superimposed on the white radiation. Generally, $K\alpha_1$ characteristic line of Copper (Cu) target, which carries an energy of 8048 eV, is used in HRXRD measurements due to the following reasons: 1) high heat conductivity of Copper helps in an efficient heat removal from the target and 2) Cu $K\alpha_1$ emission wavelength is suitable for studying zinc-blende crystals due to moderate 2θ angles for most of the commonly used reflections. The line focus mode gives more intense X-ray beam in comparison to the point focus at the cost of resolution which is more relevant in case of single crystals. Most of the samples studied in this thesis have mosaic nature, therefore, these samples are studied in line focus geometry.

2.3.2 Incident beam optics

To fulfill the requirement of HRXRD measurements, where one needs to keep the energy resolution ($\Delta E/E$) better than 10^{-3} in order to separate the closely spaced peaks, usage of X-ray monochromator is essential. The commonly used monochromator is Bartels monochromator as shown in **Figure 2.4**. Four bounces of X-ray reflection are made inside channel cut U-shaped Ge (220) single crystal as shown in **Figure 2.4**. X-ray beam coming out of the monochromator is free from unwanted white radiation and other characteristic peaks except Cu $K\alpha_1$. This monochromator is used with X-rays escaping from the point focus window where resolution is high at the cost of intensity.

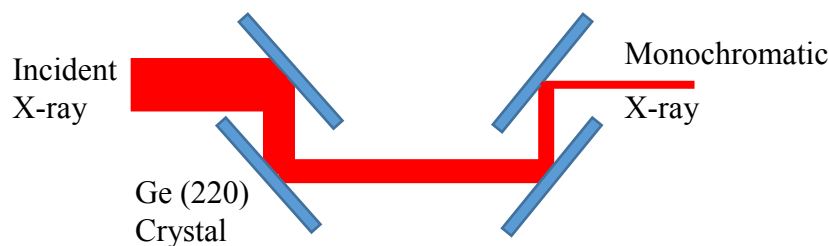


Figure 2.4 Schematic diagram of U-channel cut Bartels monochromator.^{82, 83}

Ge (220) monochromator gives a beam angular divergence of 12 arc sec. In case of hybrid monochromator, X-rays escaping from line focus window are incident on a parabolic mirror in order to make them parallel before injecting them into the above-mentioned monochromator. The parabolic mirror and monochromator assembly is packed in a single unit which is known as hybrid monochromator. The hybrid monochromator gives beam angular divergence of ≈ 18 arc sec. Most of the HRXRD experiments reported in this thesis are performed with hybrid monochromator.

2.3.3 Diffracted beam optics

In diffracted beam optics, a slit typically of 0.1-1 mm width is inserted in the path of diffracted X-ray beam before it falls on the detector.⁸⁵ For high resolution measurements an analyzer crystal, as shown in **Figure 2.5**, is sometime put in place of the slit.⁸⁵ The analyzer crystal is a triple bounce Ge(220) X-ray monochromator with ≈ 12 arc sec angular divergence.⁸⁵

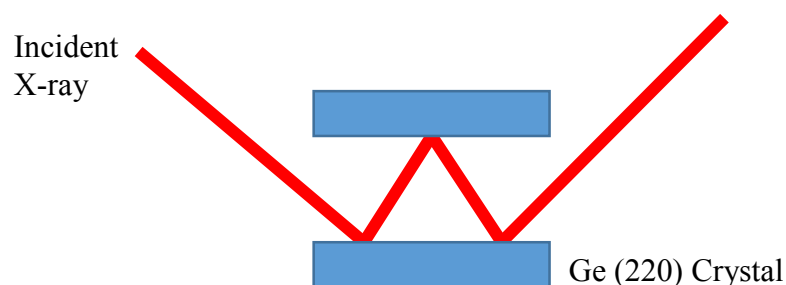


Figure 2.5 Schematic diagram of a triple bounce analyzer crystal.^{82, 83}

2.3.4 Sample stage

The flat and circular sample stage is mounted on the motorized cradle of HRXRD goniometer as shown in **Figure 2.3(a)**. In addition to X, Y and Z translational motions, in-plane rotation (ϕ) and tilt rotations (ψ) are also possible. **Table 2.2** provides a list of cradle movement and rotation capabilities of HRXRD system used during the course of this thesis work.

Table 2.2 Details of cradle translational movements and rotation capabilities.

Cradle Movement	Range	Step Size
X-axis	+50 mm to -50 mm	0.01 mm
Y-axis	+50 mm to -50 mm	0.01 mm
Z-axis	10 mm	0.01 mm
ϕ	360°	0.02°
ψ	$+90^\circ$ to -90°	0.01°
2θ	-6.1° to 162.8°	0.0001°
ω	-8.5° to 180.4°	0.0001°

2.3.5 Detector

The most commonly used detector for Cu $K\alpha_1$ X-rays is Xenon filled proportional counter. It consists of a cylindrical tube filled with Xenon gas where an anode wire is kept at 1-3 kV potential difference with respect to the grounded tube as shown in **Figure 2.6**.⁸² Xenon gas is used because of its high atomic number which makes it easily ionizable upon incidence of Cu $K\alpha_1$ X-rays. Krypton is also a suitable candidate for proportional detectors but its spectral response is nearly 50% less for Cu $K\alpha_1$.⁸⁶ Incident X-rays cause photoelectron ejection from the filled gas.⁸⁷ Since the ionization energy of noble gas is of the order of 30 eV and a single photon of Cu $K\alpha_1$

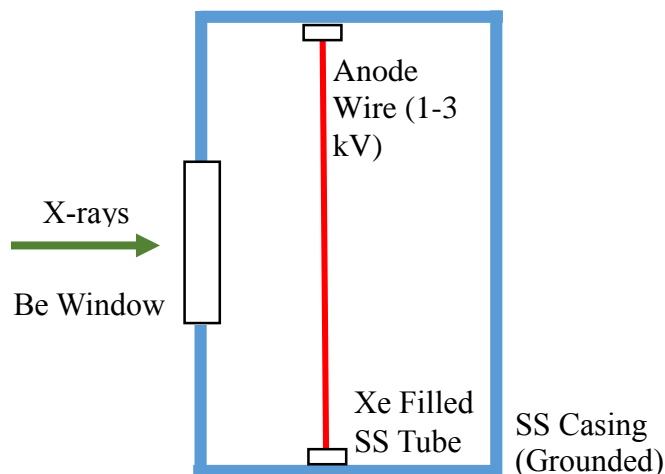


Figure 2.6 Schematic diagram of Xenon filled proportional counter.^{82, 83}

carries 8 keV energy, typically 240 electron-ion pairs are produced.^{87,88} Anode wire is kept at high positive voltage, the acceleration of photo generated electrons and their collision with other noble gas atoms produces an avalanche of electrons.⁸⁷ The collected charge is proportional to the number of incident X-ray photons, which is the basis of operation of a proportional counter.⁸⁷

2.4 Details of synchrotron radiation based HRXRD system

A few experiments are also conducted on a synchrotron radiation (SR) based HRXRD system. In this section, details of the angle dispersive X-ray diffraction beamline (BL-12) of Indus-2^{9,89} synchrotron radiation source are given. Indus-2 has a nominal electron energy of 2.5 GeV and a critical wavelength of about 1.98 Å. The main characteristics of SR source are high intensity, wide energy range and a low divergence of beam. BL-12 angle dispersive X-ray diffraction (ADXRD) beamline with energy tunability and high photon flux is used for HRXRD measurements. Horizontal and vertical root-mean-square (r.m.s.) beam sizes of synchrotron radiation coming at the centre of the bending magnet port (BL-12) are 0.234 and 0.237 mm along with the corresponding beam divergence of 0.35 and 0.06 mrad respectively. The photon energy

at BL-12 beamline is tunable from 5 to 25 keV. Various components of the HRXRD setup at BL-12 beamline are described in this section.

2.4.1 Incident and diffracted beam optics

Photon beam emitted from the bending magnet port (BL-12) passes through the incident beam optics consisting of pre-mirror (M_1), Si(311) double crystal monochromator and a post mirror (M_2) before it falls on the sample under investigation. The pre-mirror (M_1) is a Si mirror (M_1) coated with ≈ 500 Å thick Pt layer to collimate the beam at the experimental station as shown in the **Figure 2.7**. Si (311) crystal based double crystal monochromator focuses the beam in sagittal direction i.e. vertical to the diffraction plane. After that a post mirror (M_2) focuses the monochromatic beam towards the sample holder mounted at six circle diffractometer. The diffractometer is consisted of four circle 5020 Huber diffractometer, one circle goniometer on the 2θ arm to mount the detector and one circle goniometer on the 2θ arm to mount the analyzer crystal in the meridional direction i.e. along the diffraction plane. The incident beam energy resolution ($\Delta E/E$) is about 10^{-4} which is suitable for performing HRXRD measurements.

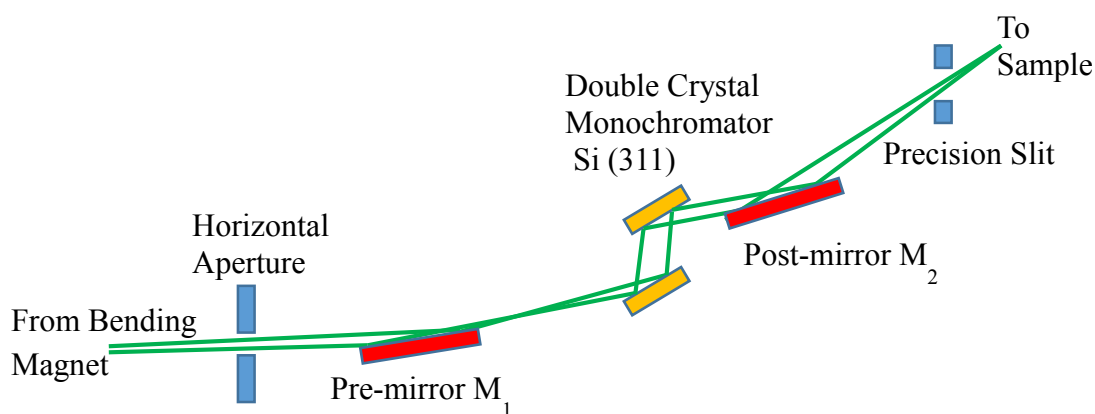


Figure 2.7 Schematic layout of BL-12 beamline at Indus-2.⁹

The general 4-circle goniometer with cradle is shown in **Figure 2.8**.⁹⁰ It shows the details of 4-circle goniometer's rotation capabilities in the experimental setup at BL12 beamline of Indus-2. During the experiments, a slit was inserted before the detector to spatially (along the diffraction plane) limit the diffracted beam before reaching the detector.

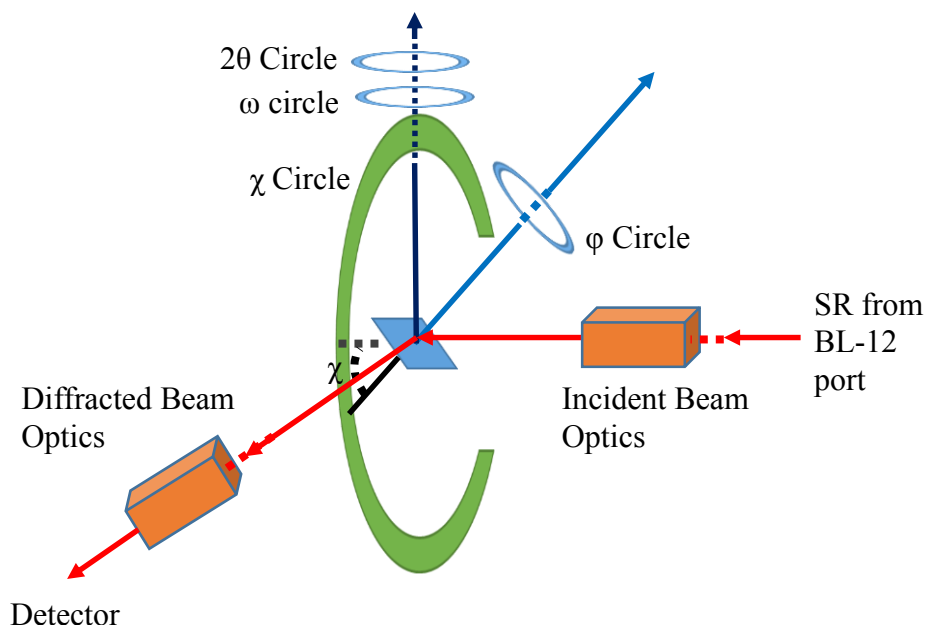


Figure 2.8 Schematic diagram of HRXRD setup at BL-12 beamline.⁹⁰

2.4.2 Detector

A scintillator detector which provides intensity proportional to the intensity of diffracted beam is used for the measurements. It is a Single Channel Scintillation Detector, SCCD-4 manufactured by Radicon Ltd., Russia. It contains 2 mm thick scintillation NaI(Tl) crystal with photomultiplier tube in a closed case having beryllium window of 24 mm diameter entrance. It has the capability to measure X-ray photon flux in the energy range of 5-30 keV (2.5- 0.4 Å) that includes the energy 15.5 keV (0.8 Å) at which the experiments are performed. The schematic of a scintillator detector excluding electronics part is shown in **Figure 2.9**.⁹¹ The detector is consisted of the

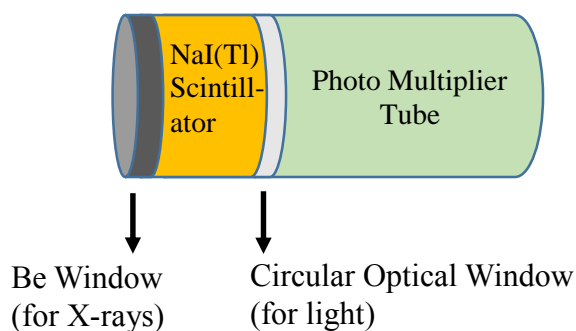


Figure 2.9 Schematic diagram of a NaI (Tl) scintillator detector.⁹¹

following components: Be window is used to transmit the X-ray beam and to protect NaI (Tl) scintillator material. Beryllium is used as a window material because it is a metal having low density and low atomic mass and thus it has low absorption of X-rays.⁹² NaI (Tl) scintillator material is used to absorb incident photon energy and to convert it into visible photon.⁹³ Although the bandgap of NaI crystal is ≈ 5.5 eV (≈ 225 nm)⁹⁴, but small doping with Tl ions create energy levels in its forbidden gap enabling this to emit the light in visible range.^{95,96} An optical window is used to transmit this scintillation to a photo multiplier tube where it incidents on photodiode to emit electrons.⁹⁷ By sequentially placing dynodes, multiplication of electrons by secondary emission is achieved. In this way the current of electrons multiplies several times before the signal electrons are collected by the anode.⁹⁷

2.5 Commonly used X-ray geometries and scans

The most common HRXRD geometries viz. symmetric, asymmetric and skew-symmetric scans for acquiring HRXRD data are described in this section.

2.5.1 Symmetric, asymmetric and skew-symmetric geometries

Schematic diagram of various HRXRD geometries is shown in **Figure 2.10**. In symmetric and skew-symmetric scan geometry, ω angle i.e. the angle between sample

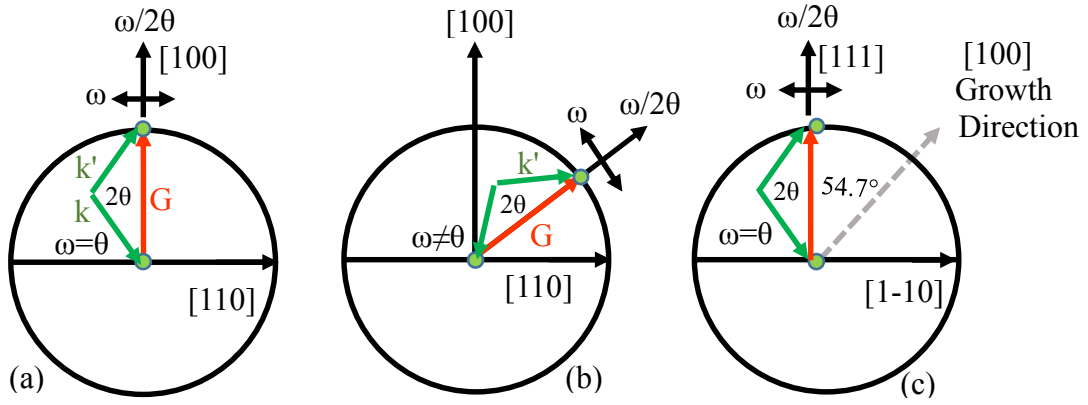


Figure 2.10 HRXRD geometries ((a) symmetric, (b) asymmetric and (c) skew-symmetric) that are used during the course of this thesis.

surface and incident X-ray is equal to θ angle i.e. the angle between reflecting plane and incident X-ray. The difference between the two geometries can be made with the value of ψ angle i.e. the angle between reflecting plane and growth plane. For symmetric scan the value of ψ is zero because reflecting plane is parallel to the growth plane. For skew-symmetric scans the value of ψ is nonzero because reflecting plane is not parallel to growth plane. In asymmetric scan geometry, ω angle is not equal to θ . The difference between the two angles is equal to the angle between the reflecting plane and growth plane. The three geometries are depicted in **Figure 2.10** for (100) growth direction.

The symmetric scan geometry is shown for any symmetric reflecting plane and skew-symmetric scan geometry is shown for (111) reflecting plane. The asymmetric scan geometry is shown for any arbitrary reflecting plane. Note that ω and $\omega/2\theta$ directions in symmetric scan geometries are along in-plane and out-of-plane (perpendicular to growth plane) directions respectively. On the other hand, in asymmetric scan geometries the two directions are along in-plane and out-of-plane with respect to the reflecting plane. In skew-symmetric scan geometry, ω scan direction is parallel to in-plane direction and $\omega/2\theta$ scan direction is along the reflecting plane normal

respectively. Note that the reflecting plane is inclined at a specific angle with respect to the growth plane e.g. 54.7° in case of $\{111\}$, in skew-symmetric geometry.

2.5.2 Different types of scans

The most common diffraction scans that are used in this thesis are summarized in **Table 2.3**. ω scans provide primarily the in-plane sample quality depending on the scan geometry. On the other hand, ω - 2θ scan provides primarily out-of-plane information of the sample whereas ϕ scan is an important tool to find the epitaxial nature of a layer grown on a given substrate.⁹⁸ Acquisition of Reciprocal space map (RSM), i.e. a 2-dimensional scan is a standard tool to find the strain, relaxation, film composition, layer tilt, crystal quality and misorientation of a thin film on a given substrate^{14,82,99}

Table 2.3 Type of scans and their descriptions.

Scan	Description
ω -scan (Rocking curve)	During this scan, ω changes while 2θ is kept constant.
ω - 2θ scan (Radial scan)	Goniometer rotates ω and 2θ at a constant angular ratio of 1:2.
Reciprocal space map (RSM)	Multiple $\omega/2\theta$ scans are recorded at different ω values.
ϕ -scan	ϕ is varied while all other angles are kept constant.

2.6 Atomic force microscopy

During the atomic force microscopy (AFM) image acquisition in non-contact mode, the interaction force between an ultra-sharp tip and sample is recorded while keeping the tip-sample separation within nanometer range. This process is repeated at

different parts of the sample in order to get a topographic image.¹⁰⁰ Schematic diagram describing the basic concept behind an AFM instrument is shown in **Figure 2.11**.¹⁰⁰ The vertical resolution of AFM can be up to 0.1 nm which is more than 1000 times better than the optical diffraction limit.¹⁰¹ AFM works on the principle of Hooke's law ($\mathbf{F} = -\mathbf{k} \cdot \delta$) where deflection of the cantilever (δ) having spring constant (k) changes according to the interaction force between the tip and the sample:¹⁰⁰

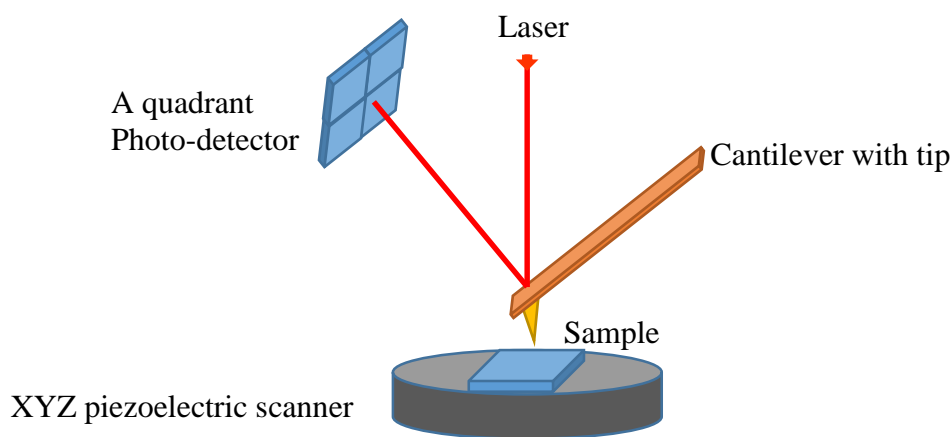


Figure 2.11 Schematic diagram to describe the basic concept behind an atomic force microscope.¹⁰⁰

There are four major components of an AFM system excluding electronics part: laser, cantilever with sharp tip, XYZ piezoelectric scanner and a quadrant photo detector. When there is no deflection, the laser is reflected at the centre of the photo-diode but as soon as the deflection of the cantilever occurs, the laser spot position on the photodiode vary. The laser spot variation provides the deflection force and the position acquired from XYZ piezoelectric scanner gives the position of the tip at sample.¹⁰⁰ In this way, a surface topography image is generated. For semiconductors, AFM measurements are performed in air therefore stiff and high-resonance frequency cantilevers are preferred.¹⁰² High stiffness of the cantilever helps in overcoming the adhesive and capillary forces of the samples in air. High-resonance frequency of the cantilever

provides the fastest possible scan rates. The non-contact tapping mode is preferred to find the topography image in which the cantilever oscillates near its resonance frequency and scans the sample surface without touching the sample surface.¹⁰³ AFM measurements reported in this thesis are performed in non-contact mode using a multimode scanning probe microscope (NT-MDT, SOLVER-PRO) which uses Silicon cantilever tip of radius of curvature 10 nm with resonant frequency 190 kHz and spring constant 5.5 Nm^{-1} .

2.7 High resolution transmission electron microscopy

High Resolution Transmission electron microscopy (HRTEM) uses high-energy electron beam to transmit through a specimen of nanometer thickness to produce high resolution image of columns of atoms.^{104,105} The transmitted beam i.e. forward scattered beam which carries reference phase of the electron wave front and diffracted beams are used to acquire HRTEM images.¹⁰⁵ The interference patterns formed from the phase relationship of diffracted beams gives HRTEM image.¹⁰⁵ Spatial resolution of TEMs lies in sub-nanometer range owing to very short (typically few pico-meters) de Broglie wavelength of high energy electrons.¹⁰⁴ In HRTEM, electron beam is controlled by electrical and magnetic fields according to the laws of electrodynamics. Since the mass of electron is smaller when compared with other charged particles, sample damage is expected to be rather minimal.¹⁰⁴ Nevertheless, one can cause unwanted damage to the sample, if appropriate measurement conditions are not chosen. The specimen thickness requirement to record HRTEM image is a function of primary electron energy and atomic number of the material. In case of III-V semiconductors, it turns out to be typically $\approx 100 \text{ nm}$. During the course of this thesis, the cross-sectional HRTEM micrographs are recorded using Philips CM200 system at an accelerated voltage of 200

kV. The microscope has a W/LaB₆ gun, X-ray detector (EDX) for compositional analysis and CCD camera.

Next, the sample preparation method adopted for HRTEM image acquisition is discussed. **Figure 2.12** shows two pieces of the sample glued together to form a HRTEM sample for cross sectional view. This method of sample preparation is known as “sandwich” technique.¹⁰⁶ In order to reduce the thickness of the specimen to nearly 20 μm mechanical grinding with diamond grit paper is used. Finally, ion milling of the sample using Ar⁺ is employed for fine polishing of the sample.

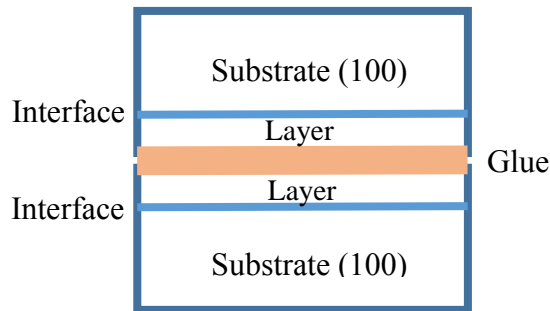


Figure 2.12 Preparation of TEM sample for cross-sectional view.¹⁰⁶

2.8 Photoluminescence spectroscopy

Photo-induced luminescence signal associated with conduction to valence band electronic transitions in a semiconductor material is collected in photoluminescence (PL) spectroscopy.¹⁰⁷ In PL, anisotropic distribution of radiative defects can be probed in addition to the usual bandgap related electronic transitions via polarization dependent PL measurements. **Figure 2.13** shows the setup used for acquiring PL data. Second harmonic Nd:YAG (emission wavelength = 532 nm) is used to excite the photoluminescence. A neutral density (ND) filter is used to keep the intensity of the laser beam fixed irrespective of polarizer setting, while a long pass filter is kept prior to the entrance slit of monochromator in order to suppress the contribution of scattered

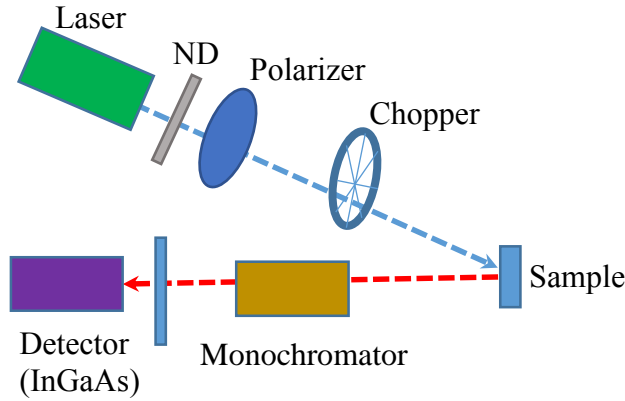


Figure 2.13 Schematic diagram for polarization dependent PL spectroscopy, ND and F stand for the neutral density filter and long pass filter respectively.

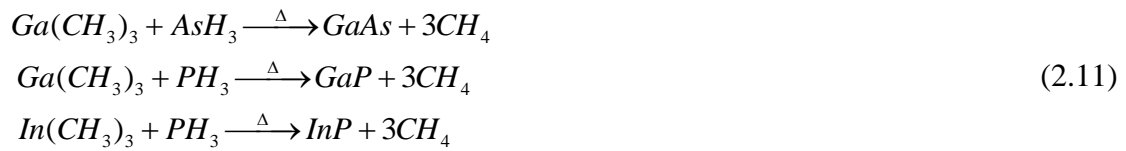
laser radiation. A mechanical chopper is used to enable phase sensitive detection for better signal to noise ratio. PL signal is dispersed with the help of a 1/2m monochromator before being detected by an InGaAs detector.

2.9 Surface Profilometer

A Stylus-Based surface profilometer provides information related to the layer thickness and topography of the semiconductor sample.¹⁰⁸ In case of surface profilometer, a diamond stylus moves along a line over the sample surface and records the change in elevation at each step during its travel with the help of a piezoelectric sensor.¹⁰⁹ For this measurement, a step is made by a selective chemical etching of the layer. The surface profilometer has a vertical resolution of approximately 0.1 nm.¹⁰⁹ Layer thickness of most of the samples reported in this thesis is determined by a Surface Profilometer model Alpha-step IQ (KLA Tencor make) - a mechanical, stylus-based step profilometer.

2.10 Epitaxial growth by metal organic vapour phase epitaxy

In this section, epitaxial growth technique namely metal organic vapour phase epitaxy (MOVPE), which is used to grow the samples, is described. MOVPE is essentially a chemical vapour deposition process based on metalorganic compounds sources where pyrolysis can occur at relatively low temperature. This helps in a low temperature growth of layer thus realizing a sharp interface.^{110,111} The typical process which takes place in epitaxial growth of GaAs, GaP and InP from metalorganic sources and hydride sources at the growth temperature in the range of 500-700 °C is shown below:



Initial developments in MOVPE growth were made by the researchers at Rockwell Corporation, USA in the late 1960s.¹¹² A generalized schematic of the MOVPE system is shown in **Figure 2.14**. Group III metalorganic compounds viz.

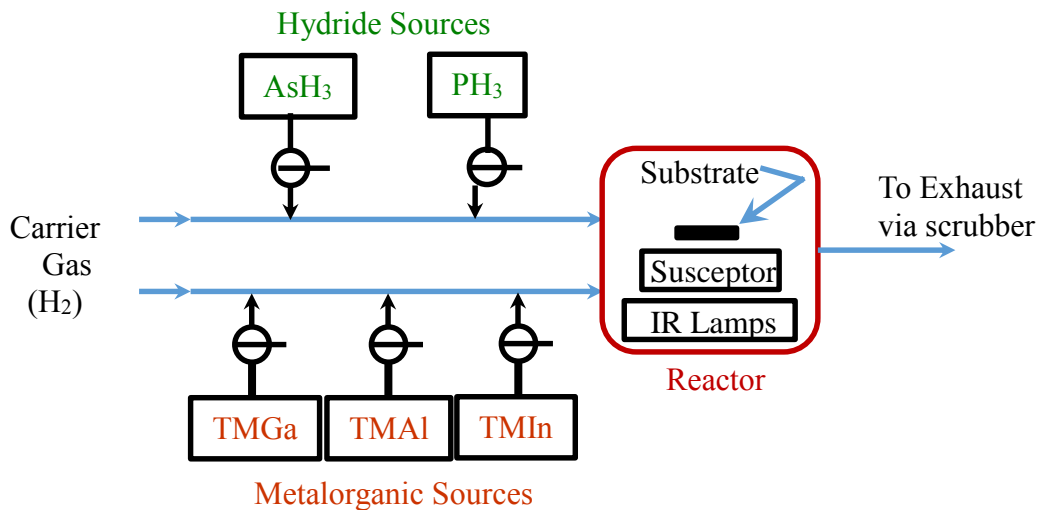


Figure 2.14 Schematic diagram of an MOVPE growth system.¹¹¹

trimethylgallium (TMGa), trimethylaluminium (TMAI) and trimethylindium (TMIn) along with group V hydride sources viz. AsH₃, PH₃ are used as precursors. Substrate e.g. GaAs, Si etc. are put on Graphite susceptor which is heated by infra-red lamps. Various un-used gases and bi-products leave the MOVPE reactor via a scrubber unit for the safety purpose. A major attraction of MOVPE is that the recipe of growth once optimized can be used for large-scale production which shows the versatility of process for commercial applications.¹¹³ MOVPE is unquestionably the most versatile technique to grow III-V alloys.¹¹³ However, problem related to need of expensive reactants and precise control of parameters are the biggest challenge before the epitaxial growers.¹¹³

2.11 Williamson-Hall analysis method

Williamson Hall (WH) analysis¹¹⁴ is a standard choice for in-depth structural characterization viz. microstructural information of both epitaxial layers and polycrystalline systems for a long time. This method is attributed to G. K. Williamson and his student, W. H. Hall.¹¹⁴ Some of the examples of semiconductor material systems that are studied using Williamson Hall (WH) analysis are GaN¹¹⁵, AlGaIn¹¹⁵, ZnO¹¹⁶, InN^{117,118}, GaAs/Si^{1,49}, GaP/Si¹¹⁹ etc. The microstructure information include lateral coherence length (LCL), vertical coherence length (VCL), tilt, twist and micro-strain.^{4,5,12,120,121} Here, LCL/VCL defines the average length of the grain along/perpendicular-to the growth direction over which X-rays are scattered coherently.^{4,5,12,120,121} The tilt/twist angle is the out-of-plane/in-plane misorientation angle of the grains.^{4,5,12,120,121} Various microstructures parameters are graphically demonstrated in **Figure 2.15**.

In standard Williamson Hall (WH) analysis, a set of ω and $\omega/2\theta$ scans are recorded for symmetric parallel planes e.g. (200), (400), (600), (800) etc. planes in the

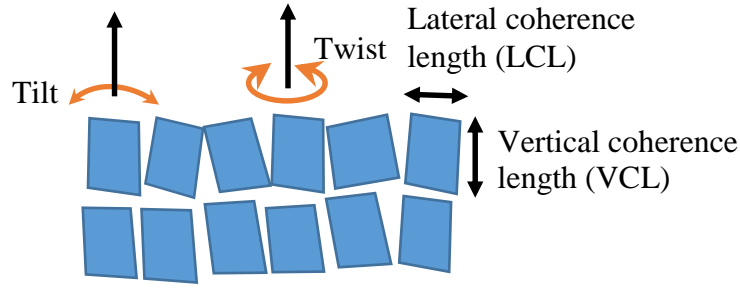


Figure 2.15 A graphical description of various microstructural parameters.¹²¹

case of (100) epitaxy. For the ease of data analysis, the recorded data is converted in reciprocal lattice units (rlu) using the following formulae:

$$\begin{aligned} q_x &= \frac{1}{\lambda} [\cos \omega - \cos (2\theta - \omega)] \\ q_z &= \frac{1}{\lambda} [\sin \omega + \sin (2\theta - \omega)] \end{aligned} \quad (2.12)$$

Where, λ is the wavelength of incident X-ray beam, ω is the angle which incident X-ray makes with the sample surface and 2θ is the angle between incident and diffracted X-ray beams. Various ω and $\omega/2\theta$ scan peaks are generally fitted by pseudo-Voigt profiles¹²² for finding the Lorentzian component (f) of each scan, FWHM of omega scan (Δq_x) and FWHM of $\omega/2\theta$ scan (Δq_z). The Lorentzian component (f) is converted to a new constant for the ease of subsequent analysis by the following relation:

$$n = 1 + (1 - f)^2 \quad (2.13)$$

Here, ω scan ($\omega/2\theta$ scan) widths are affected mainly by LCL (VCL) and tilt between the mosaic blocks. Note that the instrumental broadening is very less in highly mismatch systems in comparison to other broadenings. ω ($\omega/2\theta$) scans are recorded for at least three parallel reflections to perform a linear fit using the following relation to find intercept $(\Delta q_{LCL})^n$ ($(\Delta q_{VCL})^n$) and slope α^n (ϵ^n):

$$\begin{aligned}
(\Delta q_x)^n &= (\Delta q_{LCL})^n + (\alpha q)^n \\
(\Delta q_z)^n &= (\Delta q_{VCL})^n + (\varepsilon q)^n
\end{aligned}
\tag{2.14}$$

From Williamson-Hall analysis, LCL (VCL) is estimated from the intercept while tilt (micro-strain) is estimated by the slope of ω ($\omega/2\theta$) scans respectively.¹² Misorientation angle (α_{hkl}) estimated from several ω scans of different reflections with specific ψ angles are fitted with the following equation to find twist value i.e. α_{hkl} at $\psi = 90^\circ$;^{12,115}

$$(\alpha_{hkl})^n = (\alpha_{tilt} \cos \varphi)^n + (\alpha_{twist} \sin \varphi)^n \tag{2.15}$$

In case of modified Williamson-Hall analysis, one uses the planes which are inclined with respect the growth plane at a given angle, for example, (LLL) planes (L=1,3,4 etc.) which are inclined with respect to growth plane (100) at 54.7° .¹⁰ Here, the **Equation (2.14)** takes the following form;

$$\begin{aligned}
(\Delta q_x)^n &= (\Delta q_{LCL})^n + (\alpha_{LLL} q)^n \\
(\Delta q_z)^n &= (\Delta q_{(LLL)VCL})^n + (\varepsilon q)^n
\end{aligned}
\tag{2.16}$$

VCL is estimated by using the following relation;

$$VCL = \cos \psi / \Delta q_{(LLL)VCL} \tag{2.17}$$

Chapter 3

Study of the Anisotropic Distribution of Microstructure in GaP/GaAs Epitaxial Layers

3.1 Introduction

High resolution X-ray diffraction (HRXRD) characterization of epitaxial layers is an important step in the development of advanced semiconductor devices like high efficiency multi junction solar cells, and various optoelectronic/spin-phonic devices that are fabricated under a monolithic integration scheme.^{123–125} Epitaxial growth of compound semiconductor materials on foreign substrates is essential for the realization of such devices.^{126–132} In the case of mismatch epitaxy, a large lattice mismatch between the epilayer and substrate often leads to the generation of misfit dislocations in the grown layer.⁶⁸ Furthermore, the strain energy increases with epilayer thickness where the layer is seen to relax through the generation of defects/dislocations beyond a critical value.¹⁴

Understanding the mechanism of strain relaxation is very important for the optimization of epilayer quality grown by the mismatch epitaxy. Nucleation, propagation, and reaction of dislocations govern the ultimate dislocation density that can be achieved for an epilayer grown on a foreign substrate.^{62,71} One often tries to minimize the density of dislocations by implementing such concepts that might otherwise limit the overall performance of a device made out of the mismatched epilayers. Owing to these reasons, the study of dislocation formation and their propagation along different directions is considered to be of great interest. HRXRD and

high resolution transmission electron microscopy (HRTEM) are the preferred techniques for identifying the nature and distribution of dislocations.^{46,51,61,65,68–70,133} HRTEM is the most direct technique that provides unambiguous evidence for the presence of dislocations in the epilayer.^{46,52–54,61,69,134} However, HRTEM is a destructive and highly arduous method where the sample preparation itself requires strenuous efforts. HRXRD, being a non-destructive technique, is generally preferred over HRTEM and is often used for accessing the crystalline quality of grown layers by measuring the full width at half maximum (FWHM) of Bragg diffraction peaks.^{135–138} HRXRD is especially preferred since the growers can access the layer quality rather quickly by simply comparing the FWHM of the corresponding diffraction peaks of respective samples, which helps them in preparing the next growth recipe. However, identification of the types of dislocations that might be present in the layer, is often ignored here. All types of dislocations are generally believed to broaden the diffraction peaks and a low value of FWHM is considered to be a confirmation of good crystalline quality.^{135–138} However, it puts a question on such an analysis since the dislocations distribution in highly mismatched III–V epitaxial layers is often found to be asymmetrical.^{46,52–54,61,65,68,133,134}

It is well known that the dislocations glide with different velocities along the two orthogonal $\langle 011 \rangle$ directions in the $\{111\}$ glide plane for zinc-blende epilayers grown on (100) oriented substrates. In case of III–V epilayers, misfit dislocations with the line of dislocations along $[01\bar{1}]/[011]$ crystallographic directions are known as α/β dislocations, respectively.^{46,51–60} It is also understood that the glide velocity of α dislocations is two orders of magnitude larger than that of the β dislocations.^{52–54,56–58} Because of the difference in their core structures and the glide velocities, α and β

dislocations possess different formation energies, which leads to an asymmetry in the formation of dislocations along the two orthogonal in-plane directions.^{55,61} These are known to be primarily 60° dislocations which glide in the {111} crystallographic plane, but 30° and 90° partial dislocations also glide in the same plane as summarized by Goldman et al.⁵⁹ For a particular layer-substrate combination, specific sets of dislocations nucleate that propagate along different crystallographic directions with their respective glide velocities.^{46,52–54,62,63} It is therefore obvious that the strain relaxation is expected to be anisotropic in III–V epilayers grown on (100) oriented zinc-blende substrates. Moreover, the direction of strain relaxation can be swapped as a function of substrate miscut, dopant, and strain type.^{54,56,64} In general, anisotropic relaxation of epitaxial layer is of considerable interest both from the experimental and theoretical point of view.^{46,54,57,59,65} Therefore, understanding the atomistic mechanism of nucleation of dislocations is very important for the growth of novel heterostructures. Some of the interesting examples where the process of anisotropic strain relaxation is already studied are InGaAs/ GaAs,^{52,55,56,66,67} SiGe/Ge,⁴⁷ GaSb/GaAs,⁶⁸ InSb/GaAs,^{68,69} InAsP/InP,⁷⁰ InGaAs/InP,⁶⁵ etc. A variety of techniques are used to understand the observed anisotropy in the formation of dislocations, for example, HRXRD,^{51,65,68–70,133} variable azimuthal angle ellipsometry,⁶⁵ HRTEM,^{46,61,69} atomic force microscopy (AFM),^{61,65,69,133} cathodoluminescence,⁴⁶ and multi-beam optical stress sensor (MOSS).^{55,139}

In view of the above, one can easily appreciate that the importance of HRXRD measurements on partially relaxed layers is going to be rather limited, unless the asymmetry of dislocation distribution is taken into account. Furthermore, it is of great interest to know if one can comment on the nucleation, propagation, and reaction of

dislocations from the HRXRD measurements. By keeping this in mind, we performed meticulous HRXRD measurements on tensile strained GaP epilayers grown on (100) oriented GaAs substrates. Although the formation of surface undulation with twinning and cracking in GaP/GaAs is known,⁶¹ an anisotropic distribution of microstructure is not yet reported for this material combination. Moreover, innovative designs based on GaP/GaAs material combination¹⁴⁰ are recently reported, for example, in flash memory devices,⁴² next generation non-linear optical devices,^{43,44} and the growth of GaP islands on GaAs substrates.^{141,142} The GaP epilayers that are presented in this chapter are partially relaxed and contain grain-line structures along with a large possibility of anisotropy in mosaicity/microstructure and dislocation distribution. Formation and propagation of dislocations are studied mainly through the HRXRD technique, which is reasonably supported by the AFM and HRTEM images and is found to be in strong corroboration with the knowledge already available in the literature on other material combinations.

It is also noticed that the dislocations density in tensile Strained GaP/GaAs epilayers is different along the two in-plane orthogonal directions where the amount of anisotropy is also to be quantified. For this purpose, a method is proposed for estimating the dislocation density in tensile strained zinc blende epitaxial layers along the two in-plane orthogonal directions where two types of dislocations are predominant along the respective axis. It is especially important since the conventional methods are almost insensitive to the type of dislocations and are therefore unable to identify the asymmetry in dislocation density. With the help of proposed method, the density of 90° partial dislocations predominant along [011] direction and 60° perfect dislocations

predominant along [01 1] direction is successfully measured for tensile strained GaP/GaAs epilayer.

3.2 Experimental details

GaP/GaAs heterostructures are grown using metal organic vapor phase epitaxy reactor (AIX-200) at 50 mbar pressure. GaP layer of 1200 Å is grown at 660 °C growth temperature using phosphine and trimethylgallium source materials where the other growth details are presented elsewhere.¹⁴³ GaAs substrates are 400 µm thick and are oriented along [100] with a nominal miscut of 0.2° along the [011] direction. HRXRD measurements are performed by using a PANalytical X'PERT diffractometer equipped with Cu K α_1 X-rays ($\lambda = 1.54056$ Å) and a hybrid four-bounce crystal monochromator of beam divergence of ≈ 20 arc sec. The line-focus mode of HRXRD with typical footprint of 15 mm \times 2 mm is used for investigating the anisotropic distribution of the microstructure. Omega (ω) and Omega/2 Theta ($\omega/2\theta$) open detector scans are recorded with 1° open detector. Symbols ω (θ) stand for the angle between incident X-ray and sample surface (reflecting plane), respectively.^{12,82,144} Further, reciprocal space maps (RSMs) are recorded for {422} reflection with the sample oriented along either the [011] or [01 1] crystallographic directions perpendicular to the diffraction plane.^{52,54,145} RSMs are recorded either in the triple axis geometry with a three bounce Ge (220) crystal analyser of ≈ 12 arc sec acceptance angle or in the open detector geometry with an opening of $\approx \frac{1^\circ}{8}$. In the later case, a $\frac{1^\circ}{8}$ slit was inserted in front of the open detector for improving the signal-to-noise (S/N) ratio and also for the rapid acquisition of data. It was observed that the FWHM of diffraction peaks is quite similar in both the cases as the two values lie within $\pm 1\%$. Note that the FWHM of diffraction patterns is

typically five to six times larger than the instrumental broadening. Therefore, the instrumental broadening effects have been neglected during the data analysis.¹⁴⁶ Further, Williamson-Hall analysis is performed on the symmetric (200), (400), (600) planes, which are perpendicular to the growth direction [100] and also along the skew-symmetric planes (133), (422), (511), (311), which are inclined at an angle (ψ) from the growth direction.^{5,49,119} In order to study the anisotropy in epilayer, the sample is rotated around the growth direction by an angle ϕ as shown in **Figure 3.1**. In order to record the skew-symmetric reflections, the sample is rotated by an angle ω around the direction of X-ray projection. Cross sectional HRTEM micrographs were recorded using Philips CM200 at an accelerated voltage of 200 kV. Cross-sectional samples were prepared by the conventional procedures involving mechanical thinning followed by Ar-ion milling. AFM measurements were performed using a multi-mode scanning probe microscope (NT-MDT, SOLVER-PRO, Russia). Silicon cantilever tips having a radius of curvature of ≈ 10 nm, resonant frequency ≈ 190 kHz, and spring constant ≈ 5.5 N/m were used in a non-contact mode for the AFM measurement.

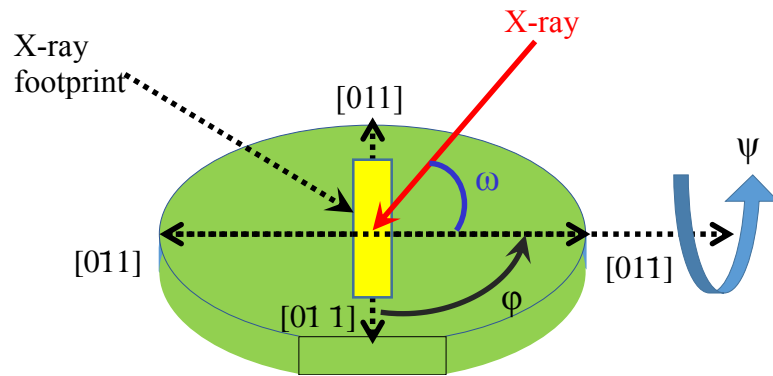


Figure 3.1 HRXRD configuration for studying the anisotropy in epilayer where the sample is rotated around the growth direction by an angle ϕ . For skew-symmetric HRXRD scans, the sample is rotated by an angle ψ around the direction of the projection of incident X-ray beam.

3.3 Results and discussion

3.3.1 Observation of anisotropic distribution of microstructure in GaP/GaAs epitaxial layers

Figure 3.2 shows four $\omega/2\theta$ -scans for (400) reflections recorded at 0° , 90° , 180° , and 270° azimuths. Diffraction peaks corresponding to GaP layer and GaAs substrates are clearly observed at all the four azimuths; however, it is found that the angular separation between the layer and substrate peaks is identical for 0° , 180° , and also for 90° , 270° azimuths. Diffraction peaks corresponding to $0^\circ/90^\circ$ azimuths are separated from the respective peaks at $180^\circ/270^\circ$ azimuths by 0.02° . At $\varphi = 0^\circ$, the projection of incident X-ray beam is taken to be along $[01\ 1]$, whereas its footprint lies aligned along the $[011]$ direction as clearly shown in **Figure 3.1**. Similarly at 90° , 180° , and 270° azimuths, the footprint of incident X-ray beam lies along $[011]$, $[0\bar{1}1]$, and $[01\ 1]$ directions, respectively, as can be easily appreciated from **Figure 3.1**. Note that the opening of the detector is parallel to the footprint of incident X-ray beam. HRXRD measurements performed at 0° (180°) and 90° (270°) azimuths examine the epilayer

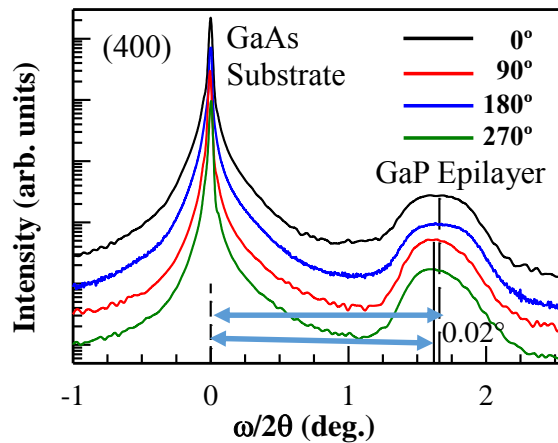


Figure 3.2 HRXRD pattern of GaP/GaAs epitaxial layer for (400) reflection recorded at 0° , 90° , 180° , and 270° azimuths.

along the respective crystallographic directions as clearly described in **Figure 3.1**. Therefore, the observed difference in the peak separations for 0° (180°) and 90° (270°) azimuths in **Figure 3.1** indicates that there exists an anisotropy in the microstructures of GaP epilayer along [011] and [01 $\bar{1}$] directions.

It is further noted that the critical thickness of GaP epilayer layer on GaAs substrate is 20 Å^{147,148} while the thickness of GaP epilayer in our case is \approx 1200 Å. Therefore, the GaP layer is expected to be relaxed through the generation of misfit dislocations.^{47,55,66,149} As mentioned in **Section 3.1**, the misfit dislocations glide with different velocities along the two in-plane orthogonal crystallographic directions where the velocity of α dislocations is expected to be larger than that of the β dislocations for zinc-blende epilayers.^{46,52,54,56–58,150} In order to explore this point further, RSM scans at 0° and 90° azimuths for (42 2) and (422) reflections are recorded, which are shown in **Figure 3.3**. The values of relaxation (R) are measured using the following relation.^{82,151,152}

$$R(\%) = \frac{\Delta x \times 100}{L \times m} \quad (3.1)$$

where, L, ΔX , and m stand for the layer peak position, layer-substrate peaks separation on the q_x axis in reciprocal space, and lattice mismatch between substrate and relaxed layer, respectively. The values of L and ΔX are measured from the RSM plots shown in **Figure 3.3**. Estimated values of relaxation for the two azimuths are shown in **Table 3.1**. It is found that the relaxation is larger by 10% along the [011] direction in comparison to the value measured for [01 $\bar{1}$] direction. It confirms that the relaxation of GaP layer is of an anisotropic nature, which indicates about the anisotropic distribution of defects/dislocations along the two orthogonal crystallographic

directions. The anisotropic nature of the relaxation process leads to anisotropy in crystallographic broadening, which leads to the observed variation in the values of FWHM of ω scans for (400) reflections seen in **Figure 3.4**. It is therefore obvious that one needs to understand the anisotropic nature of the relaxation process before comparing the FWHM of ω scans for hetero-epitaxial layers as often reported in the literature.¹³⁵ For the measurements shown in **Figure 3.4**, several rocking curves are recorded at different azimuths varying from 0 to 360° in the step of 11.25°. It is observed that the value of FWHM of ω scans is larger along [011]/[011] in comparison to the [011]/[011] directions. It indicates that the density of defects/dislocations is high along [011] in comparison to [011] direction. It is in corroboration with the results obtained

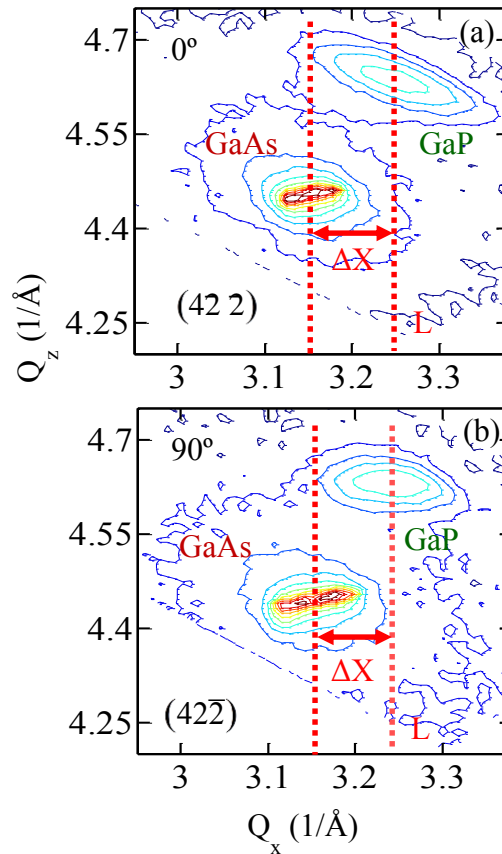


Figure 3.3 Reciprocal space maps of GaP/GaAs epitaxial layer for (a) (42 2) reflection at 0° azimuth, and (b) (422) reflection at 90° azimuth.

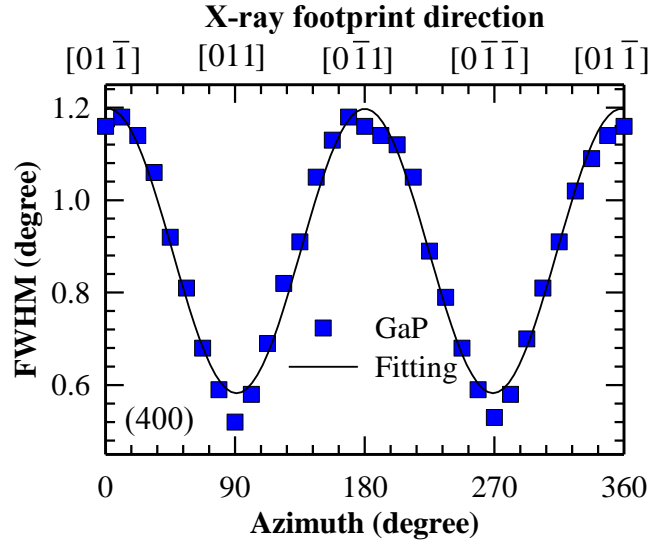


Figure 3.4 FWHMs of ω scans for (400) HRXRD pattern plotted as a function of azimuth where the solid line is a guide to eye.

from $\omega/2\theta$ and RSM scans. One can therefore conclude that the two orthogonal directions are significantly different when the density of defects/dislocations is considered for optimizing the layer quality. Furthermore, anisotropic behaviour of relaxation process is expected to yield very different values of microstructural parameters like lateral coherence length (LCL), tilt, and twist, etc., along the two orthogonal directions, i.e., [011] and [01 $\bar{1}$], respectively. The value of LCL especially can be vastly different when HRXRD measurements are performed along various crystallographic directions. One therefore needs to be extremely cautious while comparing the value of microstructural parameters of the two samples. Extreme care needs to be taken to ensure that the same crystallographic direction in HRXRD measurements is selected while comparing different samples.

In order to observe the effect of anisotropic distributions of defects/dislocations on the microstructural parameters, Williamson-Hall analysis is performed using ω -scans of symmetric (200), (400), and (600) and skew-symmetric (133), (422), (511),

and (311) reflections for both 0° and 90° azimuths. In the Williamson-Hall analysis,^{1,5,114} FWHMs of peaks (Δq_x) of ω -scans are obtained by fitting a pseudo-Voigt function.^{49,122} In this function, the Lorentzian component (f) is related as $n=1+(1-f)^2$, where $n = 1$ for Lorentzian and $n = 2$ for Gaussian like nature of the peak. Subsequently, a linear fit of $(\Delta q_x)^n$ versus q^n curve is used for estimating the values of the microstructural parameters as per the following relation:^{2,12,49,153}

$$(\Delta q_x)^n = (\Delta q_L)^n + (\alpha_{hkl} \times q)^n \quad (3.2)$$

where Δq_L is related to the lateral coherence length $LCL = \frac{1}{\Delta q_L}$. The parameter α_{hkl} defines the tilt between the grains in the GaP epilayer in case of symmetric HRXRD scans. The values of LCL and tilt can be measured from the intercept and slope of the plot shown in **Figure 3.5(a)**. In order to estimate the values of twist, the value of parameter α_{hkl} is measured for several skew-symmetric reflections using the same procedure. Thereafter, twist is measured using the following equation:^{2,5}

$$(\alpha_{hkl})^n = (\alpha_{Tilt} \times \cos \psi)^n + (\alpha_{Twist} \times \sin \psi)^n \quad (3.3)$$

At $\psi = 0^\circ/90^\circ$, α_{hkl} gives the value of tilt (α_{Tilt})/twist (α_{Twist}), respectively. **Figure 3.5(a)** shows the Williamson-Hall plots for GaP/GaAs heterostructure at 0° and 90° azimuths. The measured values of n , R , LCL, tilt, and twist for GaP layer are given in **Table 3.1**. A large value of n for [011] in comparison to [01 $\bar{1}$] direction indicates about the predominantly Gaussian like nature of diffraction peak. It indicates that more defects are present along the [011] direction in comparison to [01 $\bar{1}$] direction. Note that a large value of LCL along [01 $\bar{1}$] direction compared to the [011] direction confirms that the

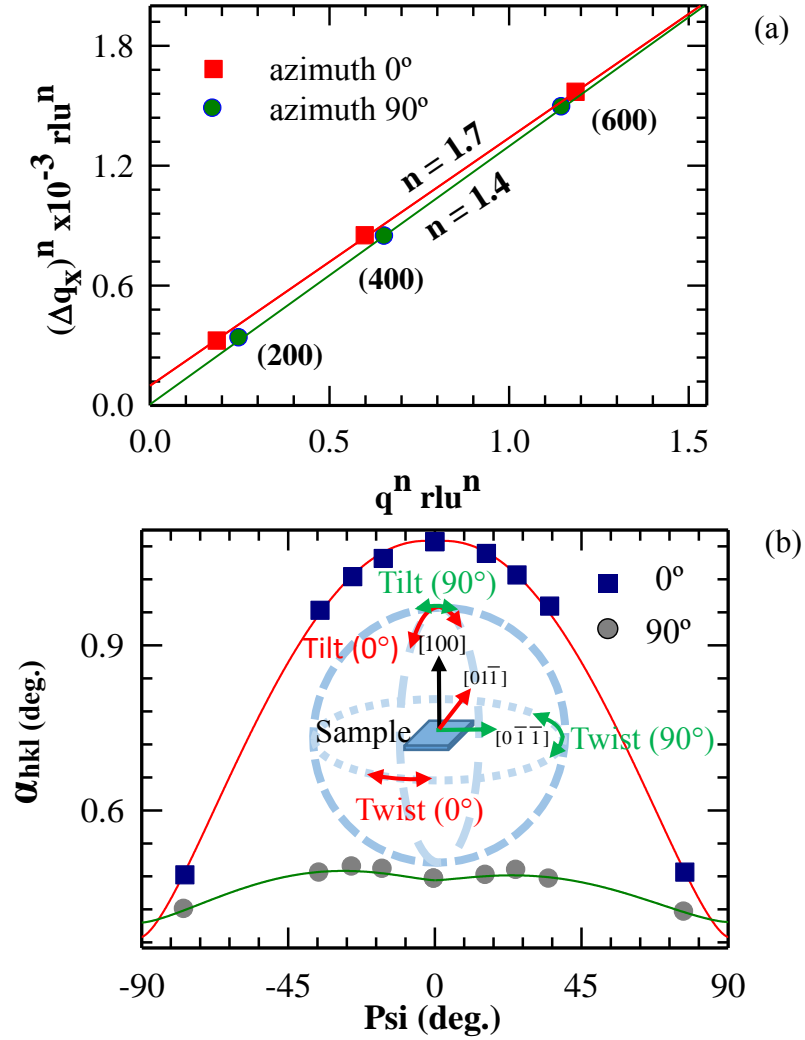


Figure 3.5 (a) Linear fit of $(\Delta q_x)^n$ plot with $(\alpha_{hkl})^n$ at 0° and 90° azimuths for the Williamson-Hall analysis, and (b) variation of α_{hkl} for several skew-symmetric reflections where the inset shows the distribution of tilt and twist along different crystallographic directions.

crystalline quality of GaP layer is superior along the $[01\bar{1}]$ direction. Further, the measured values of α_{hkl} are plotted in **Figure 3.5(b)**, which are estimated by performing numerous ω -scans at the two azimuths.

It is quite interesting to note that the values of twist along the two in-plane orthogonal directions are nearly the same as shown in **Table 3.1**. On the other hand, the value of tilt is quite different for the two azimuths. It clearly indicates about the

anisotropic distribution of defects/dislocations in the GaP epilayer. It can be easily appreciated by considering the schematic diagram shown in the inset of **Figure 3.5(b)** where the distribution of tilt and twist along various directions is illustrated. Note that the ratio of tilt/twist along $[011]$ and $[01\bar{1}]$ directions is 2.9 and 1.3, respectively, which clearly indicates about the anisotropic distribution of relaxation in the GaP epilayer. Although the anisotropic distribution of dislocations is already reported for several zinc-blende materials,^{61,65,68,154} the anisotropic behaviour of microstructural parameters is not yet available in the literature except for some preliminary work of Qiu et al.¹⁵⁵ on GaSb epilayers.

In order to observe the effect of anisotropic distribution of defects/dislocations on the surface topography, the grain size of the microstructures is measured by AFM along the two orthogonal directions as shown in **Figure 3.6**. The AFM image shows that the grains are larger in size along the $[01\bar{1}]$ direction compared to $[011]$ direction, which is in strong corroboration with the results of the Williamson-Hall analysis.

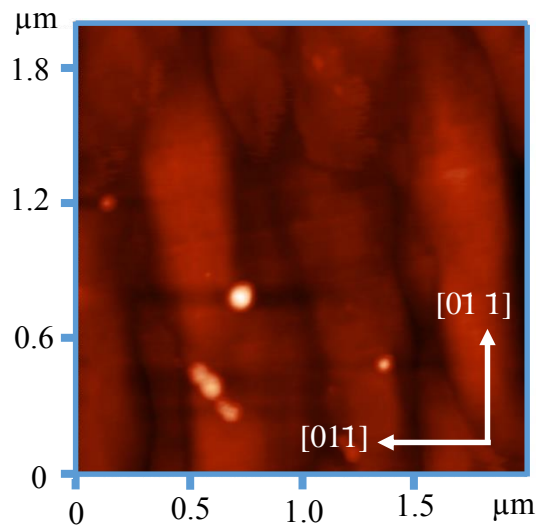


Figure 3.6 AFM image of GaP/GaAs epitaxial layer that shows anisotropic distribution of grains along $[01\bar{1}]$ and $[011]$ directions.

HRXRD and AFM measurements confirm that the GaP layer grown on GaAs shows a significantly large anisotropy in the microstructures. The origin of anisotropy predominantly lies with the nucleation kinetics of dislocations, which is explained in subsequent paragraphs.

When an epitaxial layer is grown on the substrate, it remains structurally coherent with the substrate without the generation of any defects/dislocations as long as the thickness of the layer remains below the critical layer thickness. Once the critical layer thickness is exceeded, the growing layer starts relieving the excess strain energy through the lattice relaxation process where the formation of defects/dislocations is mandatory.^{47,55,67,156} In general, defects in III–V semiconductors are predominantly one dimensional defects like 60° perfect dislocations and two dimensional like stacking fault and twin boundary (linked with 30° and 90° partial dislocations).^{59,61,157,158} Perfect and partial dislocations both can have a line of dislocations along any of the $\langle 011 \rangle$ directions. In the past, many groups have identified the asymmetric dislocation propagation along the $[011]$ and $[01\bar{1}]$ directions that is associated with the difference in the mobility of dislocations gliding along different crystallographic directions.^{46,52,53,53–55,57,65} In the tensile strained system, the dislocations having a line of dislocation along $[01\bar{1}]$ are known as α dislocations, while those having a line of dislocation along $[011]$ are called β dislocations.^{46,52} Furthermore, the glide velocity of α dislocations is much larger than that of β dislocations and the same is true for all the epilayers irrespective of their strain state, i.e., compressive or tensile.⁴⁶ The only difference is that the line of dislocations of α and β dislocations switches while going from tensile to compressive strain as clearly explained by Matragrano et al.⁴⁶

It has already been reported in the literature that the 60° dislocations have the line of dislocation along the $[011]$ direction while the partial dislocations (30° and 90°) glide along the $[01\bar{1}]$ direction in the tensile strained zinc-blende structures as shown in **Figure 3.7**.^{55,61,159} In general, 90° perfect/partial dislocations, 30° partial dislocations, and 60° perfect dislocations can contribute to the relaxation process.⁶³ It is also known that 90° perfect dislocations cannot glide into or out of the interfacial plane because a dislocation can glide only in the plane defined by its Burgers vector and line of dislocations.¹⁶⁰ Therefore, 90° perfect dislocations do not participate in the initial relaxation of pseudomorphic strained layers.¹⁶⁰ Two 60° dislocations can in principle react to form one Lomer (90° perfect) dislocation for reducing the core energy of dislocations. However, the probability of having two 60° perfect dislocations sharing the same dislocation line and appropriate Burgers vector that can combine to meet at the interface is rather minimal. Therefore, the possibility of such a dislocation reaction is extremely small.¹⁶¹ In case of tensile strained layers, partial dislocations nucleate in the beginning because of their low formation energy when compared with the perfect dislocations.^{47,63} If growth conditions are favourable, then both the 90° and 30° partial dislocations can combine to form a 60° perfect dislocation.¹⁴ However, in tensile strained layers, 90° (30°) partial dislocations make an angle of 0° (60°) with respect to the resolved shear stress vector, respectively.⁶³ It therefore implies that the force exerted by the shear stress field on 90° partial dislocations is twice when compared with that on the 30° partial dislocations.¹⁴ Due to this factor, 90° partial dislocations nucleate predominantly in case of tensile strained epilayers.^{63,64} Such 90° partial dislocations glide towards the interface and therefore produce stacking faults in its wake.⁶³ It indicates about the prevalence of 90° partial dislocations over 30° partial dislocations

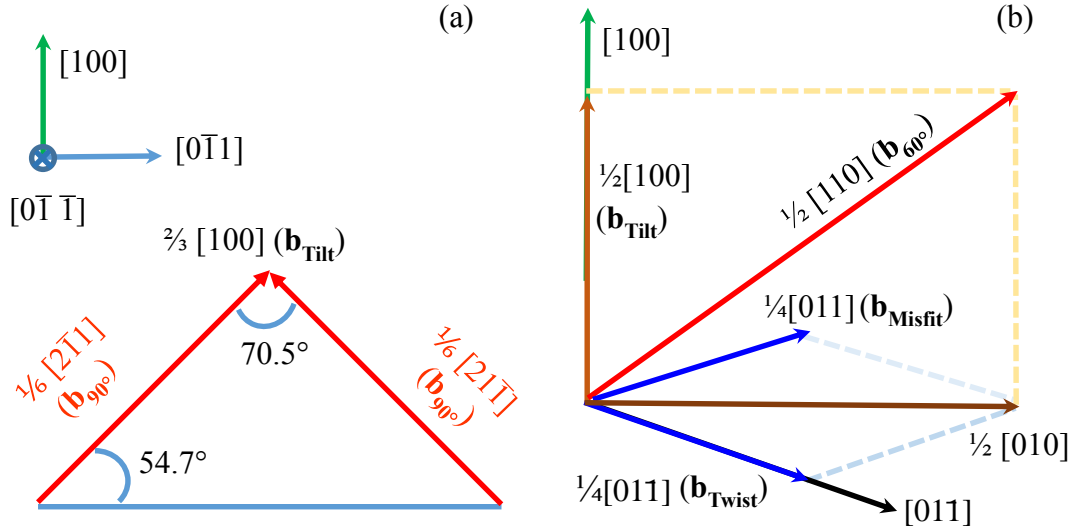


Figure 3.7 (a) 90° partial dislocations reacting to give an edge dislocation, line of dislocation is shown along $[01\ 1]$ direction, and **(b)** the components of 60° perfect dislocations where the line of dislocation is shown along $[011]$ direction.

in our case.⁶¹ Under such conditions, 90° partial dislocations with a Burgers vector of $\frac{1}{6}[211]$ react with another set of 90° partial dislocations having a Burgers vector of $\frac{1}{6}[211]$ to form an edge dislocation. The dislocation reaction can be given as follows:

$$\frac{a}{6}[211] + \frac{a}{6}[211] = \frac{2a}{3}[100] \quad (3.4)$$

Once the epilayer thickness exceeds the critical layer thickness, the formation of partial dislocations and their reactions can help in relieving the strain during the initial phase of growth as given by **Eq. (3.4)**. The formation of such dislocations is shown in **Figure 3.7(a)**, which glides along the $[01\ 1]$ crystallographic direction. Li et al.¹⁵⁷ have made a similar observation in case of nanowires where two 30° partial dislocations react to form an edge dislocation. Furthermore, it is generally understood that the partial dislocations

must necessarily border a two-dimensional defect, usually a stacking fault since the Burgers vector of a partial dislocation does not link two lattice points in a crystal.¹⁶² When occurring on adjacent atomic planes, the stacking faults form micro-twins, which are usually seen in HRTEM images, and the same is observed in **Figure 3.8**¹⁶² Therefore, the observation of V shaped configuration of stacking faults in an HRTEM image clearly suggests that the stacking fault is formed due to the coalescence of islands.¹⁶¹ Hence, the prevalence of 90° partial dislocations in GaP/GaAs epilayer is

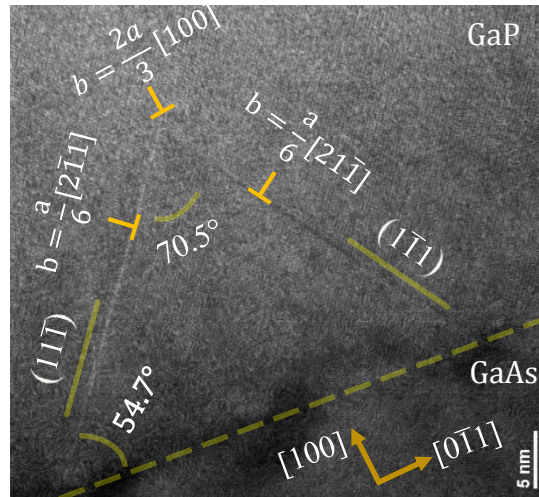


Figure 3.8 HRTEM image of GaP/GaAs epitaxial layers showing the formation of stacking fault ribbons and a highly defected interface for cross section orientation.

mainly responsible for the observation of stacking faults in our case. Note that in all the HRTEM images recorded by us, only a single stacking fault is observed as shown in **Figure 3.8**. It is due to the choice of small image size/high resolution in our case. On the other hand, Li and Niewczas⁶¹ have recorded a large size image (≈ 20 times that of ours) for the same material combination, where they observed many stacking faults spread over a large area.

Once the epilayer thickness becomes sufficiently large, it can lead to the substantial relaxation of layer where 60° perfect dislocations can relieve the strain as commonly observed in III–V semiconductors.^{47,55,66} The line of dislocation of 60° perfect dislocations is at a right angle to [01 1] direction as shown in **Figure 3.7(b)**. In case of zinc-blende epilayers, strain in the epilayer is predominantly relieved by the fast moving α dislocations during the initial phase of growth, while the remaining fraction of strain is relieved by β dislocations (60° perfect dislocations in the present case).^{47,55} Similar observations have been made by several groups in other material systems. For example, in the case of a SiGe/Ge material combination, Dynna and Marty⁴⁷ reported that the strain is relieved by 90° partial dislocations up to a film thickness of 13 nm after which the relaxation via 60° perfect dislocations is energetically favoured. Similar observations are made by Peiró et al.⁶⁶ for InGaAs/GaAs system, where they reported that at the onset of strain relaxation process and for small layer thickness, 90° partial dislocations nucleate and propagate, leaving a stacking fault behind. Further, at large layer thickness, they reported the nucleation of 60° perfect dislocations and concluded that the partial dislocations and stacking faults do not arise from the dissociation of perfect dislocations but those must nucleate independently.

For the 60° dislocations gliding along the [011] direction, the Burgers vector has three components as shown in **Figure 3.7(b)** and the corresponding dislocation reaction is given below

$$\frac{a}{2} [110] (b_{60^\circ}) = \frac{a}{4} [011] (b_{\text{Misfit}}) + \frac{a}{4} [011] (b_{\text{Twist}}) + \frac{a}{2} [100] (b_{\text{Tilt}}) \quad (3.5)$$

The three components are (1) a misfit component with a Burgers vector of $b_{\text{Misfit}} = \frac{1}{4} [011]$ on the interface plane, (2) a twist (screw) component with a Burgers vector of $b_{\text{Twist}} = \frac{1}{4} [011]$ on the interface plane, and (3) a tilt component with a Burgers vector of $b_{\text{Tilt}} = \frac{1}{2} [100]$ along the growth direction.^{68,152} It is to be noted that the misfit component is related to the strain in the GaP epilayer, the twist(screw) component is related to the in-plane rotation of mosaic blocks, and the tilt component is responsible for the out-of-plane rotation of the mosaic blocks.⁴ By considering the magnitude of respective Burgers vectors, the ratio of tilt/twist components is expected to be 1.4.⁴ It is interesting to note that the ratio of the tilt and twist value along the $[01\ 1]$ direction is ≈ 1.3 for GaP/GaAs heterostructures as shown in **Table 3.1**. This indicates that the 60° dislocations (β) glide along the $[011]$ direction for GaP/GaAs heterostructures. However, the tilt/twist ratio along the $[011]$ direction is ≈ 2.9 as shown in **Table 3.1**. It therefore indicates that the relaxation along this particular direction cannot be attributed to 60° dislocations alone. It might be influenced by the formation of 90° partial dislocations (α) as mentioned earlier.

Further support for the anisotropic distributions of defects/dislocations can be obtained from the cross sectional HRTEM images of the MOVPE grown GaP/GaAs heterostructure, and a representative image is shown in **Figure 3.8**. The HRTEM image shows a dark line perpendicular to the $[111]$ direction, which intersects another dark line perpendicular to $[111]$ direction at 70.5° . The two dark lines correspond to rotational twins (111) and $(\bar{1}\bar{1}\bar{1})$ and stacking faults.^{150,157,163,164} These stacking faults are formed because of their low formation energies.¹⁵⁰ The stacking faults and twin

formation are attributed to the formation of partial dislocations.^{63,150,165} The two 90° partial dislocations with Burgers vectors of $\frac{1}{6} [211]$ and $\frac{1}{6} [\bar{2}11]$ are shown in **Figure 3.7(a)**. They form an edge dislocation with the line of dislocation along $[01\bar{1}]$ having a Burgers vector of $\frac{2}{3} [100]$.¹⁵⁷ Edge dislocations relieve the misfit strain and are responsible for the generation of stacking faults and twin planes. Thus, large tilt and relaxation values along the $[011]$ direction can be attributed to the stacking faults and twinning due to the formation of associated 90° partial dislocations in the tensile strained GaP epilayer. It leads to the observed anisotropy in the crystal relaxation process.

Finally, it is worthwhile to discuss the impact of wafer bowing on the anisotropic distribution of dislocations. Bowing is found to be critically important in GaAs layers grown on Silicon where a large difference exists between the thermal expansion coefficients of layer and substrate as high as 123%. However, Lum et al.¹⁶⁶ have shown that the wafer bowing was eliminated for GaAs layers grown on 1000 micron thick Si wafers. They also reported that the bowing was found to be negligible in GaAs/Si films when the film thickness was lower than 1 micron. Note that the difference in the thermal expansion coefficients of GaP and GaAs is only 10%. In our sample, GaP film is only 1200 Å thick and is mosaic in nature. Therefore, the effect of bowing can be neglected in our case.

Table 3.1 Summary of the microstructural parameters of GaP/GaAs epitaxial layer obtained from the Williamson-Hall analysis of HRXRD data.

Azimuth (deg.)	X-ray foot- print direction (Line of dislocations)	Glide Planes	Relaxation (R) (%)	WH analysis				Dominant dislocations	Dislocation density estimated by using Eqn. (3.9) (cm ⁻²)	Dislocation density estimated by using Eqns. (3.6) [(3.7)] (cm ⁻²)
				<i>n</i>	LCL (μm)	Tilt and Twist				
						Tilt (Twist) (deg.)	Ratio			
0	[01 $\bar{1}$]($[0\bar{1}\bar{1}]$ -α)	(111) & (111)	85	1.7	0.04± 0.01	1.1 (0.38)	2.9	90° Partial	1.7×10 ¹¹	3.3×10 ¹⁰ [5.6×10 ¹⁰]
90	$[0\bar{1}\bar{1}]$ ($[01\bar{1}]$ -β)	(111) & (11 1)	75	1.4	0.65± 0.01	0.5 (0.38)	1.3	60° Perfect	2.1×10 ¹⁰	6.9×10 ⁹ [1.1×10 ¹⁰]

3.3.2 Anisotropic distribution of dislocations density in tensile strained GaP/GaAs epilayers

A systematic variation of FWHMs with azimuth is clearly seen in **Figure 3.4**. The values of FWHM of rocking curves vary a lot as a function of azimuths (ϕ) which indicates about a significant variation in the dislocation density across the sample. It clearly confirms that the distribution of dislocations on $\{111\}$ glide planes is nonuniform.^{68,133} A large FWHM at 0° azimuth indicates that dislocations with (111) and $(\bar{1}\bar{1}\bar{1})$ glide planes are large in number compared to the dislocations along the remaining two glide planes.^{68,133,167} The values of FWHM at 0° and 180° azimuth are nearly same indicating that the dislocations are equally distributed on (111) and $(\bar{1}\bar{1}\bar{1})$ glide planes.^{68,133,167} Similarly, the dislocations are equally distributed on (111) and $(1\bar{1}\bar{1})$ glide planes.^{68,133,167} An equal distribution of dislocations on (111) and $(11\bar{1})$ / $[(111) \text{ and } (11\bar{1})]$ glide planes also confirms that the substrate is nearly exactly oriented and is having a nominal miscut.⁶⁸ Yarlagadda et al.¹³³ had proposed a formula based on the mosaic block model, where the values of dislocation density (D) at 0° (D_{0°) and 90° (D_{90°) azimuths are measured by using the following expression;

$$D_{0^\circ/90^\circ} = \frac{\text{FWHM}_{0^\circ/90^\circ}^2}{8.7 \times b^2} \quad (3.6)$$

b is the magnitude of Burgers vector of 60° perfect dislocations which is assumed to be $b = \frac{a}{\sqrt{2}}$; a being the lattice constant of layer. In mosaic block model, it is assumed that the strain is primarily relieved via the formation of 60° perfect dislocations along both the azimuths and grain size is of the order of coherence

length.¹⁶⁸ Mosaic block model is also applied by other researchers for finding the dislocation density but their formula contains an explicit mention of coherence length.¹⁶⁹ In spite of applying Mosaic block model for determining the dislocation density in case of an asymmetric distributions, Yarlagadda et al.¹³³ approach does not consider the coherence length of grains. Contrary to the observations of Yarlagadda et al.¹³³, where they assumed the presence of only 60° perfect dislocation along the two in-plane orthogonal directions, in earlier section² we reported that the same is not true in our case. For tensile strained GaP/GaAs epilayers, 90° partial dislocations with Burgers vector of type $\frac{1}{6} [211]$ and line of dislocation along $[01\bar{1}]/[011]$ (α dislocations) contribute to the initial relaxation of epilayer and after reaching a certain thickness, 60° perfect dislocations with Burgers vector of type $\frac{1}{2} [110]$ and line of dislocation along $[011]/[011]$ (β dislocations) dominate the growth.^{2,47,55,63,66} Therefore, the value of FWHM recorded at 0° azimuth is related to 90° partial dislocations while the one at 90° azimuth is related to 60° perfect dislocations. Further, Yarlagadda et al.¹³³ did not consider the fitting of rocking curve with a pseudo-Voigt function which is generally preferred over Gaussian.^{2,4,5,49,122} Furthermore, FWHM of an omega scan is mainly affected by size broadening i.e. lateral coherence length (LCL) and angle misorientation between the mosaics blocks i.e. tilt (α_{Tilt}).^{2,5,49} In light of aforementioned discussion, it is therefore clear that the usage of FWHM term in the formula proposed by Yarlagadda et al.¹³³ (**Eq. (3.6)**) is inappropriate for GaP/GaAs epilayers. Further, symmetric omega scans^{5,12,170} carry the information of Burgers vector along $[100]$ direction. Moreover, 60° perfect dislocations do not lie along $[100]$ direction and it is only the tilt part that lies along $[100]$ direction.² For this reason, the magnitude of Burgers vector of 60°

perfect dislocations taken in the formula proposed by Yarlagaadda et al.¹³³ is not justified in the present case. Therefore, the usage of such a simple procedure for estimating the values of dislocation density in tensile strained GaP/GaAs layers will be inappropriate. A modified procedure is therefore necessary in order to make it suitable for evaluating the dislocation density in our sample. In this context, it is essential to isolate the contribution of LCL from FWHM and to know the Burgers vector or Burgers vector's components that are responsible for tilt before estimating the values of dislocation density.

Models based on mosaic structure^{121,133,169,171} and on random distribution of dislocations^{171–175} have been used for estimating the dislocation density for many material combinations^{121,169}. Recently, Nemoz et al.¹⁷¹ have shown that the value of dislocation density estimated using a model based on random distribution of dislocations namely proposed by Dunn et al.¹⁷² closely matches with the dislocation density measured from HRTEM experiments. It is also important to note that the model based on random distribution of dislocations proposed by Dunn et al.¹⁷², which is a slightly modified version of the formalism originally proposed by Gay et al.¹⁷⁴, is being extensively used in case of wurtzite materials systems especially those which are prone to high dislocation densities.^{121,169,173,176–181} This formula uses two parameters viz. misorientation angle (α) and magnitude of Burgers vector (b) responsible for the misorientation and is of the following form:^{117,169,171}

$$D = \frac{\alpha^2}{4.35 \times b^2} \quad (3.7)$$

For wurtzite material systems, misorientation angle and Burgers vectors responsible for misorientation are explicitly known which is the primary reason for its

widespread usage in such material combinations.^{117,121,169,173,176–181} However, as reported by us in earlier section² on zinc-blende tensile strained system, different types of dislocations are predominantly acting along the two in-plane orthogonal directions. Moreover, the factors leading to misorientation in epilayers depends upon the type of strain which governs the type of dominant dislocations that might be present in a layer.

In view of this, **Eq. (3.7)** needs to be modified by considering 1) the type of dislocations which might be dominant along a given direction as known in the present case² and 2) the factors/mechanism leading to the tilt shall be known a priori. Accordingly, the value of misorientation angle (α) and magnitude of Burgers vector (b) shall be inserted in **Eqn. (3.7)** for estimating the values of dislocation density. Therefore, in our case it is essential to find the tilt at each azimuth along with the Burgers vector of dominant dislocations primarily responsible for the tilt. To isolate the tilt component from the value of FWHM, we have carried out systematic WH analysis^{2,12} where the results are summarized in **Table 3.1**.

The values of α_{Tilt} for 0° ($\alpha_{[01\bar{1}]}$) and 90° azimuths ($\alpha_{[011]}$) are estimated to be 1.1° and 0.5° respectively. It is also very important to note that the intercept on y-axis (c) is related to the inverse of LCL, which in general has a very small value. One therefore expect a large error in case of the estimated values of LCL. On the other hand the value of tilt, which is estimated from the slope of the curve, can be estimated rather precisely. It provides another valid reason why one should use the formula based on random distribution modal^{117,169,171} in comparison to the mosaic block modal.^{153,169}

In earlier section², we have shown that at 0° azimuth, 90° partial dislocations are responsible for the tilt. This can be appreciated with the help of **Figure 3.8** which shows cross sectional HRTEM image of the sample. Note that the formation of stacking

faults and highly defective interface is clearly visible. It is known that 90° partial dislocations in tensile strained systems generate stacking faults in its wake.⁶³ The stacking faults are generated on adjacent {111} planes and micro-twins are then formed which are clearly visible in a V-shaped configuration as shown in **Figure 3.8**.^{161,162}

Essentially, the two 90° partial dislocations meet and create a Burgers vector ($b = \frac{a}{\sqrt{6}}$) along [100] direction which is responsible for the tilt at 0° azimuth as shown in **Figure 3.8**, where the dislocation reaction is given below;¹⁶³

$$\frac{a}{6} [211] + \frac{a}{6} [2\bar{1}1] = \frac{2a}{3} [100] \quad (3.8)$$

On the other hand at 90° azimuth, 60° perfect dislocations are responsible for tilt.² It is the edge component $\frac{1}{2} [110]$ ($b = \frac{a}{2}$) of Burgers vector of 60° perfect dislocations which is associated with tilt in grains of the mosaic sample.^{2,14,152}

In view of the aforementioned discussion, **Eq. (3.7)** is modified for measuring the values of dislocation density by measuring $\alpha_{[01\bar{1}]}$ and $\alpha_{[011]}$ independently and by inserting the magnitude of Burgers vector of 90° partial dislocations and edge component of 60° perfect dislocations as described below;

$$\begin{aligned} D_{90^\circ \text{ partial dislocations}} &= \frac{6\alpha_{[0\bar{1}\bar{1}]}^2}{4.35a^2} \\ D_{60^\circ \text{ perfect dislocations}} &= \frac{4\alpha_{[01\bar{1}]}^2}{4.35a^2} \end{aligned} \quad (3.9)$$

The values of dislocation density of 90° partial dislocations and 60° perfect dislocations are found to be $1.7 \times 10^{11} \text{ cm}^{-2}$ and $2.1 \times 10^{10} \text{ cm}^{-2}$ respectively as shown in

Table 3.1. There is nearly one order of difference between the magnitude of dislocation density of 90° partial dislocations and 60° perfect dislocations. It is in good agreement with the observation reported in the literature for other tensile strained systems e.g. SiGe/Ge⁴⁷, InGaAs/GaAs⁶⁶ etc. This is also in agreement with the reports available in literature where the initial relaxation of layer proceeds through the formation of α type dislocations having $[01\bar{1}]$ line of dislocations which is followed by β type dislocations having $[011]$ line of dislocations in zinc-blende tensile strained systems.^{2,47} It is interesting to compare the values of dislocation density estimated by using **Eq. (3.6)** and **Eq. (3.7)** with those obtained via the modified method (**Eq. (3.9)**). The corresponding values are shown in **Table 3.1**. It is found that the density of dislocations is underestimated by the earlier methods due to an inappropriate choice of Burgers vector associated by the respective dislocations and/or the usage of FWHM in lieu of tilt. Moreover, the density of 90° partial dislocations, which play a key role in the initial relaxation of tensile strained epilayers, cannot be estimated from the earlier methods.

3.4 Conclusion

Anisotropic distribution of microstructure in GaP layer grown on GaAs is investigated from the Omega/2Theta scans for (400) reflections for 0° (180°) and 90° (270°) azimuths along $[01\bar{1}]$ and $[011]$ directions. The values of relaxations are measured for both the orthogonal in-plane directions such as $[01\bar{1}]$ and $[011]$ using reciprocal space maps at 0° and 90° azimuths for (422) and (42 $\bar{2}$) reflections. Anisotropic relaxation process causes a large difference in FWHM of (400) diffraction peaks of Omega scans along the $[01\bar{1}]$ and $[011]$ directions. Under such circumstances, a simple comparison of the FWHM of diffraction peaks might be inappropriate unless

anisotropic distribution of relaxation process is taken into account. Subsequently, LCL, tilt, and twist values along the two orthogonal directions are estimated by applying the Williamson-Hall analysis. The ratio of tilt and twist values is ≈ 1.3 and ≈ 2.9 predominantly due to 60° perfect and 90° partial dislocations with the line of dislocation along the $[011]$ and $[01\bar{1}]$ directions, respectively. It is understood that 90° partial dislocations nucleate predominantly in the beginning of strain relaxation process. Such 90° partial dislocations glide towards the interface and therefore produce stacking faults in its wake, which is confirmed by the HRTEM image of the sample. Once the epilayer thickness becomes sufficiently large, it can lead to the substantial relaxation of layer where 60° perfect dislocations relieve the strain. Prevalence of 90° partial dislocations in our sample leads to the observed anisotropy of mosaicity and the dislocation distribution. The anisotropic distribution of microstructures is also revealed by the surface topography of GaP epilayer in AFM measurements. The origin of anisotropic distribution of dislocation is explained through the Burgers vector network and their consequences are seen in the cross sectional HRTEM images.

For zinc-blende tensile strained material combination, a method is proposed for estimating the density of 90° partial and 60° perfect dislocations where FWHM is replaced by tilt along with the magnitude of the respective component of Burgers vector in the conventional formula. The propose formula shall be applicable for any zinc-blende tensile strained material system. It is found that the Burgers vector of 90° partial dislocations (tilt component of 60° perfect dislocations) are responsible for tilt along $[011]$ ($[01\bar{1}]$) direction. The values of tilt are estimated using systematic Williamson-Hall analysis which are then put in the proposed formula for the estimation of density of 90° partial and 60° perfect dislocations. It is found that the density of 90° partial

dislocation is an order of magnitude large in comparison to 60° perfect dislocations. It is also noticed that the dislocation density is underestimated by the previously reported methods. HRXRD being a non-destructive tool is shown to be very effective in estimating the asymmetry of dislocation density rather quickly compared to HRTEM technique which is already known to be destructive, arduous and less statistical. The proposed method is considerably helpful to epitaxial growers who shall be able to optimize the crystalline quality of layers over a short period of time.

Chapter 4

Study of the Anisotropic Distribution of Microstructure in Compressively Strained InP/GaAs Epitaxial Layers

4.1 Introduction

InP is a material of choice for the development of light emitting devices operating in the wavelength range of 925 to 1660 nm, optoelectronic integrated circuits, high speed microwave and millimeter wave circuits, solar cells, and wireless applications owing to its direct bandgap covering the low loss telecommunication window (1550 nm) and very high electron mobility.^{182–185} Since InP wafers are costly, brittle and are available in small size, InP films grown on GaAs substrates have emerged as an alternate solution to the need of large area InP based devices.¹⁸³ Owing to large lattice mismatch (3.8%) and thermal expansion coefficients differences (19.7%) between InP and GaAs, the critical layer thickness of InP on GaAs substrate is less than 50 Å according to Matthews and Blakeslee model¹⁸⁶ and $\approx 17 \text{ Å}$ ¹⁴⁷ by X-ray interference effect method. A high value of dislocation density often exceeding 10^9 cm^{-2} have been recorded in InP layers grown on GaAs substrates.^{187,188} This poses a challenge to epitaxial growers and the grown film is found to be of mosaic nature. A quantitative analysis of the dislocation density is therefore of immense interest. InP layers on GaAs substrate are studied by HRTEM by a few researchers.^{183,188} However, no systematic study using HRXRD technique aiming to learn the asymmetric distribution of dislocations in InP/GaAs system is available in literature. In this chapter, anisotropic distribution of microstructure is studied in compressively strained InP/GaAs epitaxial layers by HRXRD technique. It is noticed that the crystalline quality of layer is better

along [011] direction when compared with [01 1] direction. It is also found that the dislocations are mainly 60° perfect dislocations along both the in-plane orthogonal directions. The density of 60° dislocations is also estimated from the analysis of HRXRD data. Polarization dependent photoluminescence (PL) measurements are also performed in order to access the anisotropy in the optical quality of layer.

4.2 Experimental details

InP layer of 2-micron thickness is deposited using metal organic vapour phase epitaxy reactor (AIX-200) on GaAs substrate at 50 mbar pressure. GaAs substrates are $\approx 400\ \mu\text{m}$ thick and are oriented along [100] with a nominal miscut of 0.05° along [01 1] direction. InP layer is grown at 660°C using phosphine and trimethylindium (TMIn) source materials. PANalytical X'PERT diffractometer equipped with $\text{CuK}\alpha_1$ X-rays (wavelength = $1.54056\ \text{\AA}$) and a hybrid $4\times$ monochromator (beam divergence ≈ 20 arc sec) is used to perform HRXRD measurements. X-ray beam has a footprint of $\approx 15\ \text{mm} \times 2\ \text{mm}$ on the sample surface perpendicular to the diffraction plane. Xenon gas filled proportional counter is used to record the intensity of diffracted beam where various $\omega/2\theta$ and ω open detector scans are performed by setting the opening of detector equal to 1° . For Williamson-Hall analysis, ω scans are recorded in triple axis geometry by inserting a triple bounce Ge (220) analyser crystal (acceptance angle ≈ 12 arc sec) in front of the detector. In this chapter, ω , θ , and 2θ are defined as the angles which incident X-ray beam makes with the sample surface, reflecting plane and diffracted X-ray respectively. On the other hand, ϕ is the azimuthal angle which lies between the projection of the incident X-ray beam on sample surface and sample in-plane [01 1] direction whereas ψ is the angle between the growth direction i.e. [100] and surface normal of the corresponding diffraction plane. Instrumental broadening

effects have been neglected in data analysis because the values of full width at half maximum (FWHM), also defined by symbol β , of HRXRD patterns is about five times larger than the instrumental broadening.¹⁴⁶ Wafer bowing¹⁶⁶ is another important factor in particular for the samples where a large difference in the values of thermal expansion coefficients of substrate and layer exists. However, this is also neglected in present case since 1) the layer is of mosaic nature and 2) the thermal expansion coefficient difference is only $\approx 19.7\%$ which is low in comparison to the value corresponding to GaAs layers grown on Silicon substrates.

Reciprocal space maps (RSM) on {422} asymmetric planes are recorded in triple axis geometry at 0° and 90° azimuths by keeping [011] and [01 $\bar{1}$] directions perpendicular to the diffraction plane respectively. Williamson-Hall (WH) analysis is performed by considering (200), (400), (600) symmetric planes and also various skew-symmetric planes like (133), (422), (511), (311) which are inclined at an angle (ψ) with respect to the growth direction.^{2,189} PL is excited with a second harmonic of Nd:YAG laser beam ($\lambda = 532$ nm) focused on a ≈ 100 μm diameter spot, where the sample was mounted inside a closed cycle He cryostat for low temperature measurements. An optical polariser was kept in the path of incident laser along with a neutral density filter. Two PL measurements are recorded by keeping the direction of electric vector of laser fixed and aligning the sample direction [011] (azimuth 0°) and [01 $\bar{1}$] (azimuth 90°) by rotating the sample accordingly. AFM measurements are performed in non-contact mode using a multimode scanning probe microscope (NT-MDT, SOLVER-PRO, Russia) equipped with Silicon cantilever tips having a radius of curvature of ≈ 10 nm, resonant frequency ≥ 190 kHz and spring constant ≈ 5.5 N/m.

4.3 Results and discussion

Figure 4.1 shows HRXRD pattern for (400) reflection recorded at 0° and 90° azimuths. At $0^\circ/180^\circ$ azimuth the direction perpendicular to diffraction plane is along $[011]/[0\bar{1}1]$. Similarly at $90^\circ/270^\circ$ azimuth the corresponding direction is along $[01\bar{1}]/[011]$. Clear peaks corresponding to GaAs substrate and InP layer are observed at both the azimuths with nearly same layer-peak separation ($\approx 1.41^\circ$). However, FWHM of layer peaks at 0° azimuth is slightly lower along $[011]$ direction, as obvious from **Figure 4.1**, which indicates about the presence of large number of defects along $[01\bar{1}]$ in comparison to $[011]$ direction. It also indicates about the existence of an anisotropy in the microstructures between the two in-plane orthogonal directions. To understand this behaviour in more detail, several rocking curves are recorded for (400) reflections by the varying the value of azimuth from 0 to 360° with an intervals of 15° where the results are summarized in **Figure 4.2**. It is observed that the value of FWHM is larger

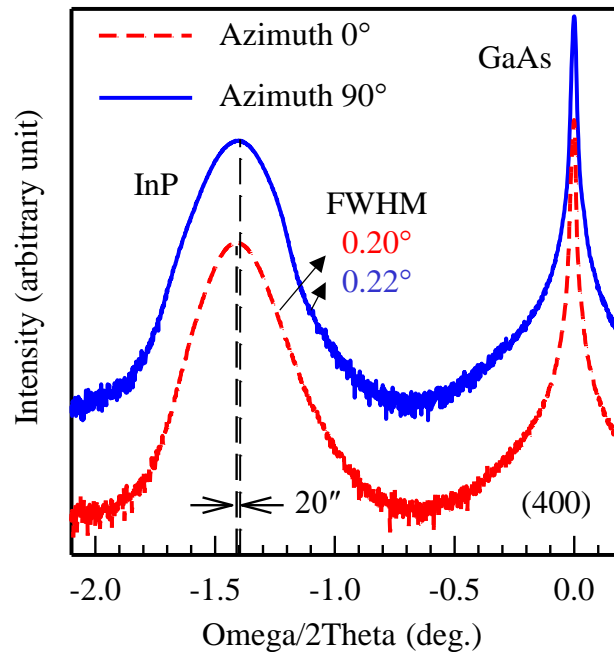


Figure 4.1 HRXRD pattern of InP epitaxial layer grown on GaAs substrates for (400) reflection recorded at two azimuths.

along $[01\bar{1}]/[011]$ direction in comparison to $[011]/[011]$ direction. One can therefore infer that the density of defects/dislocation is large along $[01\bar{1}]$ direction in comparison to other in-plane orthogonal direction. Note that in tensile strained GaP epilayers grown on GaAs substrates, an opposite behaviour was seen by us where the density of defects/dislocations was found to be large along $[011]$ direction.^{2,189}

In order to get further insights of the dislocation network in compressively strained InP/GaAs layer, reciprocal space map (RSM) corresponding to asymmetric

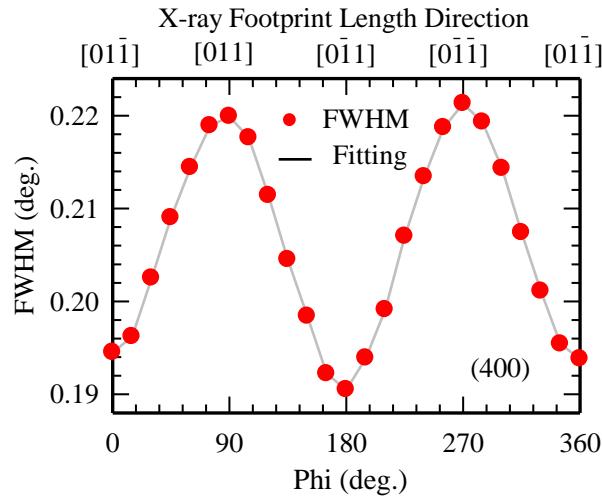


Figure 4.2 FWHM of (400) rocking curve plotted as a function of azimuth where solid line is a guide to the reader's eye.

$\{422\}$ reflections are recorded at 0° and 90° azimuths as shown in **Figure 4.3**. The relaxation² values calculated from the RSM are nearly same ($\approx 97\%$) and the variation of counts shown in **Figure 4.3** is also quite similar. Therefore, no direct information related to an asymmetry in the distribution of dislocations is available from RSM scans. Unfortunately, a separate estimate of size and strain broadening from RSM scans is not feasible. Nearly same relaxation along the two in-plane orthogonal directions is also observed by Weng et al.⁶⁹ for InSb/GaAs compressively strained epilayers. However, a

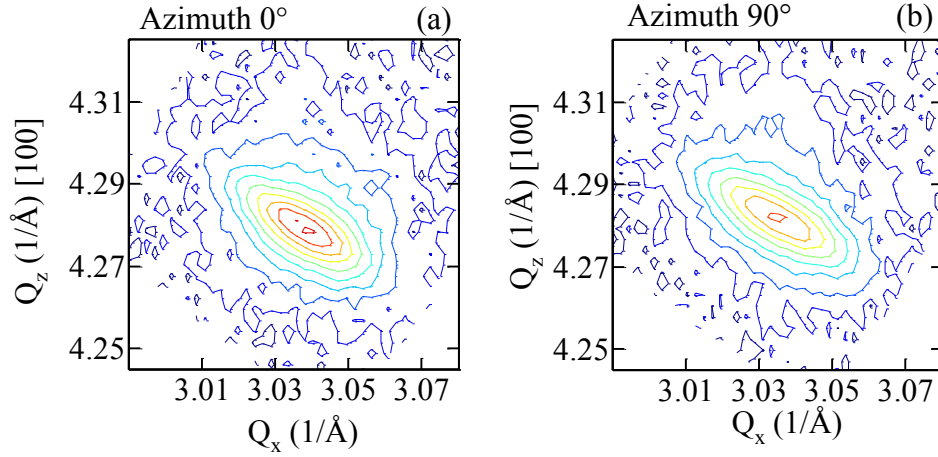


Figure 4.3 Reciprocal space maps of InP/GaAs layer recorded at 0° and 90° azimuths for {422} reflection.

reliable estimation of strain broadening is essential for studying the asymmetric distribution of dislocations in epitaxial layers.

To observe the effect of anisotropic distribution of defects in microstructure, we performed WH analysis at 0° and 90° azimuths along [011] and [01 $\bar{1}$] directions where the results are shown in **Figure 4.4(a & b)**. The values of LCL, tilt and twist for the layer are given in **Table 4.1**. The values of LCL are also slightly different along [011] and [01 $\bar{1}$] directions as shown in **Table 4.1**. It indicates that the crystalline quality of InP layer is better along [011] direction. Furthermore, the tilt is less along [011] direction when compared with [01 $\bar{1}$] direction. It also indicates that the crystalline quality is better along [011] direction.

Note that the values of twist along the two orthogonal directions are slightly different, however, the $\frac{\text{Tilt}}{\text{Twist}}$ ratio is nearly same (≈ 1.4) along the two directions as clearly shown in **Table 4.1**. Although there is some asymmetry in the density of dislocation in InP epilayer but nature of dislocations remains the same.^{2,189} It is also

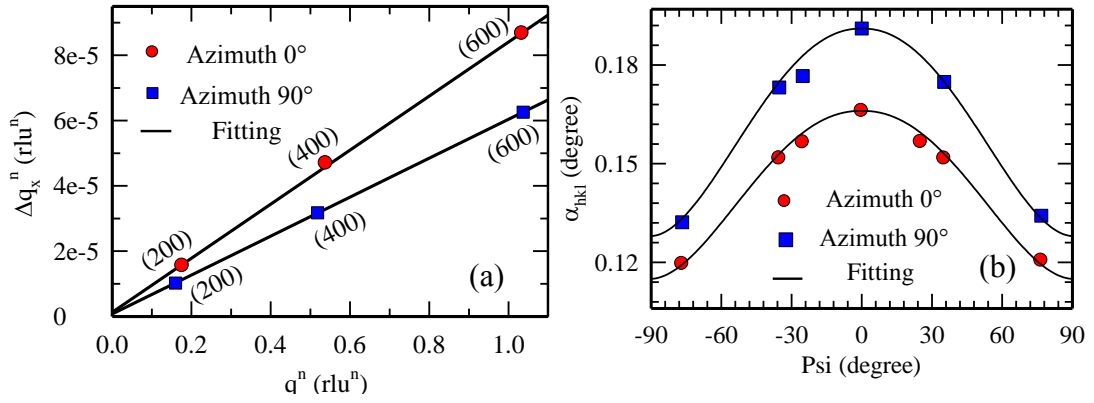


Figure 4.4 Williamson-Hall analysis: **a)** The width (Δq_x) obtained from pseudo-Voigt fitting of the omega scan diffraction peaks, n is related to Lorentzian fraction in the pseudo-Voigt fitting, is plotted as a function of q^n , **b)** The value of α_{hkl} are plotted as a function of ψ for 0 and 90° azimuths.

understood that the dislocations in compressively strained InP epilayers grown on GaAs are mainly 60° perfect dislocations along both the directions since $\frac{\text{Tilt}}{\text{Twist}}$ ratio remains ≈ 1.4 .^{2,189} This is contrary to our earlier observations made in case of tensile strained GaP/GaAs epitaxial layers where even the type of dislocations was found to be different along the two in-plane orthogonal directions.

Table 4.1 The values of microstructure namely lateral coherence length, tilt, twist and their ratio obtained from Williamson-Hall analysis at two orthogonal azimuths along with the values of dislocation density in InP epitaxial layer grown on GaAs substrate.

Azimuth	Direction ⊥ to diffraction plane	Line of dislocation	WH analysis				Dislocation density (60°)(cm ⁻²)
			LCL (μm)	Tilt and Twist			
				Tilt (°)	Twist (°)	Ratio	
0°	[011]	[01 1]-β	0.5±0.01	0.17	0.12	1.4	2.2×10 ⁹
90°	[01 1]	[011]-α	0.4±0.01	0.19	0.13	1.5	2.9×10 ⁹

Further, relatively large values of tilt and twist for line of dislocation along [011] (α) in comparison to those [01 $\bar{1}$] (β) indicates that the density of 60° (α) dislocations is large in our sample. It can also be understood that the density of dislocations is more on (111)/(11 $\bar{1}$) glide planes in comparison to (111)/(111) glide planes.¹⁸⁹ We recently proposed a formula for estimating the density of dislocations in zinc-blende epitaxial layers.¹⁸⁹ The values of dislocation density measured for the two in-plane orthogonal direction are shown in **Table 4.1**. The dislocation density is very high ($>10^9 \text{ cm}^{-2}$) where the measured values are found to be in agreement with those reported by other researchers.^{183,187,188} It is obvious that there is a slight difference in the value of dislocation density when measured along the two directions which is caused by the difference in the glide velocity of dislocations along the respective crystallographic directions.^{2,46,189} It is already known that the glide velocity of α dislocations is large in comparison to β dislocations.^{46,47,190,191} Kvam and Hull¹⁹² has also observed that only full lattice dislocations i.e. 60° perfect dislocations are responsible for relieving the strain in case of compressively strained layers. It is already known that that during the initial phase of growth α dislocations relieve the strain, however, β dislocations dominates the relaxation process beyond a certain thickness of layer.^{2,46,47,189} Owing to this reason, one should see a large anisotropy in the density of dislocations if the thickness of layer is kept reasonably low.^{2,46,47,189} A large value of layer thickness is the main reason why we see only a minor difference in the values of dislocation density. However, the anisotropy is clearly evident from the sinusoidal variation of FWHM of rocking curve as a function of azimuth as shown in **Figure 4.2**.

It is interesting to see the impact of anisotropic distribution of dislocations on the surface morphology. In earlier chapter,² elongation of grains along a particular

direction was reported by us for tensile strained GaP layers grown on GaAs. However, no major difference in the topography of InP layers between the two in-plane orthogonal directions is seen as obvious from the AFM image shown in **Figure 4.5**. One plausible explanation for this observation can be given in terms of the difference in initial relaxation of layer in the two cases. In a compressive (tensile) strained layer, initial relaxation is governed by 60° perfect (90° partial) dislocations. During the glide process towards the interface, partial dislocations produce stacking faults in their wake.^{2,63} Partial dislocations are responsible for crack formation in layer along the line of dislocation.¹⁹³ Cracks have been observed in surface morphology of several tensile strained layers.^{2,61,193–195} However, no such behaviour is observed in case of 60° perfect dislocations. Therefore cracks are not observed in the AFM image shown in **Figure 4.5**. Thus AFM image alone can give a hint about the presence of dominant dislocations in a zinc-blende system where presence of crack itself can confirm about the presence of 90° partial dislocations.

Low temperature PL measurements are also performed to compliment the information obtained from HRXRD on the asymmetry in crystalline quality of layer.

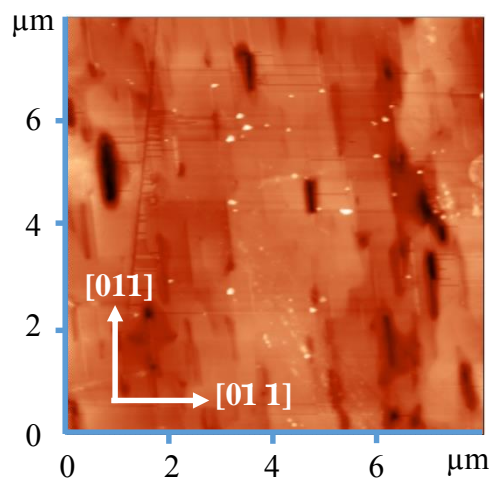


Figure 4.5 Atomic force microscopy image of InP epitaxial layer grown on GaAs substrates.

For this purpose, polarization dependent PL measurements are performed by inserting a polarizer in the path of incident laser beam before it falls on the sample. The polarizer axis is made nearly parallel to $[01\bar{1}]$ and $[0\bar{1}1]$ directions by rotating the sample in order to collect the PL data shown in **Figure 4.6**. Four distinct peaks are observed in the PL spectra at 1.42, 1.38, 1.34 and 1.32 eV which are labelled as A, B, C and D respectively. Here, the most intense PL feature (peak A) is labelled as band-to-band recombination¹⁹⁶ which is commonly observed in case of n-type InP.^{197,198} Other peaks seen in the PL spectra are also commonly observed in InP which are generally labelled as either defect associated features or phonon replica of band-to-band recombination feature of InP.^{196,197,197,199,200} An important outcome of PL measurements is that the intensity of PL signal is more along $[01\bar{1}]$ direction when compared with $[0\bar{1}1]$ direction. It can be therefore inferred that the optical quality of layer is poor along $[0\bar{1}1]$ direction in comparison to $[01\bar{1}]$ direction. It means that the density of defects/dislocations is relatively large along $[0\bar{1}1]$ direction.^{201,202} It also shows that the conclusions drawn from the PL measurements on the asymmetry in optical quality of

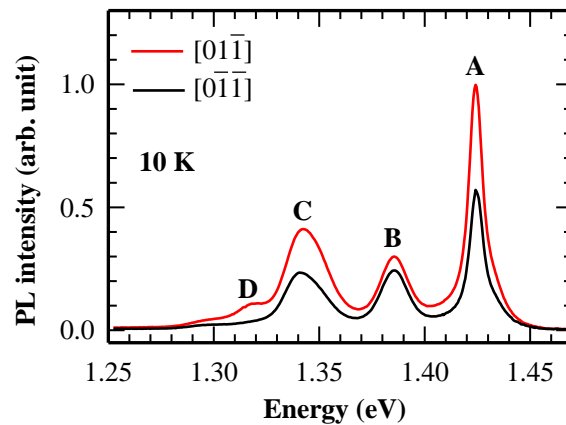


Figure 4.6 10 K Polarization dependent PL spectra of InP epitaxial layer grown on GaAs substrates.

layer are in good agreement with the observations made on the asymmetry in crystalline quality from HRXRD measurements.

4.4 Conclusion

Anisotropic distribution of defects/dislocations is studied by using HRXRD technique for compressively strained InP epitaxial layer grown on GaAs substrates. Only a minor difference in the microstructure parameters is observed, however, the anisotropy is clearly observed by recording a set of rocking curves by varying the azimuth. The value of FWHM of diffraction pattern, which is governed by the crystalline quality of layers, shows a sinusoidal variation with azimuth indicating about the presence of an anisotropy in layer. Further, it is observed that the value of dislocation density is slightly large along $[01\ 1]$ direction when compared with $[011]$ direction. The reason of anisotropy is attributed to the difference in the glide velocity of dislocations which is higher for the dislocations having line of dislocation along $[011]$ in comparison to $[01\ 1]$ direction. The information received from HRXRD measurements related to the presence of asymmetry in crystalline quality of layer is complemented by polarization dependent PL measurements. It is also proposed that the presence of cracks in topography of sample indicates about the incorporation of tensile strain which is not expected in case of compressively strained zinc-blende epitaxial layers.

Chapter 5

Study of the Anisotropic Distribution of Microstructure in Compressively Strained GaAs/Si Epitaxial Layers: A Case of Polar on Nonpolar Material Combination

5.1 Introduction

In this chapter, results related to the anisotropic distribution of microstructure in compressively strained GaAs/Si epitaxial layers are presented. The combination of well-developed Si technology with group III/V semiconductors like GaAs, GaP and InP opens up the possibility for a wide range of optoelectronic devices; for example, integrated light emitting diodes, laser diodes, detectors and solar cells on Si substrates.^{1,119} However, epitaxial growth of GaAs on Silicon substrates poses a formidable challenge due to the high lattice constant mismatch, large thermal expansion coefficients difference and presence of anti-phase domains.^{1,5,45,203} The lattice constant mismatch and difference in the thermal expansion coefficients between GaAs and Si are 4.1% and $3.43 \times 10^{-6} \text{ K}^{-1}$, respectively.⁴⁵ As mentioned earlier, this material combination is prone to a high density of dislocations leading to the mosaicity of epilayers. HRXRD characterization of compressively strained GaAs/Si epitaxial layers is therefore of considerable important where microstructural information related to the lateral coherence length (LCL), vertical coherence length (VCL), tilt, twist, and microstrain can be estimated using Williamson-Hall analysis. In Williamson-Hall analysis, HRXRD data for a set of symmetric reflections such as (L00) and (00L) planes (where L = 2, 4, 6) for zinc-blende and wurtzite systems respectively is recorded.^{49,117}

However, in a few cases especially for zinc-blende structures Williamson-Hall (WH) analysis gives unrealistic information due to the following reasons;

i) For the epitaxial layers grown on (100) nominally oriented cubic substrates, the predominantly allowed reflections are (200), (400) and (600) which is primarily decided by the wavelength of $\text{CuK}\alpha_1$ X-ray beam in our HRXRD setup as shown in **Figure 5.1**.⁴⁹ Further higher order symmetric reflections, for example (800), are not accessible using $\text{CuK}\alpha_1$ beam as can be understood from **Figure 5.1**. It is therefore obvious that the measured values of $\Delta q_{(L00)VCL}$ and microstrain obtained from WH analysis will be highly inappropriate in case any of the three allowed reflections is adversely effected by a poor signal to noise ratio.

ii) Sometimes one of the allowed reflections, for example (600) in case of GaAs, is very weak due to minimal contrast in the form factors ($f_{III/V}$) of the constituent atoms. The structure factor (s) for (hkl) plane of zinc-blende structure when h, k, l are unmixed (i.e. all even or all odd) is given by $s \propto (f_{III} + f_V e^{-i\frac{\pi}{2}(h+k+l)})$, where f_{III} and f_V are the form factors of the group III and V atoms respectively. In case of GaAs, the values of form factor of Gallium and Arsenic atoms are very close and the contrast further reduces at large diffraction angles.^{14,81} Due to these reasons the value of structure factor for (600) reflection, which is proportional to $(f_{Ga} - f_{As})$ where f_{Ga} and f_{As} are the form factors of Gallium and Arsenic atoms, is going to be very small. Therefore, (600) is a weak reflection in GaAs which leads to poor signal to noise ratio for one of three symmetric reflections. Hence, WH analysis will provide unrealistic information of the microstructure in case (600) reflections of GaAs is included.

iii) Finally, anti-phase domains (APD) are generated whenever zinc-blende epilayers

are grown on non-polar substrates like Si or Ge. Presence of the APD results in selective broadening of some reflections such as (200) and (600) because the structure factor for these reflections depends upon the relative positions of Ga and As atoms.¹ Influence of APD in the selective broadening of a few reflections has also been seen in several other material systems including metallic alloys.^{1,119}

Due to the abovementioned reasons, WH analysis cannot be used for evaluating the values of VCL, microstrain, LCL and tilt of zinc-blende epilayers grown on Si using a set of symmetric reflections i.e. (L00) where $L = 2, 4, 6$. HRXRD measurements which are generally performed using laboratory X-ray sources based on Copper/ Molybdenum X-ray tubes are largely unattractive for studying GaAs/Si epitaxial layers via WH analysis. Under such cases, a modified Williamson-Hall analysis is often adopted where a new set of parallel skew-symmetric crystallographic planes are taken and the same is also discussed in a later half of this chapter.^{4,5} However, the acquisition of HRXRD data for skew-symmetric reflections is rather cumbersome. Precise multidirectional alignment of a sample is critical for the data acquisition of a diffraction pattern for skew-symmetric crystallographic planes. A goniometer with precise multidirectional movements is therefore essential for recording the data required for the extended WH analysis. Moreover, one probes the epilayer along a different crystallographic orientation under the modified WH method. On the other hand, large photon counts are usually recorded for symmetric reflections and even the data acquisition is relatively simpler. In view of this, it is desirable to find a set of reflections where diffraction patterns of reasonable intensity can be recorded. In this context, synchrotron radiation sources offer a great opportunity for the HRXRD measurements where a broad range of intensity and wavelength of X-ray radiation can be obtained. This indeed becomes

extremely important for the cases where a few crucial reflections are either broadened due to structure factor considerations or are inherently weak for a particular crystallographic plane as mentioned above. This is indeed possible at a synchrotron radiation source where the size of the limiting sphere can be varied by changing the wavelength of the X-rays as shown in **Figure 5.1**. Moreover, the intensity of the incident X-ray beam at a synchrotron radiation source is very high⁹ when compared with the laboratory-based sources. With this in mind, we present the WH analysis of GaAs epilayers grown on Si by performing HRXRD measurements on the Indus-2 synchrotron radiation source. It is found that the conventional WH analysis performed on a synchrotron radiation source is able to reveal the desired information related to the microstructure of GaAs epilayers grown on Si which is in reasonable agreement with the results obtained from atomic force microscope (AFM) measurements.

5.2 Experimental details

GaAs epilayers were grown by the two-step growth method in a horizontal metal organic vapour phase epitaxy reactor (AIX-200) system. Trimethylgallium (TMGa) and arsine gas were used as precursors. Prior to growth, Si substrates were cleaned using a modified Radio Corporation of America (RCA) cleaning method.¹¹⁹ Afterwards the substrate was preheated to 870°C for 30 min in a hydrogen (H₂) flow of ≈ 8 slpm (slpm = standard litres per minute). This is desired for promoting Si surface rearrangement and also for the removal of native oxide from Si substrate. This procedure for the removal of native oxide from Si wafers is found to be very successful where it is reported that the native oxide on Si wafer would not reappear even after 1–2 h.²⁰⁴ After pre-heating the Si wafer at 870°C in the presence of H₂ for 30 min, the temperature was reduced to 450°C in the presence of a high flow of arsine. At this temperature, a GaAs

nucleating layer of thickness ≈ 60 nm with a V/III ratio ≈ 340 was grown. This was followed by the growth of a GaAs layer of thickness ≈ 250 nm at 670°C with V/III ratio ≈ 100 . This sample is labelled as S1. Three more samples are studied in this chapter where growth details are summarized in **Table 5.1**.

The synchrotron-based HRXRD measurements were performed using the angle-dispersive X-ray diffraction beamline (BL-12)⁹ at the Indus-2 synchrotron radiation source of RRCAT, Indore. The beamline consists of a Si (311) based double-crystal monochromator with bendable focusing optics. HRXRD measurements at Indus-2 are performed at 15.5 keV using a scintillator detector having 75 arc sec opening in the diffraction plane. The laboratory-source-based HRXRD measurements were performed using the PANalytical X'pert PRO MRD system. Note that the FWHM of HRXRD patterns is typically one order larger than the instrumental broadening. Hence, it is neglected in the data analysis.¹⁴⁶ Two independent sets of X-ray diffraction patterns are recorded using the respective laboratory and synchrotron sources. ω and $\omega/2\theta$ scans for the (L00) reflections ($L = 2, 4, 6$ etc.) of GaAs were performed using the synchrotron radiation and laboratory sources, respectively. Here, ω is defined as the angle between the incident X-ray beam and the sample surface while 2θ is the angle between the incident and diffracted X-ray beams. The ω and $\omega/2\theta$ directions explore the Ewald sphere in different directions as shown in **Figure 5.1**, where ω ($\omega/2\theta$) scan provides the lateral (vertical) information of the epilayer. AFM measurements are performed using a multimode scanning probe microscope (NT-MDT, SOLVER-PRO). Silicon cantilever tips of radius of curvature 10 nm, resonant frequency 190 kHz and spring constant 5.5 Nm^{-1} are used in non-contact mode. The thickness of epilayers was determined by a surface profilometer model Alpha-step IQ (KLA Tencor make). Steps on GaAs/Si

samples were made by the selective etching of GaAs using $\text{CH}_3\text{OH}:\text{H}_3\text{PO}_4:\text{H}_2\text{O}_2$ (3:1:1) isotropic etch solution.²⁰³ The cross sectional HRTEM micrographs are recorded using Philips CM200 at an accelerated voltage of 200 kV. Cross-sectional samples are prepared by the conventional procedures involving mechanical thinning followed by Ar-ion milling.

Table 5.1 Summary of various growth parameters of the GaAs / Si samples.

Sample No.	Layer detail	Growth Temp. (°C)	Thickness (nm)	V/III ratio
S1	GaAs Nucleating layer	450	60	340
	GaAs thick layer	670	250	100
S2	GaAs Nucleating layer	450	60	337
	GaAs thick layer	650	250	103
S3	GaAs Nucleating layer	450	60	518
	GaAs thick layer	670	250	103
S4	GaAs Nucleating layer	400	60	337
	GaAs thick layer	670	250	103

5.3 Results and discussion

5.3.1 HRXRD results based on the synchrotron radiation source

The crystallographic planes that can be accessed in HRXRD measurements are determined by the wavelength (λ) of the X-ray radiation source. This is described by drawing a limiting sphere of ' $2/\lambda$ ' radius as shown in **Figure 5.1**. The limiting sphere for the laboratory XRD systems based on $\text{Cu K}\alpha_1$ ($\lambda = 1.54056 \text{ \AA}$) is shown in **Figure 5.1** where one can access only the (200), (400) and (600) set of symmetric planes. Note that there are many asymmetric reflections that are also accessible by the same X-ray source. However, we are interested only in the symmetric reflections for the conventional WH analysis. The radius ($2/\lambda$) of the limiting sphere can be enlarged by

increasing the energy of the incident X-ray beam at the synchrotron radiation source as shown in **Figure 5.1**. It is obvious that now even the (800) symmetric reflection can be accessed that can be used to improve the accuracy of conventional WH analysis. Furthermore, the enormous intensity of the X-ray beam at a synchrotron radiation source considerably helps to improve the signal-to-noise (S/N) ratio.

Figure 5.2 shows ω and $\omega/2\theta$ scans recorded for various symmetric reflections

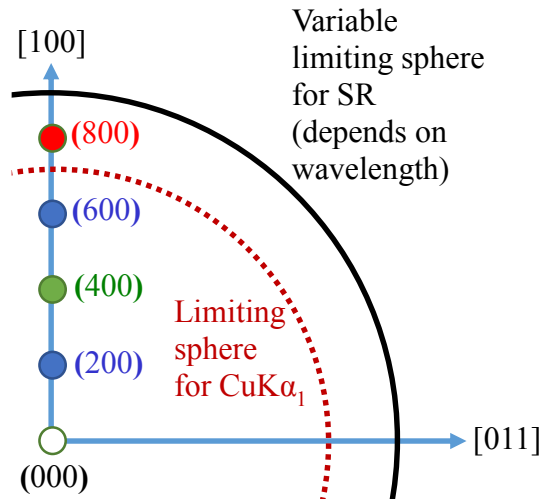


Figure 5.1 Schematic of the portion of the limiting sphere to illustrate the allowed symmetric reflections for GaAs grown on (100) Si substrates. Here, the [011] direction lies in the growth plane. The limiting sphere governed by the wavelength of the laboratory X-ray source ($\text{Cu K}\alpha_1$) is shown by a dashed line (red) whereas the limiting sphere governed by the wavelength of synchrotron radiation is shown by a solid line (black). Note that the (800) reflection (red filled circle) is accessible only when HRXRD measurements are performed at the synchrotron radiation source. At 15.5 keV energy a few more reflections are accessible. However, the reflections only up to (800) are shown here for simplicity.

using the laboratory- and synchrotron-based X-ray sources for sample S1. Note that the FWHM of the respective diffraction patterns that are recorded at two separate HRXRD systems are almost similar. This is obvious since the plots are made while keeping the x-axis in reciprocal lattice units instead of ω and $\omega/2\theta$.

Furthermore, the diffraction pattern for the (600) reflection recorded by the laboratory source is very weak and cannot be used in WH analysis. On the other hand, the same pattern recorded by the synchrotron radiation source has a very good S/N ratio that makes it reasonable for WH analysis. As mentioned earlier, the wavelength of a synchrotron radiation source is tunable which in fact enabled us also to record the diffraction pattern for the (800) reflection. Such a diffraction pattern cannot be recorded by using a laboratory source equipped with Cu X-ray tube. This reflection can also be

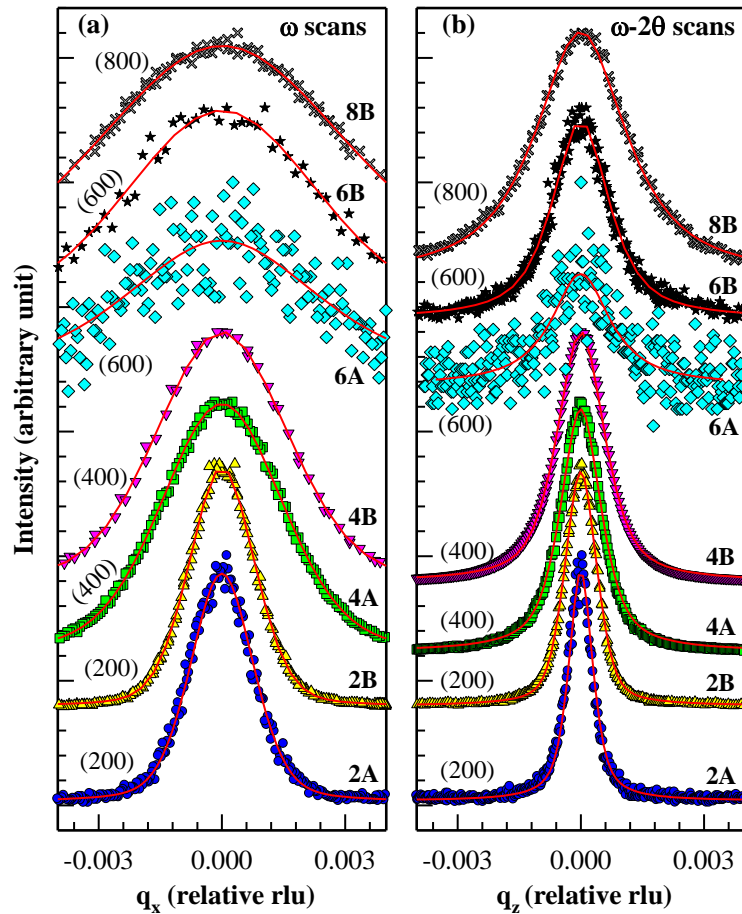


Figure 5.2 HRXRD pattern of GaAs epilayer grown on Si substrate (Sample S1): (a) ω scans, (b) $\omega/2\theta$ scans, where the curves labelled as 2A (2B), 4A (4B) and 6A (6B) are the diffraction patterns for the (200), (400), (600) reflections acquired using the laboratory (synchrotron) based X-ray source. Note that the (800) scans are acquired only at the synchrotron radiation source. The overlaying solid lines show the pseudo-Voigt fitting of the experimental data.

probed by a Molybdenum-based X-ray source. However, a Cu $K\alpha_1$ X-ray source is generally preferred for investigating the conventional III/V semiconductors because Cu $K\alpha_1$ interacts with matter more strongly than Mo $K\alpha_1$, leading to brighter diffraction spots. It can be easily appreciated that the availability of HRXRD data for four symmetric reflections is extremely important for the accuracy of microstructure information obtained from conventional WH analysis.

Next, the data shown in **Figure 5.2** are analyzed by following the procedure of WH analysis. It is observed that a low (high) value of ‘f’ is recorded for the ω ($\omega/2\theta$) scans. A low (high) value of ‘f’ along the ω ($\omega/2\theta$) direction indicates that the Lorentzian component of the broadening is low (high) along the lateral (vertical) directions. Note that the Lorentzian component of the broadening is governed by the theoretical broadening of the crystal while the Gaussian component of the broadening is decided by the crystal imperfections and inhomogeneities. Hence, a large value of ‘f’ extracted from $\omega/2\theta$ scans indicates a large grain size along the vertical direction while a low value of ‘f’ extracted from the ω scans shows a small grain size in the lateral direction. This indicates the presence of a large number of defects and dislocations in the lateral direction. In the case of the GaAs/Si (100) material system, the majority of dislocations are of 60° mixed dislocations.^{4,14,152} Burgers vectors of 60° mixed dislocations have three major components, namely misfit, screw and tilt.^{4,14,152} While the tilt components of the dislocations lie primarily along the [100] direction, the misfit and screw dislocation components lie along the $\langle 110 \rangle$ directions. Because of this, one expects to observe a large number of dislocations in the growth plane which is the primary reason for the large broadening of the ω scans and also the low value of ‘f’.

Figure 5.3 shows the WH plots for ω and $\omega/2\theta$ scans recorded using the synchrotron radiation source. The FWHM values estimated from the line-shape analysis of the data shown in **Figure 5.2** are plotted in **Figure 5.3** where q_x (q_z) represents the FWHM of the ω ($\omega/2\theta$) scans for the corresponding symmetric reflections. The intercept on the y-axis is related to the value of LCL (VCL) which is obtained from the plot of q_x^n (q_z^n) versus q^n . Similarly, the slopes of the two curves provide the values of tilt and micro-strain, respectively. These values are summarized in **Table 5.2**.

Figure 5.4(a) shows the AFM image of the same sample. The formation of grains of different sizes and the grain boundaries are clearly observed in the AFM

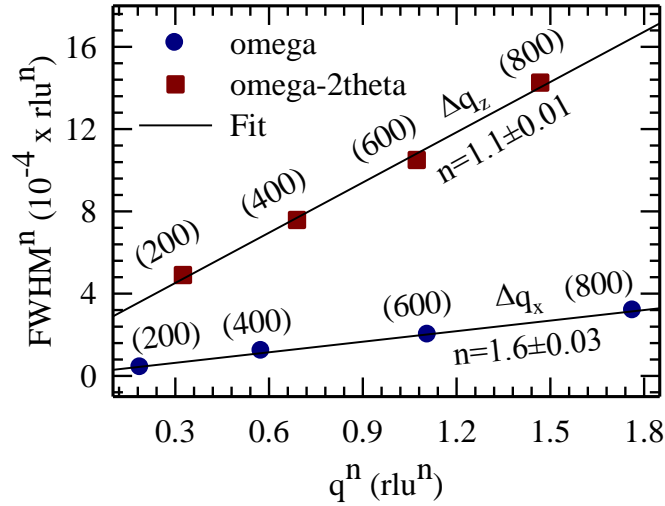


Figure 5.3 Williamson–Hall plots prepared using ω and $\omega/2\theta$ scans for (200), (400), (600) and (800) symmetric reflections recorded using the Indus-2 synchrotron radiation source. The size of the error bars is smaller than the size of symbols. The value of n is 1 for the Lorentzian component and 2 for the Gaussian component; $1 < n < 2$ whenever the line shape is defined by a pseudo-Voigt profile.

image. The observed mosaic nature of the sample is expected because of the large lattice constant and thermal constant mismatches between the layer and substrate. **Figure 5.4(b)** shows the variation of the size of grains versus frequency (number of grains of the same size) of the sample which is obtained for the image analysis of AFM data. A

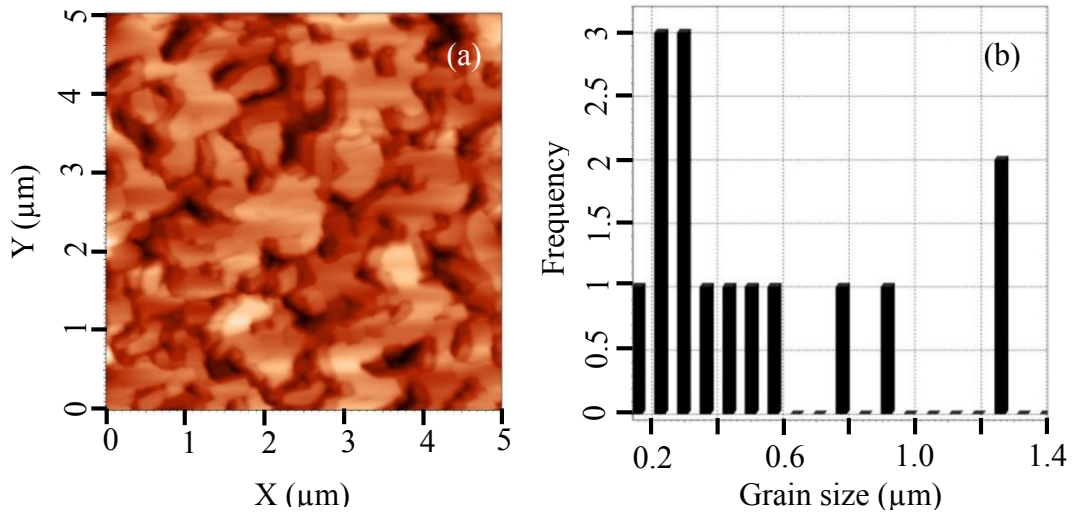


Figure 5.4 (a) AFM image ($5\ \mu\text{m} \times 5\ \mu\text{m}$) of the GaAs epilayer grown on Si substrate, and (b) frequency distribution of the grain size obtained from the image analysis of AFM data.

large majority of grains are of size smaller than $0.6\ \mu\text{m}$ whereas only a few grains of size larger than $1\ \mu\text{m}$ are seen. The value of LCL estimated from WH analysis is lower than the grain size obtained from AFM measurements, which can be easily understood since the value of LCL is related to the grain size where atoms coherently scatter X-rays. Moreover, AFM provides microscopic information related to the topography of the sample whereas HRXRD delivers crucial information related to the crystalline quality. Similar trends are also reported by other researchers.^{119,205,206} Furthermore, the thickness of the GaAs layer measured from the surface profiler is about $0.31\ \mu\text{m}$. The value of VCL measured from WH analysis is lower than the layer thickness which is also expected because of the formation of defects and dislocations at the GaAs–Si heterointerface. Note that the value of VCL is correlated with the part of the layer thickness where atoms coherently scatter the X-ray radiation. A small VCL clearly indicates a poor quality of heterointerface, which is expected due to the large lattice mismatch between the layer and substrate. Note that the intensity of the synchrotron

radiation source in our experiments was about $25 \mu\text{Wmm}^{-2}$. GaAs is a radiation-hard material²⁰⁷ which makes it a potential candidate for the development of detectors for high-flux X-ray imaging applications.^{208,209} No structural change in the sample was observed after exposure to the synchrotron radiation. AFM images were also recorded before and after the exposure where no change in the sample topography was observed.

Table 5.2 Summary of the microstructure of GaAs epilayers grown on Si substrate. The values of lateral coherence length (LCL), vertical coherence length (VCL), tilt and micro-strain are obtained by performing the Williamson–Hall analysis of HRXRD data acquired at the Indus-2 synchrotron radiation source. The values of grain size and layer thickness measured by atomic force microscopy and surface profiler techniques are also included for comparison purposes.

Epilayer thickness(μm)	Grain size (μm)	LCL WH (μm)	VCL WH (μm)	Tilt WH ($^{\circ}$)	Micro-strain WH (%)
0.31	0.40 ± 0.05	0.11 ± 0.005	0.24 ± 0.08	0.27 ± 0.01	0.15 ± 0.1

5.3.2 Modified Williamson-Hall analysis for studying the microstructure in compressively strained GaAs/Si epitaxial layers

Although the application of synchrotron radiation source in performing Williamson-Hall analysis on GaAs/Si epitaxial layers is successfully proven in the previous section but it is not recommended for the routine characterization purpose. It might be a cumbersome process when several samples are to be investigated since availability of the beam time is often limited. Hence, alternate methodologies are required with an aim of accessing a similar information by recording a set of diffraction patterns with a laboratory based X-ray source alone. Under such circumstances, the

scheme of modified Williamson-Hall analysis can be implemented by choosing a set of parallel planes which are tilted at a fixed angle with respect to the sample surface.¹⁰ Here, (111), (333) and (444) skew-symmetric reflections are chosen for recording HRXRD data which is then used to measure the information related to the microstructure in GaAs/Si epitaxial layers without any ambiguity. Here, modified Williamson-Hall analysis¹⁰ is implemented by recording $\omega/2\theta$ scans for set of {111} parallel planes that are tilted at 54.73° with respect to the sample surface.¹⁰ **Figure 5.5(a,b)** shows the W-H plots using the ω and $\omega/2\theta$ scans for the GaAs/Si samples using (111), (333) and (444) reflections for three samples. As obvious from **Figure 5.5(a,b)**, the experimental data can be accurately fitted with a straight line for all the three samples (S2 to S4) confirming the usefulness of modified WH analysis for evaluating the micro- structures of zinc-blende epilayers.

Table 5.3 summaries the values of microstructure determined from modified Williamson-Hall analysis for all the three samples. The values of VCL obtained for

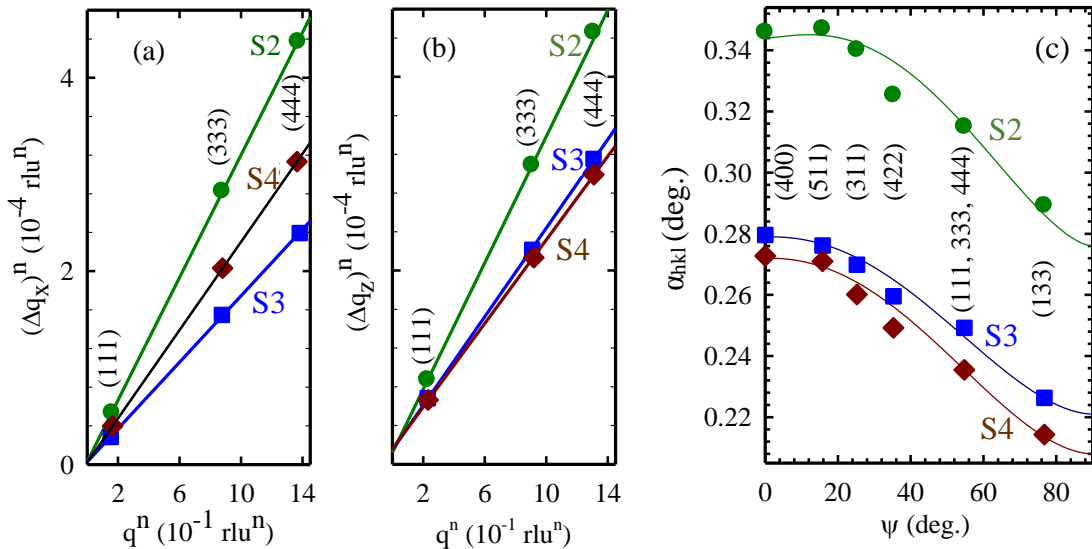


Figure 5.5 (a(b)) WH plots for GaAs/Si samples (S2, S3, and S4) using the ω ($\omega/2\theta$) scans for a set of skew-symmetric reflections. Straight lines show a linear fitting of the experimental data. (c) Variation of α_{hkl} for several skew-symmetric reflections.

these samples corroborate with the epilayer thickness measured by the surface profiler. The measured values of VCL are thus found to be equivalent to the layer thickness.^{206,210–212} Further, the value of microstrain is smaller for samples having larger VCL as expected. Furthermore, it is observed from **Table 5.1** and **Table 5.3** that one should choose a lower temperature for the growth of buffer layer since the values of microstrain / tilt / twist are lower and LCL is larger for sample S4 when compared with S2. On the other hand, high V/ III ratio should be preferred as can be understood by comparing the microstructures of samples S2 and S3 from **Table 5.3**. Scheme of modified WH analysis based on (111), (333) and (444) reflections is therefore highly useful for evaluating the microstructures of zinc-blende epilayers grown on non-polar substrates with a lab source based HRXRD setup.

It is generally known that there are two types of dislocations that are prevalent in the lattice mismatched III-V semiconductors: I) pure edge type dislocations with the line of dislocation along [011] and Burgers vector along [011], II) 60° mixed type of dislocations with the line of dislocation along [011] and Burgers vector along [101] direction.^{14,152} Type I dislocations help in relieving the misfit strain and do not contribute to any tilt or twist between the layer and substrate. Burgers vector of a type II dislocation (60° mixed dislocation) can be decomposed into three parts. For a dislocation line lying along [011] direction, Burgers vector can be decomposed into the following components as shown in **Figure 5.6(a)**: $\frac{1}{2} [110] (\mathbf{b}_{60^\circ}) = \frac{1}{4} [011] (\mathbf{b}_{\text{Misfit}}) + \frac{1}{4} [011] (\mathbf{b}_{\text{Twist}}) + \frac{1}{2} [100] (\mathbf{b}_{\text{Tilt}})$ respectively.^{14,152,213} The misfit component is responsible for relieving the strain in epilayer. This is identical to the effect of pure edge dislocations (type I dislocation). The screw (twist) component results in a local rotation of the mosaic

blocks about the direction resulting in twist between the mosaic blocks and the substrate and also between the individual mosaic blocks. The tilt component results in a tilt between the mosaic blocks and the substrate, and also between the mosaic blocks. It suggests that the tilt and twist in epilayer occur due the presence of a single dislocation line. Magnitude of tilt component and screw (twist) components are $\frac{a}{2}$ and $\frac{a\sqrt{2}}{4}$ respectively. The ratio of magnitudes of tilt component and twist component of 60° mixed dislocations is therefore 1.4. Hence, once tilt is measured then the value of twist can be simply estimated by dividing the tilt by a factor of 1.4.

Figure 5.6(b) shows the HRTEM image of a large cross sectional area of sample S4. In this figure, we find that the interface is not sharp and contains many dislocations. The presence of defect field at the interface is clearly seen in the image. The dislocation type is identified from the cross section HRTEM image. In **Figure 5.6(c)**, a small portion around the centre of **Figure 5.6(b)** is magnified to illustrate the arrangement of crystallographic planes. The red dotted lines show the orientation of $\{111\}$ crystallographic planes. Insertion of an extra half plane along with $\{111\}$

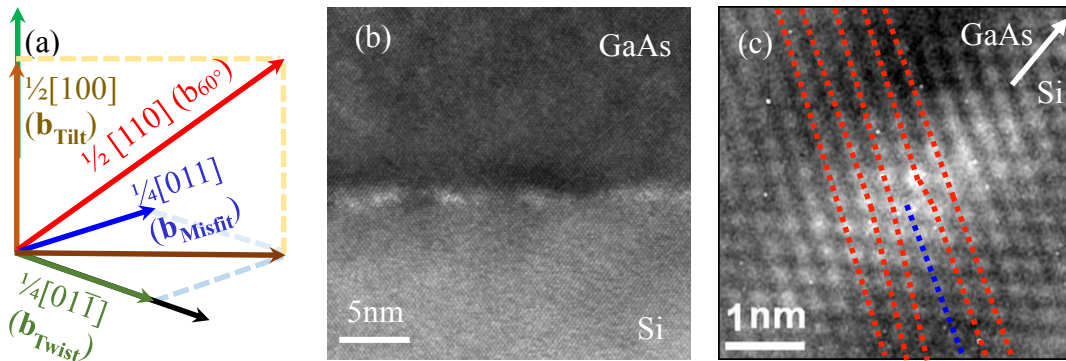


Figure 5.6 (a) The components of Burgers vector for 60° mixed dislocation, (b) cross section HRTEM image of sample S4, and (c) magnified HRTEM image around the centre of previous image.

crystallographic planes clearly confirms the presence of dislocations as shown by the blue dashed line. Burgers vector is inclined from (100) plane confirming that the dislocations are of 60° type.²¹⁴ Thus, it is concluded from the HRTEM images that the prevalent dislocations are 60° mixed dislocations present at the interface of GaAs/Si. Similar observations have been made by other researchers for several III-V heterostructure materials.^{152,214–216} In presence of 60° mixed dislocations, tilt will be equal to 1.4 times of the value of twist as mentioned in an earlier section of this chapter. From the measured values of tilt for the sample S2, S3 and S4, the twist values are calculated for the three samples and are listed in **Table 5.3**.

Table 5.3 Summary of the microstructure obtained from the modified Williamson-Hall analysis for the three GaAs/Si samples S2, S3 and S4.

Sample No.	Epilayer Thickness (μm)	LCL (μm)	Tilt (degree)	Twist (degree)	Tilt/Twist ratio	Twist by Burgers vector consideration ($^\circ$)	VCL (μm)	Microstrain (%)	Dislocation density estimated (cm^{-2})
S2	0.31	0.40	0.34	0.28	1.3	0.24	0.30	0.19	1.0×10^{10}
S3	0.31	0.31	0.28	0.22	1.3	0.20	0.34	0.14	6.8×10^9
S4	0.35	0.51	0.27	0.21	1.3	0.19	0.35	0.13	6.5×10^9

Note that the estimated values of twist are in reasonable agreement with those obtained from the modified WH analysis. Therefore, the proposed method of estimating the twist from Burgers vector consideration is acceptable. It totally avoids the requirement of acquiring numerous ω scans for different reflections and tedious fitting procedures are not at all needed. The calculated dislocation density of 60° perfect dislocation¹⁸⁹ is also shown in **Table 5.3**.

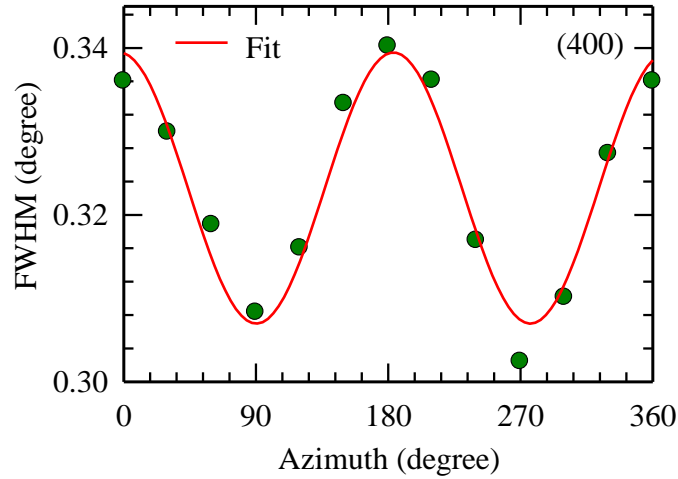


Figure 5.7 FWHMs of ω scans for (400) HRXRD pattern plotted as a function of azimuth.

5.3.3 Anisotropic distribution of microstructure in compressively strained GaAs/Si epitaxial layers

In this section, attention is paid to the anisotropic distribution of microstructure in compressively strained GaAs/Si epitaxial layers where the measurements are performed on a lab source based HRXRD setup. Several rocking curves are recorded at different azimuths varying from 0 to 360° where the results are summarized in **Figure 5.7**. It is observed that the value of FWHM of ω scans is larger at azimuth 0° in comparison to the one at azimuth 90°. It indicates that the density of defects/dislocations is high at azimuth 0° in comparison to the one at azimuth 90°. One can therefore conclude that the two orthogonal directions are significantly different from the microstructure point of view. It indicates about the presence of an anisotropic relaxation process which causes a large variation in FWHM of (400) diffraction peaks as shown in **Figure 5.7**. It therefore provides large differences in the values of microstructural parameters of GaAs epitaxial layer along the two in-plane orthogonal directions. Furthermore, the anisotropic behaviour of the relaxation process is expected to yield

very different values of microstructural parameters like lateral coherence length (LCL), tilt, and twist, etc., at the two azimuths. The value of LCL especially can be vastly different when HRXRD measurements are performed along various crystallographic directions. One therefore needs to be extremely cautious while comparing the value of microstructural parameters of the two samples. Extreme care needs to be taken to ensure that the same crystallographic direction in HRXRD measurements is selected while comparing different samples.

In modified Williamson–Hall analysis, (111), (333) and (444) reflections which make an angle of 54.73° with the plane parallel to the surface are chosen for studying the microstructure. It is important that none of these planes are affected by APDs and all of them are allowed reflections. One therefore get good data for all these reflections with a lab based HRXRD system and therefore the values of FWHM can be determined with high accuracy. **Figure 5.8(a)** shows the intensity vs. q_x curves obtained from ω scans for (111), (333) and (444) reflection of GaAs/Si sample. A pseudo-Voigt fitting of the curves is also shown by the overlaying lines in the figure. **Figure 5.8(b)** shows the modified WH plots using the ω scans for the GaAs/Si samples using (111), (333) and (444) reflections at orthogonal azimuths.¹⁰ The value of "n" used in the plots are determined from the pseudo-Voigt fitting of the ω scan profiles. The values of tilt (out-of-plane misorientation of the blocks) and the twist (in-plane misorientation of the blocks) are estimated by recording a set of reflections in the skew-symmetric geometry at both the azimuths and plotting the values of α_{hkl} of these reflections as a function of

ψ as shown in **Figure 5.9**. The values of tilt and twist are shown in the **Table 5.4**. The measured values of other microstructural parameters for the sample are also shown.

Table 5.4 Summary of microstructural parameters of GaAs/Si epitaxial layer obtained from the modified Williamson-Hall analysis of HRXRD data.

Azimuth (deg.)	WH analysis				Dominant dislocations	Dislocation density (cm ⁻²)
	<i>n</i>	LCL (Å)	Tilt and Twist			
			Tilt (Twist) (deg.)	Ratio		
0	1.4	3016	0.28 (0.2)	1.4	60° Perfect	6.6×10 ⁹
90	1.4	4317	0.26 (0.18)	1.4	60° Perfect	5.7×10 ⁹

Note that the tilt/twist ratio is nearly 1.4 at both the azimuths. It is also understood that the dislocations in compressively strained GaAs/Si epitaxial layers are mainly 60°

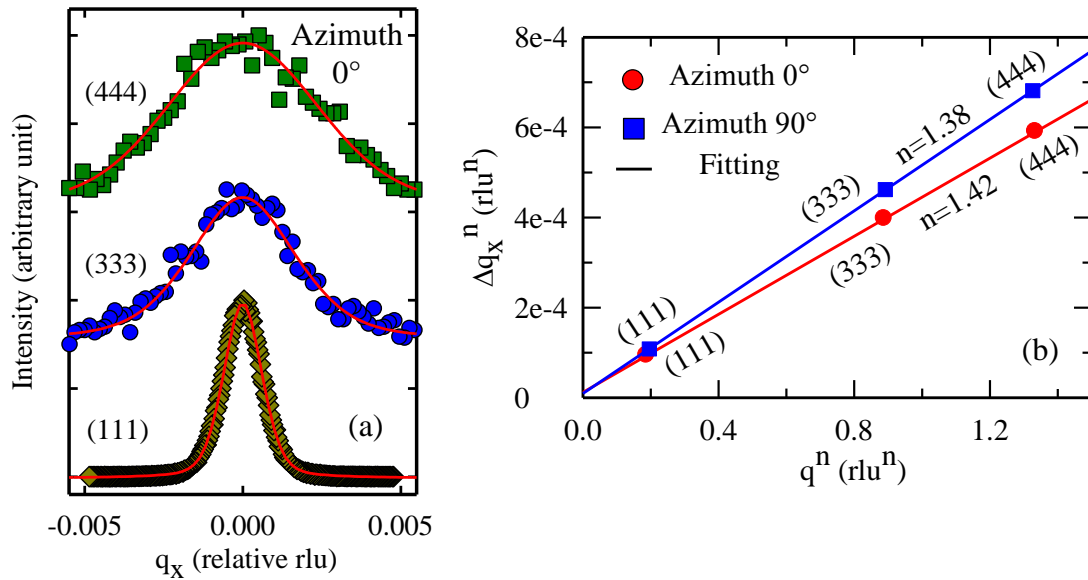


Figure 5.8 (a) Intensity versus q_x curves for (111), (333) and (444) reflection of GaAs/Si sample. The fitting of the curve is shown by overlaying line. (b) Modified Williamson-Hall plots prepared using ω scans for (111), (333), and (444) skew-symmetric reflections recorded using Cu $K\alpha_1$. The size of the error bars is smaller than the size of symbols.

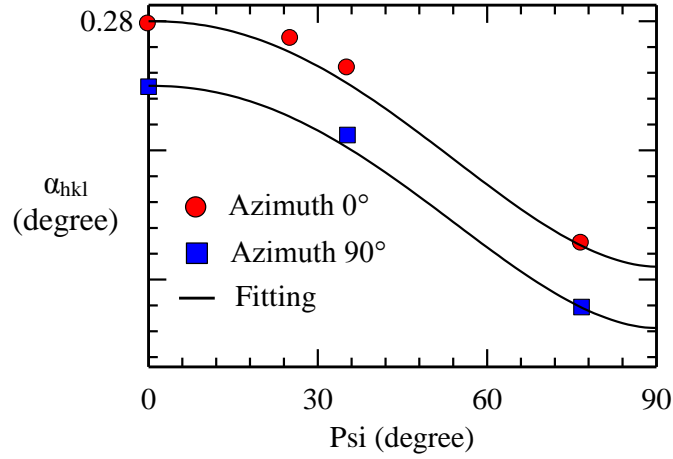


Figure 5.9 Variation of α_{hkl} for several skew-symmetric reflections.

perfect dislocations along both the directions since $\frac{\text{Tilt}}{\text{Twist}}$ ratio remains ≈ 1.4 .^{2,189} This is similar to our earlier observations made in case of compressively strained InP/GaAs epitaxial layers. Density of dislocations measured along the two directions is also shown in **Table 5.4**. Note that only a slight difference occurs between the dislocation densities since the relaxation process is significantly affected by the formation of APDs in the present case. The tilt/twist ratio shown in **Table 5.4**. at 0° and 90° azimuths is also ≈ 1.4 which confirms that anisotropic relaxation of GaAs/Si epilayers is mainly presence of 60° perfect dislocations.

5.4 Conclusion

Conventional WH analysis based on the HRXRD data acquired on a synchrotron radiation source is used to find the microstructure of GaAs epilayers grown on Si substrates where the values of LCL, VCL, tilt and the micro-strain are successfully measured. This information could not be obtained by performing similar experiments on a laboratory-based X-ray diffraction system. The high intensity and high energy of the incident X-ray beam, delivered by the Indus-2 synchrotron radiation source, are the

two critical parameters for these measurements. The values of LCL (VCL) are lower than the average grain size (layer thickness) obtained from AFM (surface profiler) measurements. This indicates the moderate crystalline quality of the epitaxial film, which is expected due to the lattice constant/thermal expansion coefficient differences between the layer and substrate. Although we have investigated GaAs epilayers grown on silicon substrates as an example, the proposed method is in general applicable for other semiconductor epilayers grown on foreign substrates.

Scheme of modified Williamson Hall analysis for evaluating the microstructures using skew symmetric (LLL) reflections ($L = 1, 3, 4$ etc.) successfully overcomes the limitations of weak intensity of (600) reflection by eliminating the low intensity and selective broadening issues. The estimated values of VCL are in strong corroboration with the values of epilayer thickness/granular size measured by the surface profiler. Furthermore, a straightforward method for estimating the values of twist between the mosaic blocks is proposed. It is based on Burgers vector considerations that totally avoids the requirement of acquiring numerous ω scans for different reflections and tedious fitting procedures are not at all needed. Presence of 60° mixed dislocations is clearly observed in cross sectional HRTEM images of GaAs/Si heterostructure. It is also found that a clear anisotropy exists in the microstructure of GaAs/Si epitaxial layers. However, only a slight difference occurs in the values of dislocation density which is significantly affected by the formation of APDs.

Chapter 6

Summary, Conclusion, and the Future Scope

6.1 Summary

In this thesis, HRXRD characterization of compressive and tensile strained III-V semiconductor epitaxial layers is carried out with an aim of understanding the anisotropic distribution of microstructure. In particular, GaP/GaAs, InP/GaAs, and GaAs/Si epitaxial layers are investigated in depth. These material combinations are interesting since 1) all the three combinations are nearly 4% lattice-mismatched systems, and 2) issues related to the growth of III-V semiconductors on polar/nonpolar substrates along with the type of strain i.e. compressive/tensile are addressed. HRXRD measurements in symmetric, skew-symmetric and asymmetric geometries are extensively performed on several samples by using the laboratory as well as synchrotron radiation based X-ray sources. We found that HRXRD is a powerful and versatile characterization tool to know the anisotropic distribution of microstructure, where predominant dislocations present in the zinc-blende layers can be identified rather quickly. Further, an estimate of the dislocation density in epitaxial layers can also be made. During this thesis, Williamson-Hall analysis is used to study various zinc-blende epitaxial layers. It is found that standard Williamson-Hall analysis can be used to understand the asymmetric distribution of microstructure in zinc-blende epitaxial layers grown on polar substrate irrespective of the type of residual strain. However, the method fails in case of epitaxial layers grown on nonpolar substrates. In that case, either the HRXRD measurements should be performed on a synchrotron radiation source or modified Williamson-Hall analysis, based on a set of skew-symmetric reflections, needs to be carried out in case the measurements are performed with a lab source. HRXRD

characterization results from three nearly 4% lattice-mismatched material combinations showed an anisotropic distribution of microstructure along the two in-plane orthogonal directions irrespective of the type of residual strain.

Anisotropic distribution of microstructure is observed in case of tensile strained GaP/GaAs epitaxial layers which causes a large difference in FWHM of (400) diffraction peaks of Omega scans along [011] and [01 $\bar{1}$] directions. The values of LCL, tilt, and twist along the two orthogonal directions are estimated by applying the Williamson-Hall analysis. It is found that the ratio of tilt and twist values is ≈ 1.3 and ≈ 2.9 predominantly governed by the dominance of 60° perfect and 90° partial dislocations with the line of dislocation along the [011] and [01 $\bar{1}$] directions, respectively. From Burgers vector analysis and HRTEM images it is found that tilt/twist ratio turns out to be 1.4 when 60° perfect dislocations are predominant. The tilt/twist ratio was found to be very large (≈ 2.9) along [011] direction in tensile strained GaP layers grown on GaAs substrates. From Burgers vector analysis, it is found that a high value of tilt/twist ratio indicates about the dominance of 90° partial dislocations in strain relaxation. The same is confirmed by the formation of stacking faults in tensile strained GaP/GaAs epilayers which is observed in HRTEM images. It is proposed that 90° partial dislocations are primarily responsible for initial relaxation of the layer while 60° perfect dislocations dominate the relaxation process beyond a certain layer thickness in case of tensile strained GaP/GaAs epilayers.

In case of compressively strained InP/GaAs epitaxial layers, it is found that the same type of dislocations i.e. 60° perfect dislocations are responsible for lattice relaxation along both the crystallographic directions. Here, the anisotropy in microstructures occurs mainly due to the difference in the density of dislocations along

the two directions. Density of dislocations in compressively strained epitaxial layers as well as tensile strained layers are mainly governed by the glide velocity of α and β dislocations which dominate the lattice relaxation process along the two in-plane orthogonal directions. Changes in the type of relaxations are also observed in the AFM images of these samples where fine cracks running along $[01\ 1]$ direction are evident in tensile strained layers whereas no cracks are seen in case of compressively strained layers. The anisotropy in microstructure is also compared with anisotropic optical quality of epilayers with the help of polarization dependent PL spectroscopy for one of the sample. It is found that optical quality seamlessly follows the anisotropy seen in the microstructural properties. A method based on random distribution of dislocations and Burgers vector analysis is also presented for estimating the values of dislocation density in these layers.

In case of compressively strained GaAs/Si epitaxial layers, it is found that the conventional WH analysis can only be carried out by acquiring HRXRD data on a synchrotron radiation source. A similar information could not be obtained by performing similar experiments on a laboratory-based HRXRD system. A high intensity/energy of the incident X-ray beam at BL-12 of Indus-2 plays a key role in overcoming the limitations posed by a laboratory based X-ray source. By comparing the results of WH analysis on several samples, it is understood that one should choose a lower temperature for the growth of buffer layer. Further, the ratio of tilt and twist turns out to be 1.3 which indicates about the dominance of 60° perfect dislocations in the relaxation process. The same is also confirmed by the HRTEM technique. A slight asymmetry in the values of microstructure along the two in-plane orthogonal directions is observed which is governed by the difference in the glide velocity of respective

dislocations and the formation of APDs in epitaxial layer. Further, it is also understood that if the type of dominant dislocations is known a priori then the value of twist can be estimated by measuring the tilt alone.

6.2 Conclusion

An anisotropic distribution of microstructure is observed where the origin of anisotropy is found to depend on the nature of strain and the choice of polar/nonpolar substrate. A quick identification of dislocation type and estimation of the dislocation density is possible by HRXRD technique. It is found that anisotropy in the crystalline quality of epilayers is consistent with the optical quality. The limitation imposed by the weak intensity of reflections which is more evident in layers grown on non-polar substrates for finding the microstructure from Williamson-Hall analysis can be overcome by the use of intense and wavelength tunable synchrotron radiation source. Alternatively, modified Williamson-Hall analysis can be performed on the data acquired using laboratory source which also gives the required information although along a different direction. The present work is useful in understanding the relaxation process in compressive and tensile strained III-V semiconductor epitaxial layers which is expected to help in the development of novel semiconductor devices based on such materials.

6.3 Suggestions for future work

As part of future work, it is proposed to study a few other lattice-mismatched system e.g. GaP/Ge, AlAs/Si etc. which shall help in developing a robust understanding about the lattice relaxation process in such material combinations. The understanding developed for zinc-blende systems can also be helpful in understanding the relaxation

mechanism in wurtzite systems e.g. GaN/Sapphire, GaN/SiC etc. Modified Williamson-Hall analysis can also be useful in studying wurtzite materials system by selecting an appropriate set of reflections. Other techniques like extended X-ray absorption fine structure (EXAFS) and X-ray absorption near edge structure (XANES) can also be applied to understand the anisotropic strain relaxation by measuring the bond lengths.

References

- ¹ D. A. Neumann, H. Zabel, R. Fischer, and H. Morkoç, J Appl Phys **61**, 1023 (1987).
- ² R. Kumar, V.K. Dixit, T. Ganguli, C. Mukherjee, A.K. Srivastava, and T.K. Sharma, J. Appl. Phys. **120**, 135307 (2016).
- ³ R. Kumar, V.K. Dixit, A.K. Sinha, T. Ganguli, C. Mukherjee, S.M. Oak, and T.K. Sharma, J. Synchrotron Radiat. **23**, (2016).
- ⁴ Ravi Kumar, Tapas Ganguli, Vijay Chouhan, V. K. Dixit, Puspen Mondal, A. K. Srivastava, C. Mukherjee, and T. K. Sharma, J Nano- Electron Phys **6**, 02010 (2014).
- ⁵ Ravi Kumar, Tapas Ganguli, Vijay Chouhan, and V K Dixit, J Nano- Electron Phys **3**, 17 (2011).
- ⁶ V.K. Khanna, *Fundamentals of Solid-State Lighting: LEDs, OLEDs, and Their Applications in Illumination and Displays* (CRC Press, 2014).
- ⁷ S. Kasap and P. Capper, *Springer Handbook of Electronic and Photonic Materials* (Springer, 2006).
- ⁸ S.L. Morelhão, L.H. Avanci, L.P. Cardoso, F. Riesz, K. Rakennus, and T. Hakkarainen, Vacuum **46**, 1013 (1995).
- ⁹ A.K. Sinha, A. Sagdeo, P. Gupta, A. Upadhyay, A. Kumar, M.N. Singh, R.K. Gupta, S.R. Kane, A. Verma, and S.K. Deb, J. Phys. Conf. Ser. **425**, 072017 (2013).
- ¹⁰ Vijay Chouhan, High Resolution X-Ray Diffraction of Semiconductor Epilayers, M. Tech. Dissertation, Shri G. S. Insitute of Technology and Science, 2008.
- ¹¹ Pallab Bhattacharya, *Semiconductor Optoelectronic Devices*, Second (PHI Learning Private Limited, New Delhi, 2011).
- ¹² M A Moram and M E Vickers, Rep Prog Phys **72**, 036502 (2009).

- ¹³ H. Morkoç, in *Handb. Nitride Semicond. Devices* (Wiley-VCH Verlag GmbH & Co. KGaA, 2009), pp. 1231–1255.
- ¹⁴ J.E. Ayers, *Heteroepitaxy of Semiconductors: Theory, Growth, and Characterization* (CRC Press, 2007).
- ¹⁵ S. Nakamura and G. Fasol, *The Blue Laser Diode: GaN Based Light Emitters and Lasers* (Springer Berlin Heidelberg, 2013).
- ¹⁶ E.A. Fitzgerald, Mater. Sci. Rep. **7**, 87 (1991).
- ¹⁷ F.C. Frank and J. H. van der Merwe, Proc. R. Soc. Lond. Math. Phys. Eng. Sci. **198**, 205 (1949).
- ¹⁸ F.C. Frank and J.H. van der Merwe, Proc. R. Soc. Lond. Math. Phys. Eng. Sci. **198**, 216 (1949).
- ¹⁹ F.C. Frank and J. H. van der Merwe, Proc. R. Soc. Lond. Math. Phys. Eng. Sci. **200**, 125 (1949).
- ²⁰ F.C. Frank and J. H. van der Merwe, Proc. R. Soc. Lond. Math. Phys. Eng. Sci. **201**, 261 (1950).
- ²¹ J.H.V.D. Merwe, J. Appl. Phys. **34**, 117 (1963).
- ²² J.H.V.D. Merwe, J. Appl. Phys. **34**, 123 (1963).
- ²³ W.A. Jesser and D. Kuhlmann-Wilsdorf, Phys. Status Solidi B **19**, 95 (1967).
- ²⁴ W.A. Jesser and J.W. Matthews, Philos. Mag. J. Theor. Exp. Appl. Phys. **15**, 1097 (1967).
- ²⁵ W.A. Jesser and J.W. Matthews, Philos. Mag. J. Theor. Exp. Appl. Phys. **17**, 461 (1968).
- ²⁶ W.A. Jesser and J.W. Matthews, Philos. Mag. J. Theor. Exp. Appl. Phys. **17**, 595 (1968).

- ²⁷ J.W. Matthews, S. Mader, and T.B. Light, *J. Appl. Phys.* **41**, 3800 (1970).
- ²⁸ J.W. Matthews and J.L. Crawford, *Thin Solid Films* **5**, 187 (1970).
- ²⁹ P. Haasen, *Acta Metall.* **5**, 598 (1957).
- ³⁰ E.A. Fitzgerald, G.P. Watson, R.E. Proano, D.G. Ast, P.D. Kirchner, G.D. Pettit, and J.M. Woodall, *J. Appl. Phys.* **65**, 2220 (1989).
- ³¹ L. Esaki and R. Tsu, *IBM J. Res. Dev.* **14**, 61 (1970).
- ³² J.W. Matthews and A.E. Blakeslee, *J. Cryst. Growth* **27**, 118 (1974).
- ³³ T.J. Drummond, W. Kopp, R. Fischer, H. Morkoç, R.E. Thorne, and A.Y. Cho, *J. Appl. Phys.* **53**, 1238 (1982).
- ³⁴ R. Fischer, T.J. Drummond, J. Klem, W. Kopp, T.S. Henderson, D. Perrachione, and H. Morkoc, *IEEE Trans. Electron Devices* **31**, 1028 (1984).
- ³⁵ T. Henderson, M. Aksun, C. Peng, H. Morkoc, P. Chao, P. Smith, K.-H. Duh, and L. Lester, *IEEE Electron Device Lett.* **7**, 649 (1986).
- ³⁶ A. Okamoto, H. Toyoshima, and K. Ohata, *Jpn. J. Appl. Phys.* **26**, 539 (1987).
- ³⁷ S.-M. Liu, M.B. Das, C.K. Peng, J. Klem, T. Henderson, W. Kopp, and H. Morkoç, *J. Cryst. Growth* **81**, 359 (1987).
- ³⁸ S. Yamakoshi, M. Abe, O. Wada, S. Komiya, and T. Sakurai, *IEEE J. Quantum Electron.* **17**, 167 (1981).
- ³⁹ D.G. Deppe, D.W. Nam, N.H. Jr, K.C. Hsieh, R.J. Matyi, H. Shichijo, J.E. Epler, and H.F. Chung, *Appl. Phys. Lett.* **51**, 1271 (1987).
- ⁴⁰ S. Essig, M.A. Steiner, C. Allebé, J.F. Geisz, B. Paviet-Salomon, S. Ward, A. Descoeudres, V. LaSalvia, L. Barraud, N. Badel, A. Faes, J. Levrat, M. Despeisse, C. Ballif, P. Stradins, and D.L. Young, *IEEE J. Photovolt.* **6**, 1012 (2016).

- ⁴¹ S. Essig, J. Benick, M. Schachtner, A. Wekkeli, M. Hermle, and F. Dimroth, *IEEE J. Photovolt.* **5**, 977 (2015).
- ⁴² S.M. Islam, P. Biswas, P. Banerji, and S. Chakraborty, *Mater. Sci. Eng. B* **198**, 102 (2015).
- ⁴³ V. Tassev, M. Snure, R. Peterson, K.L. Schepler, R. Bedford, M. Mann, S. Vangala, W. Goodhue, A. Lin, J. Harris, M. Fejer, and P. Schunemann, in *Proc SPIE 8604* (2013), pp. 86040V-86040V–9.
- ⁴⁴ S. Vangala, M. Kimani, R. Peterson, R. Stites, M. Snure, and V. Tassev, *Opt. Mater.* **60**, 62 (2016).
- ⁴⁵ P. Sheldon, K. M. Jones, M. M. Al-Jassim, and B. G. Yacobi, *J Appl Phys* **63**, 5609 (1988).
- ⁴⁶ M.J. Matragrano, D.G. Ast, J.R. Shealy, and V. Krishnamoorthy, *J. Appl. Phys.* **79**, 8371 (1996).
- ⁴⁷ M. Dynna and A. Marty, *Acta Mater.* **46**, 1087 (1998).
- ⁴⁸ G. Naresh-Kumar, A. Vilalta-Clemente, H. Jussila, A. Winkelmann, G. Nolze, S. Vespucci, S. Nagarajan, A.J. Wilkinson, and C. Trager-Cowan, *Sci. Rep.* **7**, 10916 (2017).
- ⁴⁹ R. Kumar, V.K. Dixit, A.K. Sinha, T. Ganguli, C. Mukherjee, S.M. Oak, and T.K. Sharma, *J. Synchrotron Radiat.* **23**, 238 (2016).
- ⁵⁰ R.E. Smallman, *Modern Physical Metallurgy* (Elsevier Science, 2013).
- ⁵¹ H. Suzuki, T. Sasaki, A. Sai, Y. Ohshita, I. Kamiya, M. Yamaguchi, M. Takahasi, and S. Fujikawa, *Appl. Phys. Lett.* **97**, 041906 (2010).
- ⁵² Ł. Gelczuk, M. Dąbrowska-Szata, J. Serafińczuk, A. Masalska, E. Łusakowska, and P. Dłużewski, *Mater. Sci.-Pol.* **26**, 157 (2008).

- ⁵³ O. Yastrubchak, J.Z. Domagała, T. Wosiński, A. Kudła, and K. Regiński, *Phys. Status Solidi C* **2**, 1943 (2005).
- ⁵⁴ Ł. Gelczuk, D. Pucicki, J. Serafińczuk, M. Dąbrowska-Szata, and P. Dłużewski, *J. Cryst. Growth* **430**, 14 (2015).
- ⁵⁵ R. France, A. J. Ptak, C. -S. Jiang, and S. P. Ahrenkiel, *J Appl Phys* **107**, 103530 (2010).
- ⁵⁶ R.S. Goldman, H.H. Wieder, and K.L. Kavanagh, *Appl. Phys. Lett.* **67**, 344 (1995).
- ⁵⁷ S.K. Choi, M. Mihara, and T. Ninomiya, *Jpn. J. Appl. Phys.* **16**, 737 (1977).
- ⁵⁸ K. Wasmer, M. Parlinska-Wojtan, R. Gassilloud, C. Pouvreau, J. Tharian, and J. Micher, *Appl. Phys. Lett.* **90**, 031902 (2007).
- ⁵⁹ R.S. Goldman, K.L. Kavanagh, H.H. Wieder, S.N. Ehrlich, and R.M. Feenstra, *J. Appl. Phys.* **83**, 5137 (1998).
- ⁶⁰ L. Largeau, G. Patriarche, F. Glas, and E. Le Bourhis, *J. Appl. Phys.* **95**, 3984 (2004).
- ⁶¹ Y. Li and M. Niewczas, *J. Appl. Phys.* **101**, 064910 (2007).
- ⁶² H.L. Tsai and Y.C. Kao, *J. Appl. Phys.* **67**, 2862 (1990).
- ⁶³ J. Petruzzello and M.R. Leys, *Appl. Phys. Lett.* **53**, 2414 (1988).
- ⁶⁴ R. Hull, R.A. Logan, B.E. Weir, and J.M. Vandenberg, *Appl. Phys. Lett.* **63**, 1504 (1993).
- ⁶⁵ B.R. Bennett and J.A. del Alamo, *Appl. Phys. Lett.* **58**, 2978 (1991).
- ⁶⁶ F. Peiró, A. Cornet, and J.R. Morante, *J. Appl. Phys.* **77**, 4993 (1995).
- ⁶⁷ M. Grundmann, U. Lienert, D. Bimberg, A. Fischer-Colbrie, and J.N. Miller, *Appl. Phys. Lett.* **55**, 1765 (1989).
- ⁶⁸ M. Li, Y. Qiu, G. Liu, Y. Wang, B. Zhang, and L. Zhao, *J. Appl. Phys.* **105**, 094903 (2009).

- ⁶⁹ X. Weng, R. S. Goldman, D. L. Partin, and J. P. Heremans, *J Appl Phys* **88**, 6276 (2000).
- ⁷⁰ M.K. Hudait, Y. Lin, and S.A. Ringel, *J. Appl. Phys.* **105**, 061643 (2009).
- ⁷¹ Y.U. Wang, Y.M. Jin, and A.G. Khachatryan, in *Handb. Mater. Model. Methods*, edited by S. Yip (Springer Netherlands, Dordrecht, 2005), pp. 2287–2305.
- ⁷² W.D. Lee, J. Drazen, P.A. Sharp, and R.S. Langer, *From X-Rays to DNA: How Engineering Drives Biology* (MIT Press, 2013).
- ⁷³ D.K. Bowen and B.K. Tanner, *X-Ray Metrology in Semiconductor Manufacturing* (CRC Press, 2006).
- ⁷⁴ A.G. Michette and S. Pfauntsch, *X-Rays: The First Hundred Years* (John Wiley & Sons, 1996).
- ⁷⁵ J.P. Glusker and K.N. Trueblood, *Crystal Structure Analysis: A Primer* (OUP Oxford, 2010).
- ⁷⁶ A. Authier, *Early Days of X-Ray Crystallography* (OUP Oxford, 2013).
- ⁷⁷ R.K. Harris, R.E. Wasylshen, and M.J. Duer, *NMR Crystallography* (Wiley, 2012).
- ⁷⁸ *Introduction to Solid State Physics, 77th Ed* (Wiley India Pvt. Limited, 2007).
- ⁷⁹ B.B. He, *Two-Dimensional X-Ray Diffraction* (Wiley, 2018).
- ⁸⁰ W. Massa and R.O. Gould, *Crystal Structure Determination* (Springer Berlin Heidelberg, 2013).
- ⁸¹ B.D. Cullity, *Elements of X-Ray Diffraction* (Addison- Wesley, Reading, MA, 1956).
- ⁸² Paul F. Fewster, *X-Ray Scattering from Semiconductors and Other Materials*, 3rd (World Scientific, 2013).
- ⁸³ Philips Analytical X-ray (PANalytical), *X’Pert-MPD System – User Guide*, Second (Philips Electronic N.V., Netherlands, 1995).

- ⁸⁴ U. Shmueli, *Theories and Techniques of Crystal Structure Determination* (OUP Oxford, 2007).
- ⁸⁵ M. Sardela, *Practical Materials Characterization* (Springer New York, 2014).
- ⁸⁶ P. H. Dowling, C. F. Hendee, T. R. Kohler, and W. Parrish, *Philips Tech. Rev.* **18**, 262 (1956).
- ⁸⁷ C. Suryanarayana and M.G. Norton, *X-Ray Diffraction: A Practical Approach* (Springer US, 1998).
- ⁸⁸ U. Pietsch, V. Holy, and T. Baumbach, *High-Resolution X-Ray Scattering: From Thin Films to Lateral Nanostructures* (Springer New York, 2013).
- ⁸⁹ S.K. Deb, G. Singh, and P.D. Gupta, *J. Phys. Conf. Ser.* **425**, 072009 (2013).
- ⁹⁰ S.-K. Wang, P. Dai, and H. Taub, *J. Appl. Crystallogr.* **26**, 697 (1993).
- ⁹¹ G.B. Saha, *Physics and Radiobiology of Nuclear Medicine* (Springer New York, 2013).
- ⁹² G.S. Brady, *Materials Handbook* (McGraw-Hill, 1963).
- ⁹³ G.F. Knoll, *Radiation Detection and Measurement* (John Wiley & Sons, 2010).
- ⁹⁴ P. Erhart, A. Schleife, B. Sadigh, and D. Åberg, *Phys Rev B* **89**, 075132 (2014).
- ⁹⁵ D.L. Bailey, D.W. Townsend, P.E. Valk, and M.N. Maisey, *Positron Emission Tomography: Basic Sciences* (Springer London, 2004).
- ⁹⁶ Y.M. Tsipenyuk, *Physical Methods, Instruments and Measurements – Volume II* (2009).
- ⁹⁷ P.R.S. Kumar, *Photonics* (PHI Learning, 2012).
- ⁹⁸ R. Roychowdhury, S. Kumar, A. Wadikar, C. Mukherjee, K. Rajiv, T.K. Sharma, and V.K. Dixit, *Appl. Surf. Sci.* **419**, 957 (2017).
- ⁹⁹ Q. Yang, F. Williams, X. Zhao, C.E. Reece, and M. Krishnan, in (2013).

- ¹⁰⁰ M. Lanza, *Conductive Atomic Force Microscopy: Applications in Nanomaterials* (Wiley, 2017).
- ¹⁰¹ A.M. Baró and R.G. Reifengerger, *Atomic Force Microscopy in Liquid: Biological Applications* (Wiley, 2012).
- ¹⁰² P.C. Braga and D. Ricci, *Atomic Force Microscopy: Biomedical Methods and Applications* (Humana Press, 2004).
- ¹⁰³ D.G. Capco and yongsheng chen, *Nanomaterial: Impacts on Cell Biology and Medicine* (Springer Netherlands, 2014).
- ¹⁰⁴ A. Rosenauer, *Transmission Electron Microscopy of Semiconductor Nanostructures: An Analysis of Composition and Strain State* (Springer Berlin Heidelberg, 2003).
- ¹⁰⁵ B. Fultz and J.M. Howe, *Transmission Electron Microscopy and Diffractometry of Materials* (Springer Berlin Heidelberg, 2012).
- ¹⁰⁶ A. Méndez-Vilas and J. Díaz, *Microscopy: Science, Technology, Applications and Education* (Formatex Research Center, 2010).
- ¹⁰⁷ K. Ito, *Copper Zinc Tin Sulfide-Based Thin-Film Solar Cells* (Wiley, 2014).
- ¹⁰⁸ X.C.T.P. D, *Advanced Materials for Integrated Optical Waveguides* (Springer International Publishing, 2013).
- ¹⁰⁹ D.C. Harris, *Infrared Window and Dome Materials* (SPIE Optical Engineering Press, 1992).
- ¹¹⁰ M.A. Herman, W. Richter, and H. Sitter, *Epitaxy: Physical Principles and Technical Implementation* (Springer Berlin Heidelberg, 2013).
- ¹¹¹ M. Razeghi, *The MOCVD Challenge: Volume 2: A Survey of GaInAsP-GaAs for Photonic and Electronic Device Applications* (Taylor & Francis, 1995).

- ¹¹² R. Szweda, *Gallium Arsenide, Electronics Materials and Devices. A Strategic Study of Markets, Technologies and Companies Worldwide 1999-2004* (Elsevier Science, 2000).
- ¹¹³ G.B. Stringfellow, *Organometallic Vapor-Phase Epitaxy: Theory and Practice* (Elsevier Science, 2012).
- ¹¹⁴ G K Williamson and W H Hall, *Acta Metall.* **1**, 22 (1953).
- ¹¹⁵ S R Lee, A M West, A A Allerman, K E Waldrip, D M Follstaedt, P P Proventio, D D Koleske, and C R Abernathy, *Appl Phys Lett* **86**, 241904 (2005).
- ¹¹⁶ Brajesh S Yadav, Sukhvinder Singh, Tapas Ganguli, Ravi Kumar, S S Major, and R S Srinivasa, *Thin Solid Films* **517**, 488 (2008).
- ¹¹⁷ Tapas Ganguli, Abdul Kadir, Mahesh Gokhale, Ravi Kumar, A P Shah, B M Arora, and Arnab Bhattacharya, *J Cryst Growth* **310**, 4942 (2008).
- ¹¹⁸ X.L. Zhu, L.W. Guo, N.S. Yu, J.F. Yan, M.Z. Peng, J. Zhang, H.Q. Jia, H. Chen, and J.M. Zhou, *J. Cryst. Growth* **306**, 292 (2007).
- ¹¹⁹ V K Dixit, Tapas Ganguli, T K Sharma, S D Singh, Ravi Kumar, S Porwal, Pragya Tiwari, Alka Ingale, and S M Oak, *J Cryst Growth* **310**, 3428 (2008).
- ¹²⁰ V. Srikant, J.S. Speck, and D.R. Clarke, *J. Appl. Phys.* **82**, 4286 (1997).
- ¹²¹ R. Chierchia, T. Böttcher, H. Heinke, S. Einfeldt, S. Figge, and D. Hommel, *J. Appl. Phys.* **93**, 8918 (2003).
- ¹²² F. Sánchez-Bajo and F.L. Cumbreira, *J. Appl. Crystallogr.* **30**, 427 (1997).
- ¹²³ A.G. Taboada, M. Meduña, M. Salvalaglio, F. Isa, T. Kreiliger, C.V. Falub, E. Barthazy Meier, E. Müller, L. Miglio, G. Isella, and H. von Känel, *J. Appl. Phys.* **119**, 055301 (2016).

- ¹²⁴ T. Orzali, A. Vert, B. O'Brien, J.L. Herman, S. Vivekanand, R.J.W. Hill, Z. Karim, and S.S. Papa Rao, J. Appl. Phys. **118**, 105307 (2015).
- ¹²⁵ P. Mukhopadhyay, R. Kumar, S. Ghosh, A. Chakraborty, A. Bag, S. Kabi, P. Banerji, and D. Biswas, J. Cryst. Growth **418**, 138 (2015).
- ¹²⁶ C.-H. Cheng, A.-J. Tzou, J.-H. Chang, Y.-C. Chi, Y.-H. Lin, M.-H. Shih, C.-K. Lee, C.-I. Wu, H.-C. Kuo, C.-Y. Chang, and G.-R. Lin, Sci. Rep. **6**, 19757 (2016).
- ¹²⁷ S. Nakamura and M.R. Krames, Proc. IEEE **101**, 2211 (2013).
- ¹²⁸ Y. Sun, K. Zhou, Q. Sun, J. Liu, M. Feng, Z. Li, Y. Zhou, L. Zhang, D. Li, S. Zhang, M. Ikeda, S. Liu, and H. Yang, Nat Photon **advance online publication**, (2016).
- ¹²⁹ S. Nakamura, S. Pearton, and G. Fasol, *The Blue Laser Diode: The Complete Story* (Springer Berlin Heidelberg, 2013).
- ¹³⁰ S. Wirths, R. Geiger, N. von den Driesch, G. Mussler, T. Stoica, S. Mantl, Z. Ikonik, M. Luysberg, S. Chiussi, J. M. Hartmann, H. Sigg, J. Faist, D. Buca, and D. Grützmacher, Nat Photon **9**, 88 (2015).
- ¹³¹ L. Pavesi, S. Gaponenko, and L.D. Negro, *Towards the First Silicon Laser* (Springer Netherlands, 2012).
- ¹³² J. Kühn, *AlGaIn-GaN-HEMT Power Amplifiers with Optimized Power-Added Efficiency for X-Band Applications* (KIT Scientific Publ., 2011).
- ¹³³ B. Yarlagadda, A. Rodriguez, P. Li, R. Velampati, J.F. Ocampo, E.N. Suarez, P.B. Rago, D. Shah, J.E. Ayers, and F.C. Jain, Appl. Phys. Lett. **92**, 202103 (2008).
- ¹³⁴ P.M.J. Marée, J.C. Barbour, J.F. van der Veen, K.L. Kavanagh, C.W.T. Bulle-Lieuwma, and M.P.A. Vieggers, J. Appl. Phys. **62**, 4413 (1987).
- ¹³⁵ Y.B. Bolkhovityanov and O.P. Pchelyakov, Phys.-Uspekhi **51**, 437 (2008).

- ¹³⁶ W. Wang, T. Yan, W. Yang, Y. Zhu, H. Wang, G. Li, and N. Ye, *CrystEngComm* **18**, 4688 (2016).
- ¹³⁷ G. Bhagavannarayana, S. Parthiban, and S. Meenakshisundaram, *J. Appl. Crystallogr.* **39**, 784 (2006).
- ¹³⁸ Y. Chen, D. Bagnall, and T. Yao, *Mater. Sci. Eng. B* **75**, 190 (2000).
- ¹³⁹ H. Suzuki, T. Matsushita, M. Katayama, K. Maeda, and T. Ikari, *Jpn. J. Appl. Phys.* **53**, 018001 (2014).
- ¹⁴⁰ Q. Ni, Z. Qiu, B. Yu, X. Liu, T. Zhang, and Y. Wang, in *Optoelectron. Microelectron. ICOM 2012 Int. Conf. On* (2012), pp. 1–4.
- ¹⁴¹ P.J. Simmonds and M. Larry Lee, *Appl. Phys. Lett.* **99**, 123111 (2011).
- ¹⁴² P.J. Simmonds and M.L. Lee, *Appl. Phys. Lett.* **97**, 153101 (2010).
- ¹⁴³ Shailesh K. Khamari, V. K. Dixit, Tapas Ganguli, S. D. Singh, C. Mukharjee, Alka Ingale, U.P. Deshpande, T. Shripathi, and S. M. Oak, in *E-Proc. Natl. Laser Symp.-19* (Raja Ramanna Centre for Advanced Technology, Indore, 2010).
- ¹⁴⁴ D.K. Bowen and B.K. Tanner, *High Resolution X-Ray Diffractometry And Topography* (CRC Press, 2005).
- ¹⁴⁵ Halliwell M.A.G., *Advances in X-Ray Analysis* (Plenum Press, New York, 1990).
- ¹⁴⁶ J.E. Ayers, *J. Cryst. Growth* **135**, 71 (1994).
- ¹⁴⁷ A. Mazuelas, L. González, F.A. Ponce, L. Tapfer, and F. Briones, *J. Cryst. Growth* **131**, 465 (1993).
- ¹⁴⁸ A. Freundlich, A. Bensaoula, A.H. Bensaoula, and V. Rossignol, *J. Vac. Sci. Technol. B* **11**, 843 (1993).
- ¹⁴⁹ K. Yuan, K. Radhakrishnan, H.Q. Zheng, Q.D. Zhuang, and G.I. Ing, *Thin Solid Films* **391**, 36 (2001).

- ¹⁵⁰ D.B. Holt and B.G. Yacobi, *Extended Defects in Semiconductors: Electronic Properties, Device Effects and Structures* (Cambridge University Press, 2007).
- ¹⁵¹ T.K. Koo, B. O. Y.-M. Yu, D.-J. Kim, C.-S. Kim, Y.D. Choi, J.W. Lee, M.-Y. Yoon, P.Y. Yu, and T.W. Kang, J. Appl. Phys. **108**, 113508 (2010).
- ¹⁵² Y. Qiu, M. Li, G. Liu, B. Zhang, Y. Wang, and L. Zhao, J. Cryst. Growth **308**, 325 (2007).
- ¹⁵³ S.R. Lee, A.M. West, A.A. Allerman, K.E. Waldrup, D.M. Follstaedt, P.P. Provencio, D.D. Koleske, and C.R. Abernathy, Appl. Phys. Lett. **86**, 241904 (2005).
- ¹⁵⁴ F. Peiró, A. Cornet, and J.R. Morante, Mater. Sci. Technol. **13**, 957 (1997).
- ¹⁵⁵ Y. Qiu, M. Li, Y. Wang, B. Zhang, Y. Wang, G. Liu, and L. Zhao, Phys. Scr. **2007**, 27 (2007).
- ¹⁵⁶ Freundlich, A., J Phys Colloq. **50**, C5 (1989).
- ¹⁵⁷ L. Li, Z. Gan, M.R. McCartney, H. Liang, H. Yu, Y. Gao, J. Wang, and D.J. Smith, Sci. Rep. **3**, 3229 (2013).
- ¹⁵⁸ P.D. Brown, Y.Y. Loginov, W.M. Stobbs, and C.J. Humphreys, Philos. Mag. A **72**, 39 (1995).
- ¹⁵⁹ X. Wu and G.C. Weatherly, Philos. Mag. Lett. **80**, 535 (2000).
- ¹⁶⁰ Stringfellow, *Gallium Arsenide and Related Compounds 1991, Proceedings of the Eighteenth INT Symposium, 9-12 September 1991, Seattle, USA* (Taylor & Francis, 1992).
- ¹⁶¹ K. Sumino, *Defect Control in Semiconductors* (Elsevier Science, 2012).
- ¹⁶² J. Godet, L. Pizzagalli, S. Brochard, and P. Beauchamp, Phys Rev B **70**, 054109 (2004).
- ¹⁶³ T.P. Darby and R.W. Balluffi, Philos. Mag. **36**, 53 (1977).

- ¹⁶⁴ F. Peiró, A. Cornet, and J.R. Morante, *J. Vac. Sci. Technol. B Microelectron. Nanometer Struct. Process. Meas. Phenom.* **13**, 2057 (1995).
- ¹⁶⁵ W. Wegscheider and H. Cerva, *J. Vac. Sci. Technol. B* **11**, 1056 (1993).
- ¹⁶⁶ R.M. Lum, J.K. Klingert, R.B. Bylsma, A.M. Glass, A.T. Macrander, T.D. Harris, and M.G. Lamont, *J. Appl. Phys.* **64**, 6727 (1988).
- ¹⁶⁷ K.L. Li, Y.R. Sun, J.R. Dong, Y.M. Zhao, S.Z. Yu, C.Y. Zhao, X.L. Zeng, and H. Yang, *J. Cryst. Growth* **380**, 261 (2013).
- ¹⁶⁸ S. Rubini, B. Bonanni, E. Pelucchi, A. Franciosi, A. Garulli, A. Parisini, Y. Zhuang, G. Bauer, and V. Holý, *J. Vac. Sci. Technol. B Microelectron. Nanometer Struct. Process. Meas. Phenom.* **18**, 2263 (2000).
- ¹⁶⁹ T Metzger, R Höpler, E Born, O Ambacher, M Stutzmann, R Stömmer, M Schuster, H Göbel, S Christiansen, M Albrecht, and H P Strunk, *Philos Mag A* **77**, 1013 (1998).
- ¹⁷⁰ P.F. Fewster, *Rep. Prog. Phys.* **59**, 1339 (1996).
- ¹⁷¹ M. Nemoz, R. Dagher, S. Matta, A. Michon, P. Vennéguès, and J. Brault, *J. Cryst. Growth* **461**, 10 (2017).
- ¹⁷² C.G. Dunn and E.F. Kogh, *Acta Metall.* **5**, 548 (1957).
- ¹⁷³ V.M. Kaganer, O. Brandt, A. Trampert, and K.H. Ploog, *Phys Rev B* **72**, 045423 (2005).
- ¹⁷⁴ P. Gay, P.B. Hirsch, and A. Kelly, *Acta Metall.* **1**, 315 (1953).
- ¹⁷⁵ A.D. Kurtz, S.A. Kulin, and B.L. Averbach, *Phys Rev* **101**, 1285 (1956).
- ¹⁷⁶ Y. Zhang, Z. Xing, Z. Ma, Y. Chen, G. Ding, P. Xu, C. Dong, H. Chen, and X. Le, *Sci. China Phys. Mech. Astron.* **53**, 465 (2010).
- ¹⁷⁷ E. Arslan, M.K. Ozturk, Ö. Duygulu, A.A. Kaya, S. Ozcelik, and E. Ozbay, *Appl. Phys. A* **94**, 73 (2009).

- ¹⁷⁸ J.A. Freitas, M.A. Mastro, E.R. Glaser, N.Y. Garces, S.K. Lee, J.H. Chung, D.K. Oh, and K.B. Shim, *J. Cryst. Growth* **350**, 27 (2012).
- ¹⁷⁹ C. Chen, T. Yan, S.-H. Yu, C.-Y. Lee, C.-W. Chang, and M.M.C. Chou, *RSC Adv* **5**, 35405 (2015).
- ¹⁸⁰ V. Thakur, S.K. Nayak, K.K. Nagaraja, and S.M. Shivaprasad, in *2014 IEEE 2nd Int. Conf. Emerg. Electron. ICEE* (2014), pp. 1–4.
- ¹⁸¹ A. Kadir, T. Ganguli, M.R. Gokhale, A.P. Shah, and A. Bhattacharya, *Phys. Status Solidi A* **207**, 1070 (2010).
- ¹⁸² N.P. Siwak, X.Z. Fan, and R. Ghodssi, *J. Micromechanics Microengineering* **25**, 043001 (2015).
- ¹⁸³ F.M. Morales, R. García, S.I. Molina, A. Aouni, P.A. Postigo, and C.G. Fonstad, *Appl. Phys. Lett.* **94**, (2009).
- ¹⁸⁴ K. Kasaya, O. Mitomi, M. Naganuma, Y. Kondo, and Y. Noguchi, *Photonics Technol. Lett. IEEE* **5**, 345 (1993).
- ¹⁸⁵ T.P.E. Broekaert, J.F. Jensen, D. Yap, D.L. Persechini, S. Bourgholtzer, C.H. Fields, B. Shi, and R.H. Walden, *Solid-State Circuits IEEE J. Of* **36**, 1335 (2001).
- ¹⁸⁶ J.W. Matthews and A.E. Blakeslee, *J. Cryst. Growth* **27**, 118 (1974).
- ¹⁸⁷ L. Sagalowicz, A. Rudra, E. Kapon, M. Hammar, F. Salomonsson, A. Black, P.-H. Jouneau, and T. Wipijewski, *J. Appl. Phys.* **87**, 4135 (2000).
- ¹⁸⁸ S.N.G. Chu, W.T. Tsang, T.H. Chiu, and A.T. Macrander, *J. Appl. Phys.* **66**, 520 (1989).
- ¹⁸⁹ R. Kumar, V.K. Dixit, and T.K. Sharma, *Vacuum* **154**, 214 (2018).
- ¹⁹⁰ Ł. Gelczuk, D. Pucicki, J. Serafińczuk, M. Dąbrowska-Szata, and P. Dłużewski, *J. Cryst. Growth* **430**, 14 (2015).

- ¹⁹¹ O. Yastrubchak, J.Z. Domagała, T. Wosiński, A. Kudła, and K. Regiński, *Phys. Status Solidi C* **2**, 1943 (2005).
- ¹⁹² E.P. Kvam and R. Hull, *J. Appl. Phys.* **73**, 7407 (1993).
- ¹⁹³ M. Natali, D.D. Salvador, M. Berti, A.V. Drigo, L. Lazzarini, G. Salviati, G. Rossetto, and G. Torzo, *J. Vac. Sci. Technol. B Microelectron. Nanometer Struct. Process. Meas. Phenom.* **18**, 2527 (2000).
- ¹⁹⁴ A. Diéguez, A. Vilà, A. Cornet, S.A. Clark, D.I. Westwood, and J.R. Morante, *J. Vac. Sci. Technol. B* **15**, 687 (1997).
- ¹⁹⁵ X. Wu and G.C. Weatherly, *J. Cryst. Growth* **233**, 88 (2001).
- ¹⁹⁶ P.A. Postigo, F. Suárez, A. Sanz-Hervás, J. Sangrador, and C.G. Fonstad, *J. Appl. Phys.* **103**, 013508 (2008).
- ¹⁹⁷ S.A. Ringel and B. Chatterjee, *J. Appl. Phys.* **83**, 5904 (1998).
- ¹⁹⁸ E. Williams, W. Elder, M. Astles, M. Webb, J. Mullin, B. Straughan, and P. Tufton, *J. Electrochem. Soc.* **120**, 1741 (1973).
- ¹⁹⁹ Y. Moon, S. Si, E. Yoon, and S.J. Kim, *J. Appl. Phys.* **83**, 2261 (1998).
- ²⁰⁰ P.H. Borchers, G.F. Alfrey, A.D.B. Woods, and D.H. Saunderson, *J. Phys. C Solid State Phys.* **8**, 2022 (1975).
- ²⁰¹ Y. He, Y. Sun, Y. Zhao, S. Yu, and J. Dong, *J. Mater. Sci. Mater. Electron.* **28**, 9732 (2017).
- ²⁰² R. Kumar, A. Bag, P. Mukhopadhyay, S. Das, and D. Biswas, *Appl. Surf. Sci.* **357**, 922 (2015).
- ²⁰³ A Georgakilas, P Panayotatos, J Stoemenos, J-L Mourrain, and A Christou, *J Appl Phys* **71**, 2679 (1992).

- ²⁰⁴ D J Meyer, *Silicon Epitaxy (Chap. 10- Si-Based Alloys: SiGe and SiGe:C)* (Academic Press, San Diego, CA, 2001).
- ²⁰⁵ S. Pal, S.D. Singh, V.K. Dixit, T.K. Sharma, R. Kumar, A.K. Sinha, V. Sathe, D.M. Phase, C. Mukherjee, and A. Ingale, *J. Alloys Compd.* **646**, 393 (2015).
- ²⁰⁶ B.S. Yadav, S. Singh, T. Ganguli, R. Kumar, S.S. Major, and R.S. Srinivasa, *Thin Solid Films* **517**, 488 (2008).
- ²⁰⁷ A. Owens and A. Peacock, *Proc. 5th Int. Workshop Radiat. Imaging Detect.* **531**, 18 (2004).
- ²⁰⁸ M.C. Veale, S.J. Bell, D.D. Duarte, M.J. French, A. Schneider, P. Seller, M.D. Wilson, A.D. Lozinskaya, V.A. Novikov, O.P. Tolbanov, A. Tyazhev, and A.N. Zarubin, *Nucl. Instrum. Methods Phys. Res. Sect. Accel. Spectrometers Detect. Assoc. Equip.* **752**, 6 (2014).
- ²⁰⁹ M.C. Veale, S.J. Bell, D.D. Duarte, M.J. French, M. Hart, A. Schneider, P. Seller, M.D. Wilson, V. Kachkanov, A.D. Lozinskaya, V.A. Novikov, O.P. Tolbanov, A. Tyazhev, and A.N. Zarubin, *J. Instrum.* **9**, C12047 (2014).
- ²¹⁰ Engin Arslan, Mustafa K Ozturk, Ali Teke, Suleyman Ozcelik, and Ekmel Ozbay, *J Phys Appl Phys* **41**, 155317 (2008).
- ²¹¹ J Kozlowski, R Paszkiewicz, and M Tlaczala, *Phys Status Solidi B* **228**, (2001).
- ²¹² X.L. Wang, D.G. Zhao, X.Y. Li, H.M. Gong, H. Yang, and J.W. Liang, *Mater. Lett.* **60**, 3693 (2006).
- ²¹³ S. Ghanad Tavakoli, O. Hulko, and D.A. Thompson, *J. Appl. Phys.* **103**, 103527 (2008).
- ²¹⁴ Tetsuo Soga, Takashi Jimbo, and Masayoshi Umeno, *J Cryst Growth* **163**, 165 (1996).

²¹⁵ Masato Imai, Yoshiji Miyamura, Daisuke Murata, Takahiro Kanda, Takane Kobayashi, and Kazuhiko Omote, in (2008).

²¹⁶ A. Vilà, A Cornet, J R Morante, P Ruterana, M Loubradou, and R Bonnet, J Appl Phys **79**, 676 (1996).